Jumps and Pirouettes – a Dance of Disks and Planets

Dissertation

der Mathematisch-Naturwissenschaftlichen Fakultät

der Eberhard Karls Universität Tübingen

zur Erlangung des Grades eines

Doktors der Naturwissenschaften

(Dr. rer. nat.)

vorgelegt von

M. Sc. Thomas Rometsch

aus Nagold

Tübingen
2022

Gedruckt mit Genehmigung der Mathematisch-Naturwissenschaftlichen Fakultät
der Eberhard Karls Universität Tübingen.

Tag der mündlichen Qualifikation:	16.11.2022
Dekan:	Prof. Dr. Thilo Stehle
1. Berichterstatter:	Prof. Dr. Klaus Werner
2. Berichterstatter:	Prof. Dr. Cornelis P. Dullemond

In memory of Willy Kley.

Contents

Abstract

Protoplanetary disks are the birthplace of planets. Before these gaseous disks are dispersed by the radiation from their host star they interact with the planets that form out of them. This interaction causes the planets to change their orbits and the disk to be sculpted by the planets if these are sufficiently massive. Transition disks constitute a subset of the protoplanetary disks that feature an inner hole while mass accretion onto the star is ongoing. While transition disks with small inner holes and low accretion rates have already been explained by photoevaporation, the origin of transition disks with large inner holes up to tens of astronomical units wide and high mass accretion rates remains unclear.

In this thesis, I explain, using two-dimensional fluid dynamics simulations, how an outward migrating pair of planets can reproduce the characteristics of transition disks with large holes and high accretion rates.

In addition, I describe a newly-found phenomenon in the realm of planet–disk interaction. During the process which I call a migration jump, a pair of giant planets resonantly migrates outward which excites the eccentricity of the planets and creates a vortex in the outer disk. Through interaction with the vortex, the outer planet enters an accelerated phase of outward migration allowing it to cover tens of astronomical units in only a few thousand years, before it quickly migrates back into the initial configuration with the inner planet.

Sparked by the prominence of the vortex in the migration jump, I studied the properties of planet-induced large-scale vortices in protoplanetary disks and their dependence on the thermal relaxation timescale and the level of viscosity of the disk. For the detection and analysis of vortices in simulation data, I developed a novel detection pipeline based on computer vision algorithms. The vortices tend to live longest in disks with low viscosity and short thermal relaxation timescale and live shortest in disks with thermal relaxation timescales comparable to the orbital period.

Kurzfassung

Protoplanetare Scheiben sind die Geburtsstätte von Planeten. Bevor diese Gasscheiben von der Strahlung ihres Zentralsterns zerstreut werden, interagieren sie mit den Planeten, die aus ihnen entstehen. Diese Interaktion führt zu einer Veränderung der Planetenorbits, und falls die Planetenmassen hoch genug sind, führt sie zu einer Formung der Scheibe selbst. Eine Untergruppe der protoplanetaren Scheiben sind die Übergangsscheiben, welche in Beobachtungen im Zentrum ein Loch aufweisen und gleichzeitig Massenakkretion auf den Zentralstern erlauben. Während die Übergangsscheiben mit kleinen Löchern und geringen Akkretionsraten bereits durch Photoevaporation erklärt werden können, bleibt die Herkunft von denjenigen mit großen Löchern bis zu einigen zehn astronomischen Einheiten und hohen Akkretionsraten unklar.

In dieser Doktorarbeit erkläre ich anhand von zweidimensionalen Strömungsdynamiksimulationen, wie ein nach außen migrierendes Planetenpaar die Übergangsscheiben mit großen Löchern und hohen Akkretionsraten erklären kann.

Außerdem beschreibe ich ein neu entdecktes Phänomen im Bereich der Planet-Scheiben Wechselwirkung. In dem Prozess, den ich Migrationssprung nenne, migriert ein Planetenpaar in Resonanz nach außen, wodurch die Exzentrizitäten der Planeten erhöht werden und ein Wirbel in der äußeren Scheibe entsteht. Durch die Interaktion mit dem Wirbel beginnt der äußere Planet eine Phase von beschleunigter, nach außen gerichteter Migration, während welcher er mehrere zehn astronomische Einheiten in nur wenigen Tausend Jahren zurücklegen kann, bevor er wieder rasch in die ursprüngliche Konfiguration mit dem inneren Planeten zurückkehrt.

Inspiriert durch die prominente Rolle des Wirbels in den Migrationssprüngen untersuchte ich die Eigenschaften von großen Wirbeln, die von Planeten erzeugt werden, und deren Abhängigkeit von der thermischen Relaxationszeit und der Viskosität der Scheibe. Zur Detektion und Analyse von Wirbeln in Simulationsdaten entwickelte ich ein neues Vorgehen basierend auf Bilderkennungsalgorithmen. Die Wirbel leben am längsten in Scheiben mit geringer Viskosität und kurzer thermischer Relaxationszeit und leben am kürzesten in Scheiben mit einer thermischen Relaxationszeit, die mit der Umlaufperiode des Planeten vergleichbar ist.

1 Introduction

Countless civilizations have attributed gods of all different kinds to Nature's various phenomena that govern our lives, to the elements and to the celestial bodies. In many cultures, the sun god takes the role of a king of gods being associated with consciousness itself, as is the case for Egyptian mythology with its sun god *Ra* and his offspring, the god of the sky *Horus* whose two eyes are the sun and the moon.

Living in an age of never-ending technological marvels and having access to electrical light at any time, the importance of the sun for daily life might be less striking to us than to our ancestors, but being in the presence of a view of the night sky, unimpeded by light pollution, is still one of the most awe-inspiring experiences possible. In the night sky, the colorful wanderers — the ancient Greek word *planētai* translates to *wanderers* — are very prominent, being the brightest objects together with our moon.

For many humans, curiosity accompanies awe and observing that the planets are large objects orbiting the sun, the next questions to ask are: how do these planets form? And what about the moon and the sun? As it turns out, these questions are intricately connected.

1.1 A brief story of planet formation

Stars are giant bodies of gas that are so massive that the gravitational attraction they exert on themselves is enough to trigger and sustain nuclear fusion in their interiors. They form during the collapse of gaseous cores inside a giant molecular cloud, usually together with many other stars, which is reflected in the fact that over half of the observed stars are in binary or multiple start systems (Offner et al. 2022). Different stages of the collapse process are sketched in Fig. 1.1. After the first 10^4–10^5 years, part of the collapsing cloud has accumulated into a protostar, not yet producing its radiated energy by nuclear fusion but by contraction heating. At this stage, the protostar is still embedded in an opaque cloud.

Because the initial cloud is subject to internal differential motion, the cloud generally has a non-zero angular momentum. Because of angular momentum conservation, the cloud can only freely fall onto the star parallel to the rotation axis. In the plane perpendicular to the rotation axis, some material needs to stay at a distance while orbiting the central protostar. In addition, jets can emerge parallel to the rotation axis, fueled by gravitational energy which is released as the material moves closer to the central star.

During an intermediate stage of the star formation process which lasts several 10^5–10^6 yr (Haisch et al. 2001) when the star is in the *T Tauri* phase (named after

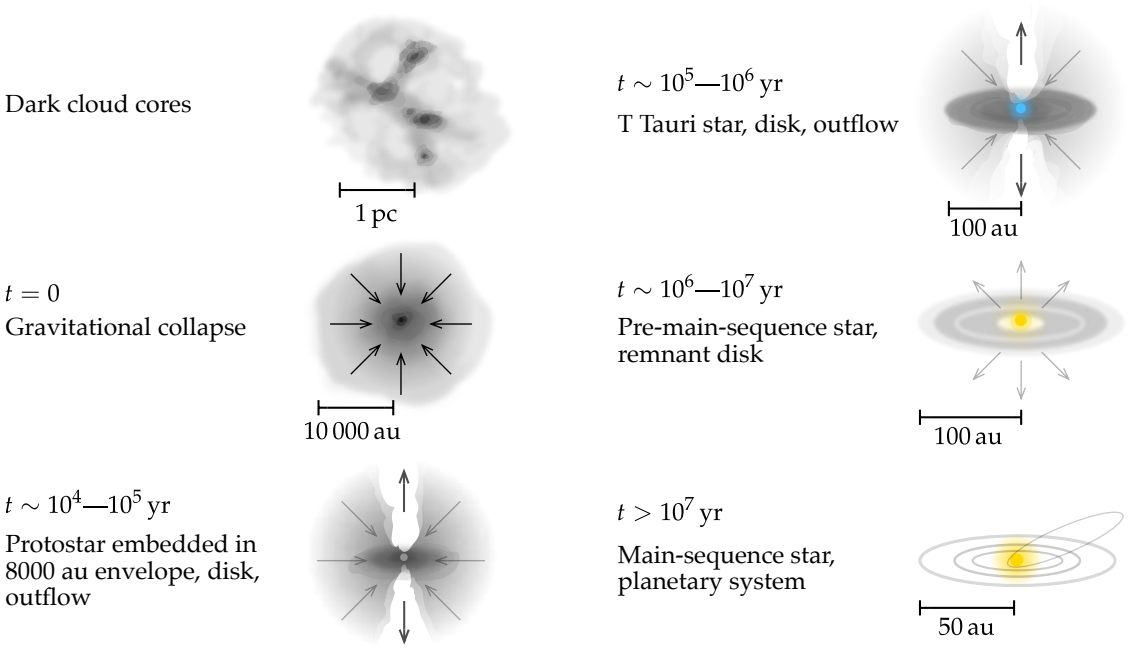

Figure 1.1: Sketch of the multiple stages of star formation from a giant molecular cloud to a planetary system. Credit: André Oliva, adapted from Greene (2001).

a particular star in the Taurus constellation), a disk-like structure exists around the protostar which is the result of angular momentum conservation and which is surrounded by a thin envelope. Most of the accretion (mass accumulation) onto the star ensues through the disk at this stage — hence the name *accretion disk*. It is in these disks where planets are formed — accordingly, they are often called protoplanetary disks (PPDs). The gas in a PPD is finally either accreted onto the protostar or expelled from the disk by photoevaporation until only small solid objects and planets remain.

Akin to the interstellar medium (ISM) they emerge out of, it is assumed that PPDs have a similar chemical composition with around 1 % being μm-sized dust (Mathis et al. 1977). These dust particles are the fundamental building blocks for terrestrial planets.

In the most widely accepted scenario, the core accretion scenario, planets form by the agglomeration of this μm-sized dust into larger dust grains, which collide and stick together to form meter-sized pebbles and boulders and finally km-sized planetesimals. Planetesimals are then able to gravitationally attract additional solid particles until they grow to terrestrial planets. The left-over small solid bodies

and the fragments caused by the collision of larger objects end up as comets and asteroids. The resulting bodies can be a discerning factor in assessing solar system formation theories by a comparison of the statistics of observed bodies in the asteroid and Kuiper belt to predictions from models (Nesvorný 2018). While smaller terrestrial planets are able to retain a small gaseous atmosphere (the atmosphere of the Earth accounts for $\sim 10^{-6}$ of its total mass), larger rocky planets (with a mass of 10–20 $M_\oplus$, Mizuno 1980; Ikoma et al. 2000) can accrete much more gas and grow to become gas giants like Jupiter.

1.2 Accretion disks

A characteristic property of PPDs is that they are accretion disks. Accretion rates onto young T Tauri stars range from 10^{-9}–$10^{-7}\,M_\odot$/yr with a median at $10^{-8}\,M_\odot$/yr (Hartmann et al. 1998). Disk masses around young stellar objects range from 10^{-4} to a few $10^{-1}\,M_\odot$ (Andrews & Williams 2005). Because of angular momentum conservation, an accretion disk must facilitate angular momentum transport from the inside out — otherwise, the disk material would stay at a fixed orbit, analogous to how planets stay on fixed orbits if not perturbed. Accretion disks can be thought of as machines that transport angular momentum away and mass towards the star.

Therefore, an angular momentum transport mechanism is needed. Viscosity, the resistance to shear within the fluid of the disk, is a suitable candidate as can be shown with simple 1D disk models (Lynden-Bell & Pringle 1974). However, the molecular viscosity of the gas is much too small to sustain the observed mass accretion through the disk, and thus turbulence has been proposed to be the driving mechanism of angular momentum transport — resulting in an effective turbulent viscosity. This is a widely used assumption and encapsulated in the α-viscosity model (Shakura & Sunyaev 1973) where the turbulence is parameterized as an effective viscosity through the viscous stress tensor. During the last decades, numerous different types of turbulence and instabilities with the ability to transport angular momentum have been identified. The list includes the magneto-rotational instability (MRI, Balbus & Hawley 1990), the gravitational instability (Gammie 2001), and the vertical shear instability (VSI, Nelson et al. 2013). All these instabilities occur under different sets of conditions which sometimes overlap, leading to one instability attacking the structures formed by a previous instability. The efficiency of these instabilities and their turbulence in transporting angular momentum can usually not be evaluated analytically, and thus numerical simulations have been performed to assess it. The angular momentum transport efficiency due to instabilities ranges from $\alpha = 10^{-5}$–10^{-3} for the VSI (Nelson et al. 2013; Stoll & Kley 2014; Flock et al. 2017; Barraza-Alfaro et al. 2021) and $\alpha = 10^{-3}$–10^{-2} for the MRI (Hawley et al. 1995). These values are consistent with the mass accretion rates observed for young stars (Hartmann et al. 1998).

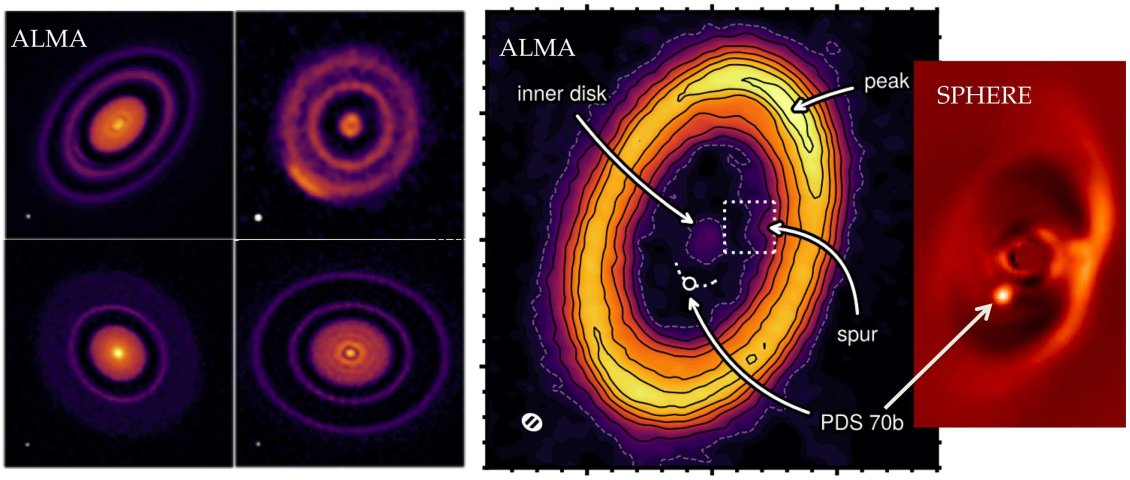

Figure 1.2: Left: Disk observations using high resolution radio observations with ALMA from the DSHARP survey (Andrews et al. 2018) revealing many substructures. Right: ALMA (Keppler et al. 2018) and near-IR observations using the VLT (insert on the right, Müller et al. 2018) of the unique PDS 70 system in which two giant planets were directly observed while still accreting and being embedded in their disk (Haffert et al. 2019).

Contemporary observations are able to resolve the disk with the help of interferometry, either in radio wavelengths, e.g. with the Atacama Large Millimeter Array (ALMA, see left and center panel Fig. 1.2), or in infrared with the Very Large Telescope (VLT, see right panel Fig. 1.2), in combination with sophisticated data analysis and interpretation techniques. Many of the resolved disk observations show substructures in the disks (see Fig. 1.2) including holes, rings, arcs and localized intensity maxima. The sizes of the resolved disks vary from some tens to some hundreds of au.

1.3 Transition disks

While an observed accretion rate indirectly hints at the existence of an accretion around a young star, the existence of a disk can also be directly identified by the spectrum of emission due to thermal radiation from the μm-sized to mm-sized dust grains. As illustrated in the left panel of Fig. 1.3, the disk appears as a plateau in the spectrum of the star-disk system at the Rayleigh end of the stellar blackbody spectrum, because the disk is considerably cooler than the stellar surface, but with a much larger surface area. Because the temperature in the disk midplane usually decreases outward, the disk spectrum is a superposition of a range of blackbody

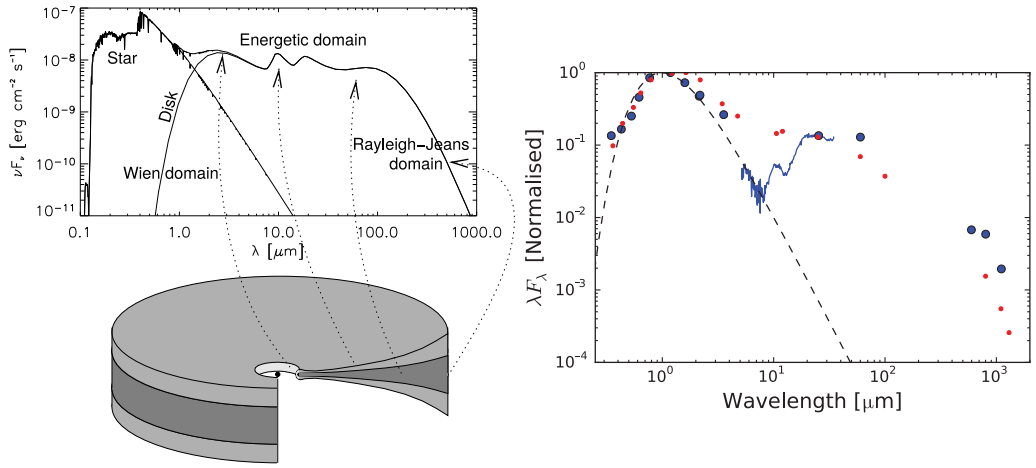

Figure 1.3: Schematic spectrum of a protostar and its disk (left, from Dullemond et al. 2007) and the observational spectrum of the transition disk DM Tau (blue) along with the stellar spectrum (dashed line) and the median spectral energy distribution (red dots) of PPDs in the Taurus star-forming region (right, from Owen 2016).

spectra with different temperatures, emitted at different radii within the disk. As a consequence, different parts of the spectrum can be associated with different radii in the disk (see the left panel of Fig. 1.3).

Observationally, PPDs were first identified and distinguished from isolated stars by their emission in the near- and mid-infrared. In addition to smooth disks and isolated stars, there was a third class of observed objects that were believed to be in an intermediary state during which the stars lose their disk (Kenyon & Hartmann 1995). Owing to this hypothesized transitional state, these objects were termed *transition disks* (TDs).

Spectral observations of TDs reveal an even clearer way to define this subclass of disks. TDs lack emission in the near-infrared which results in a valley in their spectrum between the stellar and disk contributions (see the blue line in the right panel in Fig. 1.3). Relying on the fact that the wavelength of the emission is linked to the distance from the star, this missing near-infrared emission indicates that TDs have holes in their dust distribution close to the star.

Owen (2016) classified TDs into two opposing categories. TDs with low millimeter-fluxes (mm-flux), small inner hole sizes ($\lesssim 10\,\mathrm{au}$) and low accretion rates (10^{10}–$10^{-9}\,\mathrm{M}_\odot/\mathrm{yr}$) were classified as type I. TDs with high mm-fluxes, large inner hole sizes ($\gtrsim 20\,\mathrm{au}$) and high accretion rates ($10^{-8}\,\mathrm{M}_\odot/\mathrm{yr}$) were classified as type II.

Type I disks can mostly be explained by X-ray photoevaporation (Owen 2016; Picogna et al. 2019). Because photoevaporation is most efficient close to the star,

photoevaporative disk dispersal happens from the inside out. It starts at the distance from the star, where thermal energy input from stellar irradiation is sufficiently high to overcome the gravitational attraction by the star.

Type II disks appear as a paradox. They simultaneously have large inner holes but show large accretion rates at the same time. Here, however, a caveat is important. The observations, spectra and images, show dust emission. As a consequence, there might just be a hole in the dust distribution and the gas disk might be continuous.

It is known from analytical theory (Goldreich & Tremaine 1979, 1980) that giant planets in PPDs open gaps — a fact which was verified in hydrodynamics simulations many times (e.g. Kley 1999; Crida et al. 2006; Kanagawa et al. 2017). This suggests a possible explanation of type II disks in which a system of giant planets opens a large hole in the disk via gravitational interaction.

1.4 Migration and gap opening

As outlined in Sect. 1.1, planets form in and out of accretion disks around young stars. This means that there must be a time when both the planets and their parent disk coexist. During this time, the planets and the disk interact gravitationally and exchange angular momentum. The change of the angular momentum of a planet results in migration — a change in the distance to the host star — as well as changes in eccentricity and inclination, and precession of the orbit. For typical disk parameters and planet masses up to several $\mathrm{M_J}$, the planets lose angular momentum which causes the planets to migrate closer to the star Ward (1997); Kley & Nelson (2012). See Sect. 2.3 for more details on planet migration.

Planets with sufficiently large mass can push away material from their orbit and thus create a gap in the disk (e.g. Goldreich & Tremaine 1980; Ward 1997; Kanagawa et al. 2017), much like the planets in the solar system clear their orbits from asteroids and how the moons around Saturn create the gaps in its rings. For a PPD, this process is governed by a balance between the angular momentum flux carried by density waves launched close to the planet and the angular momentum flux of the viscous disk evolution that refills the gap. Thus, the mass needed to open a gap scales with the efficiency of the disk to open a planet. For a relatively cold disk with an aspect ratio of $h = 0.05$ and a low viscosity $\alpha \lesssim 10^{-4}$, this planet mass can be as low as one Neptune mass $\mathrm{M_{Nep}} \approx 0.05\,\mathrm{M_J} \approx 5 \times 10^{-5}\,\mathrm{M_\odot}$ (Kanagawa et al. 2015). This gap opening capability was repeatedly invoked to explain rings in observations of PPDs, e.g. for the first image of a PPD produced by ALMA (the disk around HL Tau, ALMA Partnership et al. 2015) or for the disks in the DSHARP survey (Andrews et al. 2018, see also the left panel of Fig. 1.2 for examples of rings).

For a special case of resonant migration of a pair of two giant planets ($M_p \gtrsim 3\mathrm{M_J}$),

the overlapping gaps of both planets can reach widths that are comparable to their distance to the central star (Masset & Snellgrove 2001). This property is what makes them ideal candidates for carving the gaps and holes in type II TDs (Owen 2016). The formation of a gap can also stop dust particles from drifting inward further than the outer gap edge. Just outside the outer gap edge, a radial pressure maximum forms as a consequence of the gap opening. For the dust sizes that are observable by ALMA, this pressure maximum acts as a barrier, halting the inward drift of the dust particles (Weidenschilling 1977). This creates a scenario in which a planetary system carves a large gap that is visible as a large inner hole in dust observations.

Coincidentally, the only system in which we observed planets in their natal disk that are actively accreting is one with such properties. The disk around PDS 70 (see Fig. 1.2 for observations with ALMA and the VLT) features a large inner hole of around 40 au and two super-Jupiter-mass planets in a configuration compatible with resonant outward migration (Müller et al. 2018; Keppler et al. 2019; Bae et al. 2019; Rometsch et al. 2020, see also Sect. 4.3 for more details about the modelling of this system).

1.5 Vortices

One consequence of gap opening by embedded planets is the possibility of the emergence of vortices in the disk (Li et al. 2005; Val-Borro et al. 2007). Conditions for their formation exist either during the planet formation process when a gap is created for the first time or during the dynamical interplay of multiple giant planets.

Vortices and eddies are the fundamental building blocks of turbulence (Lyra & Umurhan 2019) and can exist on a range of length scales in a given system. Depending on the type of turbulence as characterized by the power law exponent of its spectral energy density, turbulent energy is moved from large scales to very small scales, where the energy is dissipated into heat, or from small scales to large scale, resulting in the formation of large-scale vortices.

In the context of PPDs, there are several ways, including instabilities, that enable the growth or destruction of vortices. Growth can be sustained by the Rossby-wave instability (RWI, Lovelace et al. 1999), the subcritical baroclinic instability (SBI, Klahr & Bodenheimer 2003; Lesur & Papaloizou 2010), or the zombie vortex instability (ZVI, Marcus et al. 2015, 2016). The RWI can occur in PPDs at the edge of a gap in the disk, which can either be opened by embedded giant planets (Li et al. 2005; Val-Borro et al. 2007) or at viscosity transitions which are expected to happen at the interface of a dead zone (Godon & Livio 1999). Vortex decay can be brought about by viscous spreading that attacks the vortex boundary and diffuses the vortex, or from within the vortex, e.g. by the elliptical instability (Lesur &

Papaloizou 2009). Vortex properties, including their lifetime, not only depend on viscosity, but also on the thermodynamic properties of the disk which influence the kinematic viscosity via the temperature in the α prescription (Pierens & Lin 2018; Tarczay-Nehéz et al. 2020) or directly via vortensity generation at the planetary spiral arm shocks (Cimerman & Rafikov 2021).

There is a large number of substructures found in resolved protoplanetary disks (Andrews 2020). Some of these observations include non-axisymmetric and lopsided structures. Possible explanations range from dust trapped in the Lagrange points of gap-opening planets (Rodenkirch et al. 2021) to the presence of vortices (Barge & Sommeria 1995; Marel et al. 2013; Bae et al. 2016; Pérez et al. 2018; Hammer et al. 2019). Fig. 1.4 shows a collection of vortices as they emerge in non-linear fluid dynamics simulations and as they appear in observations of PPDs.

The basic argument of employing vortices for the explanation of non-axisymmetric structures in disk observations is their tendency to accumulate dust (Barge & Sommeria 1995; Tanga et al. 1996; Johansen et al. 2004). Dust particles follow pressure gradients in the disk and as a result, they accumulate in the center of a pressure maximum. Anticyclonic vortices in PPDs correspond to pressure maxima (Lyra & Umurhan 2019) and thus accumulate dust naturally. Because ALMA images the dust content of PPDs close to the midplane (Andrews 2020), a lopsided structure in a disk is a plausible hint at the existence of a vortex.

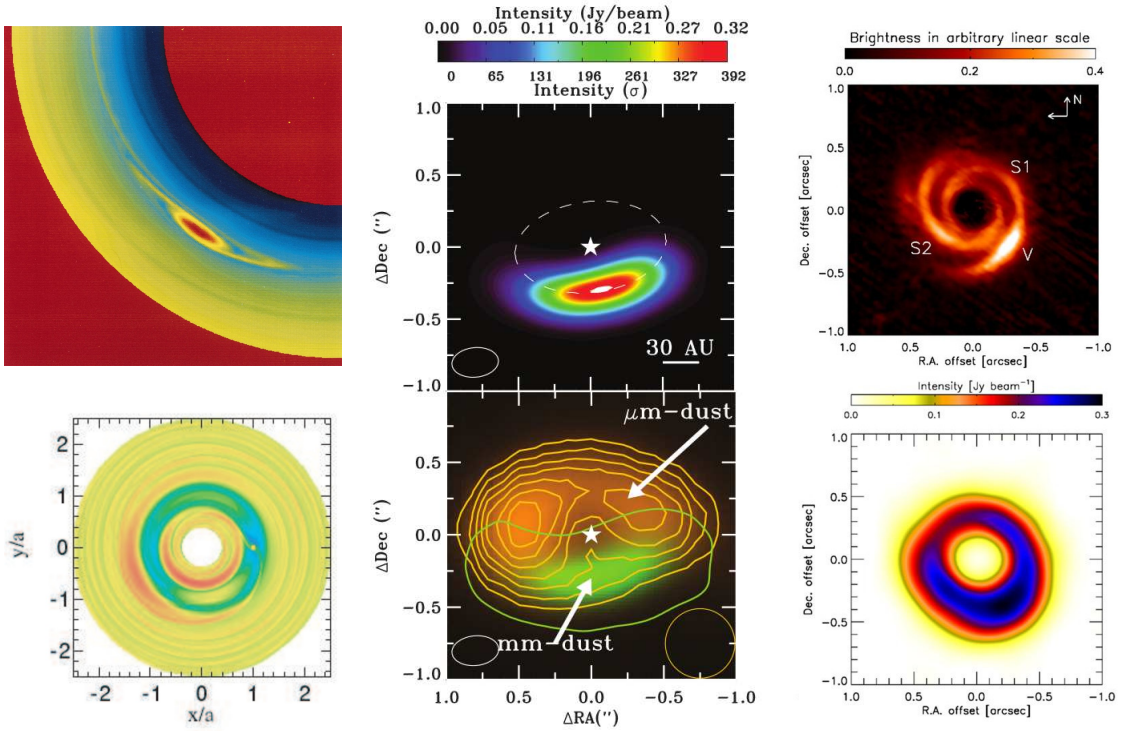

Figure 1.4: Vortices in PPD models and observations with large-scale asymmetries in brightness interpreted as vortices. Left: a numerical fluid dynamics simulations in which a vortex formed at a jump in density due to a viscosity transition (top, Godon & Livio 1999) and due to a gap carved by a giant planet (bottom, Val-Borro et al. 2007). Center: the asymmetry in the IRS 48 disk observed with ALMA (Marel et al. 2013) in dust continuum (top) and μm-sized and mm-sized dust (bottom). Right: the disk of HD 135344 in scattered light observations (top, Garufi et al. 2013) and in dust continuum emission with ALMA (bottom, Pérez et al. 2014).

1.6 Aims

Transition disks inhabit the space between smooth accretion disks and planetary systems. Planets have been invoked to explain their characteristics based on their ability to carve gaps into the disks (Rice et al. 2003; Quillen et al. 2004; Calvet et al. 2005) From previous numerical modeling of these disks with embedded planets, the expectation arises that they show various types of substructures including spirals (Ogilvie & Lubow 2002), rings (Rafikov 2002) and non-axisymmetric features such as vortices (Val-Borro et al. 2007). Indeed, resolved disk observations show a plethora of such substructures (Andrews et al. 2018).

This thesis aims to study the more concrete hypothesis proposed by Owen (2016) that **type II transition disks — those with large hole size, high accretion rate and high mm-flux — can be explained by a system of embedded planets** using two-dimensional fluid dynamics simulations. Along with the attempt of reproducing type II TDs, the dynamical evolution of the embedded planetary system is investigated.

The emergence of vortices during the interaction of disks with embedded giant planets (Val-Borro et al. 2007) and their importance in the observed dynamical effects in the first part of this thesis motivated a further investigation into the properties of planet-induced vortices with a focus on the role of radiative effects which have been demonstrated to be of vital importance for the simulation of disk-planet systems (Ziampras et al. 2020; Miranda & Rafikov 2020).

For both investigations, the influence of physical and numerical choices such as the thermal relaxation timescale, the level of turbulence, the inclusion of self-gravity and radiative processes, and the resolution are studied to support the validity of the results.

2 Theoretical background and methods

This chapter describes the methods and theoretical background used to answer the astrophysical questions in this thesis. The chapter gives an overview of the fluid dynamics equations, a typical PPD model, the gravitational interaction between planets and PPDs, and vortices. Additionally, the simulation tool and a typical simulation workflow are described.

2.1 Fluid dynamics

The theoretical basis for the description of many astrophysical systems is fluid dynamics (Shu 1992). On a conceptual level, fluid dynamics can be derived from three types of conservation laws: conservation of mass, momentum and energy. In a mathematical formulation, the three conservation laws take the form (see, e.g. Shu 1992)

$$\frac{\partial \rho}{\partial t} + \nabla \cdot (\rho \vec{u}) = 0\,, \tag{2.1a}$$

$$\frac{\partial (\rho \vec{u})}{\partial t} + \nabla \cdot (\rho \vec{u} \otimes \vec{u}) = -\nabla p + \rho \vec{k} + \nabla \tau\,, \tag{2.1b}$$

$$\frac{\partial (\rho \varepsilon)}{\partial t} + \nabla \cdot (\rho \varepsilon \vec{u}) = -p \nabla \cdot \vec{u} + S\,, \tag{2.1c}$$

where ρ is the mass density, $\vec{u}$ is the velocity, $\otimes$ denotes the tensor product, ε is the specific internal energy, p is the pressure, $\vec{k}$ is the acceleration due to external forces, τ is the viscous stress tensor, and S are radiative sources and sinks. The inviscid form of Eqs. (2.1) (with $\tau = 0$) are also called the Euler equations.

The viscous stress tensor is defined as (see, e.g. Shu 1992)

$$\tau_{ij} = 2\,\mu \left[\frac{1}{2} \left(\frac{\partial u_i}{\partial x_j} + \frac{\partial u_j}{\partial x_i} \right) - \frac{\delta_{ij}}{3} \nabla \vec{u} \right] + \zeta \delta_{ij} \nabla \vec{u}\,, \tag{2.2}$$

where $i, j \in \{1, 2, 3\}$ indicate the spatial directions, μ and ζ are the shear and bulk viscosity, respectively, and δ_{ij} is the Kronecker δ. In the case of PPDs, ζ can usually be neglected and one can write $\mu = \nu\rho$ with the kinematic viscosity denoted by ν.

Equations (2.1a) to (2.1c) are usually called the Navier–Stokes equations and represent five partial differential equations (PDEs), counting each component of $\vec{u}$ separately plus the scalar continuity and energy equations. Yet, a fluid is described by six quantities: ρ, ε, the three components of $\vec{u}$, and p. In order to solve the system of PDEs, an additional relationship between the pressure and the other quantities is needed. Such a relation that enables the solution of a system of PDEs is usually called a closure relation and in the context of fluid dynamics, it is called the equation of state (EOS). The EOS links p to ρ and ε of the fluid or, equivalently, to ρ and the temperature T.

In the context of PPDs and astrophysics in general, the fluid is often assumed to be an ideal gas, which is justified by the very low volume densities involved (Shu 1992). The EOS then takes the form

$$p = \frac{\mathrm{R_G}}{\mu} T \rho \,, \tag{2.3}$$

with the gas constant $\mathrm{R_G} = \mathrm{k_B}/\mathrm{m_H}$, the Boltzmann constant $\mathrm{k_B}$, the hydrogen mass $\mathrm{m_H}$, and the mean molecular weight μ in units of $\mathrm{m_H}$.

There exists no closed solution to Eqs. (2.1), so numerical methods are used to solve them in a discretized way or approximations have to be utilized.

2.2 A simplified protoplanetary disk model

Even though the Navier–Stokes equations have no analytical solution, approximate solutions under various conditions can be achieved. This section presents common assumptions which lead to the disk models which are commonly used to study PPDs (for more details, see the review by Lodato 2008).

One suitable approximation for PPDs is that the disk is very thin, meaning that their vertical extent, as measured by the vertical pressure scale height H, is much smaller than the radius r at each location in the disk. The aspect ratio, $h = H/r \ll 1$, is set by the balance between (thermal) pressure and gravity from the central object and the disk itself. Temperature and (as a consequence) pressure are increased by heating from viscous dissipation and stellar or cosmic irradiation and lowered by emission from the surfaces of the disk (Hubeny 1990). All these processes depend on the particulars of the environment and the microphysics and chemistry of the disk which, e.g., determine the opacities and thus influence all radiative processes.

As a first consequence of the small aspect ratio, PPD models are often treated using the vertically integrated form of the fluid dynamics equations Eqs. (2.1). They are obtained by vertical integration ($\int_{-\infty}^{\infty} \mathrm{d}z \ldots$) in a cylindrical coordinate

system (r, ϕ, z) in which the disk coincides with the $z = 0$ plane:

$$\frac{\partial \Sigma}{\partial t} + \nabla \cdot (\Sigma \vec{u}) = 0\,, \tag{2.4a}$$

$$\frac{\partial (\Sigma \vec{u})}{\partial t} + \nabla \cdot (\Sigma \vec{u} \otimes \vec{u}) = -\nabla P + \Sigma \vec{k} + \nabla \tau\,, \tag{2.4b}$$

$$\frac{\partial (\Sigma \varepsilon)}{\partial t} + \nabla \cdot (\Sigma \varepsilon \vec{u}) = -P \nabla \cdot \vec{u} + S\,, \tag{2.4c}$$

where the density ρ is replaced by the surface density $\Sigma = \int_{-\infty}^{\infty} \rho \,\mathrm{d}z$, pressure p is replaced by vertically integrated pressure $P = \int_{-\infty}^{\infty} p \,\mathrm{d}z$, and the velocities are restricted to the disk plane such that $u_z = 0$. External forces $\vec{k}$, the stress tensor τ and energy source terms S change their meaning accordingly.

For these 2D disks, equilibrium solutions can be derived assuming the disks to be axially symmetric (e.g. Lynden-Bell & Pringle 1974). For this case, the surface density and temperature can be expressed as power laws,

$$\Sigma(R) = \Sigma_0 \left(\frac{r}{r_0} \right)^s \tag{2.5}$$

and

$$T(R) = T_0 \left(\frac{r}{r_0} \right)^q\,, \tag{2.6}$$

with a reference radius r_0, a reference density Σ_0 and a reference temperature T_0. The sound speed and aspect ratio are then given by $c_s = c_0 (r/r_0)^{q/2}$ and $h = h_0 (r/r_0)^{(q+1)/2}$. Choosing the exponents s and q appropriately, the mass accretion rate through the disk $\dot{M} = 3\pi\nu\Sigma$ is constant for an α viscosity model (Lynden-Bell & Pringle 1974). For a PPD, typical order of magnitude estimates at $r_0 = 1\,\mathrm{au}$ are $T_0 = 100$–$1000\,\mathrm{K}$, $h_0 = 0.03$–0.1, and $\Sigma_0 = 100$–$3000\,\mathrm{g/cm^2}$ (Williams & Cieza 2011).

Simulating the radiative processes with the full radiative transport equations is prohibitively expensive, as it would require following all possible paths of photons within the disk. Alternatively, PPD models often assume that the disk is locally isothermal, meaning it has a constant temperature on cylindrical shells around the star and that it does not change with time. Then, Eq. (2.6) describes the temperature in the disk for all times. This assumption can be justified when the disk cools through its surfaces on a timescale that is very short compared to the orbital period, which is expected for the outer parts of the disk at a distance of

some tens to hundreds of astronomical units. In addition to the benefit of reduced complexity of the model, assuming a locally isothermal temperature sidesteps the need of solving the energy equation Eq. (2.4c) which reduced the computational costs of numerical PPD models.

Recent studies have shown that the locally isothermal assumption causes several issues concerning the angular momentum deposition by the planetary spiral waves (Ziampras et al. 2020; Miranda & Rafikov 2020). This can result in the appearance of unphysical pressure maxima in the disk, which can influence the dynamics of gas and dust. The next simplest but still a more accurate treatment of radiative effects is the so-called β-cooling prescription (Gammie 2001), in which the temperature is relaxed back to a background state according to

$$\frac{\mathrm{d}T}{\mathrm{d}t} = -\frac{T - T_0}{\tau_{\mathrm{relax}}} \tag{2.7}$$

with the relaxation timescale $\tau_{\mathrm{relax}} = \beta/\Omega_{\mathrm{K}}$ which depends on the Keplerian angular velocity $\Omega_{\mathrm{K}} = \sqrt{\mathrm{G}M_*/r^3}$. One major advantage of this treatment of radiative processes is the possibility to utilize dimensionless units. All complexity of the radiation physics is incorporated within the single β parameter, allowing the simulation results to be scaled to different physical radii, as long as the local thermal cooling and heating rates are compatible and no other choices of physical parameters interfere.

In cases where simulations are compared to disk observations directly, the physical parameters such as the size of the disk, location of the planets and the temperature can be chosen to match the observational values. Then, heating and cooling can be treated explicitly by incorporating them into the source term S in the energy equation Eq. (2.4c)

$$S = Q_{\mathrm{visc}} + Q_{\mathrm{irrad}} + Q_{\mathrm{cool}} \tag{2.8}$$

where

$$Q_{\mathrm{visc}} = \frac{1}{2\nu\Sigma}\mathrm{Tr}(\tau^2) \tag{2.9}$$

is the viscous heating term. Irradiation from the star causes a heating rate

$$Q_{\mathrm{irrad}} = 2\frac{L_*}{4\pi r^2}(1-\epsilon)\left(\frac{\mathrm{d}\log H}{\mathrm{d}\log r} - 1\right) h\frac{1}{\tau_{\mathrm{eff}}} \tag{2.10}$$

where L_* is the luminosity of the star, ϵ the disk albedo and τ_{eff} is an effective optical depth taking into account the vertical structure of the disk (Hubeny 1990; Müller

& Kley 2012). The radiative losses from both surfaces of the disk are modeled with

$$Q_{\mathrm{cool}} = 2\sigma_{\mathrm{SB}} \frac{T^4}{\tau_{\mathrm{eff}}} \tag{2.11}$$

with the Stefan-Boltzmann constant σ_{SB}.

2.3 Planet–disk interaction

The process of planet migration can be studied using either analytical approximations in the form of linear theory, which by necessity focus on the special case of a small parameter, or by using numerical fluid dynamics simulations, which incorporate the full non-linear interaction with the downside of limited resolution and runtime constraints. The simulation strategy also poses the challenge of interpreting the results and linking patterns observed in them to underlying physical processes.

In numerical simulations, the gravitational torque exerted by the disk onto the planet can be obtained by integrating the torque density over the whole volume

$$\vec{T} = -\int \mathrm{d}V \, \vec{r}_p \times \frac{\mathrm{G}M_p \rho(\vec{r})}{|\vec{r} - \vec{r_p}|^2} \frac{\vec{r} - \vec{r_p}}{|\vec{r} - \vec{r_p}|} \,, \tag{2.12}$$

where G is the gravitational constant, M_p is the planet mass, and $\vec{r}$ and $\vec{r}_p$ are the position vectors of a point in the disk and the planet, respectively. These simulations include the full non-linear response of the disk to the perturbation by the planet, but they give no direct insight into which regions of the disk interact most strongly with the planet. Insight can be gained to some degree by evaluating the torque density, the integrand in Eq. (2.12), using suitable spatial and time averages. However, in systems with multiple planets with moderate to high eccentricities the torque density can vary strongly in time, making the interpretation of the torque density significantly more challenging.

Insight into the qualitative behavior of the interaction can be gained by analytical calculations via an asymptotic expansion of the gravitational potential of the planet in a small parameter, e.g. the eccentricity of the orbit (Goldreich & Tremaine 1979, 1980; Lin & Papaloizou 1979; Artymowicz 1993; Ward 1997). The resulting linear reaction of the disk to the perturbation and the contributions to the torque onto the planet which were identified by these authors are still the main concepts used today.

To identify the regions that mainly contribute to the torque, consider the gravi-

tational potential of a planet on a circular orbit in a polar coordinate system

$$\Phi(r, \phi, t) = -\frac{\mathrm{G}M_p}{|\vec{r} - \vec{r_p}|} \,. \tag{2.13}$$

Expressing the potential as a Fourier series yields (see, e.g. Goldreich & Tremaine 1980)

$$\Phi(r, \phi, t) = \sum_{l=-\infty}^{\infty} \sum_{m=0}^{\infty} \Phi_{l,m}(r) \cos\left(m\phi - l\Omega_p t\right) \,, \tag{2.14}$$

where Ω_p is the angular velocity of the planet, and l and m are, respectively, the indices for the radial and azimuthal decomposition. The pattern speed of each component of the potential is $\Omega_{l,m} = \Omega_p \, l/m$.

The coefficients $\Phi_{l,m}$ can be calculated which results in a dependence on the eccentricity of the planet e as $\Phi_{l,m} \propto e^{|l-m|}$. This allows one to interpret the Fourier series in terms of an asymptotic expansion. Assuming a low eccentricity of the planet ($e \ll 1$), all terms of e^2 and higher can be neglected, which effectively selects l to be equal to m or $m \pm 1$ up to first order.

Only at locations in the disk where the frequency of the response of the disk to perturbations, which is roughly the epicyclic frequency κ, matches the pattern speed of the potential, the gravitational interaction can result in a significant torque (Goldreich & Tremaine 1980). This resonance condition

$$\epsilon\kappa(r) = m(\Omega_{l,m} - \Omega(r)) \,, \quad \epsilon \in \{-1, 0, 1\} \tag{2.15}$$

can be translated to resonance locations by assuming that $\kappa(r) \approx \Omega(r) \approx \Omega_{\mathrm{K}}(r)$ to yield

$$r_{l,m} = r_p \left(\frac{m + \epsilon}{l}\right)^{2/3} \,. \tag{2.16}$$

Approximating $\kappa(r) \approx \Omega(r)$ overestimates the torque resulting from the feedback of the disk onto the planet. Thus, the $\kappa(r)$ itself has to be considered in calculating migration rates of planets (e.g. Ward 1997). $\epsilon = 0$ corresponds to corotation resonances, where the disk locally orbits with the same angular velocity as the perturbation. For $l = m$, which are the dominant modes in Eq. (2.14), this corresponds to a corotation with the planet. $\epsilon = \pm 1$ are the so-called Lindblad resonances. The resulting changes in the orbital elements as a result of the torques acting at these resonances can be estimated analytically (Goldreich & Tremaine 1980). While for $l = m$ both corotation resonances and Lindblad resonance lead to migration, higher-order modes with $l = m \pm 1$ either excite eccentricity (Lindblad) or damp it (corotation). The torque at Lindblad resonances arises from density waves that are

launched at the resonance locations and that travel in a direction away from the planet while carrying away angular momentum. The torque contribution from the inner Lindblad resonances are positive while the outer (usually dominant) contributions are negative. This density wave then gets sheared as it travels into the outer (inner) disk, where the disk orbits at a slower (faster) rate compared to the planet which results in a spiral arm pattern that orbits with the same angular velocity as the planet.

The migration behavior in viscous disks described in the literature and found in non-linear numerical simulations can be divided into four categories, which are explained in the following paragraphs.

Solid bodies in the meter to kilometer range drift towards the star due to gas drag, which is sometimes called *type 0 migration*. This process is very fast and bodies can reach the star on the order of hundreds to thousands of years (Weidenschilling 1977). With larger object mass, gas drift becomes slower and for planetesimal-sized objects with radii of 10 km and above the drift timescale becomes much larger than the disk lifetime.

At higher masses, wave torques, corotation torques and the horseshoe drag become dominant (first introduced by Goldreich & Tremaine 1979, 1980). Wave torques are a result of the gravitational interaction of the planet with the gas located at the first-order Lindblad resonances while corotation torques result from the interaction with the gas that is on horseshoe orbits around the planet. This so-called *type 1 migration* (Ward 1997) is sensitive to the properties of the disk such as the radial gradient of surface density and temperature, as well as the strength of radiative diffusion and viscosity. It can be very rapid with migration timescales on the order of 10^5 years for larger planet masses because the wave torque scales with the square of planet mass, which would result in all large planets being swallowed by their host star if this was the only mode of migration. Because the planet exchanges angular momentum with a region of the disk that coorbits with the planet, the angular momentum reservoir to be exchanged is limited. After the gas has performed one horseshoe orbit, it can not again supply or take angular momentum again. Thus, the migration speed of this type of migration depends on how efficiently the disk can supply new angular momentum to the horseshoe region which is mainly governed by the level of viscosity (for more detail, see Kley & Nelson 2012; Baruteau & Masset 2013; Paardekooper et al. 2022).

Higher-mass planets are capable of opening a gap in the disk (e.g. Goldreich & Tremaine 1980; Kley 1999). The gap opening process is governed by a balance between the removal of gas by the wave torques exerted by the planet at the Lindblad resonances and the refilling of gas into the gap region by viscous accretion and diffusion or migration of the planet. Initially, a *type 2 migration* regime was proposed in which the planet was locked inside such a gap with no material flowing through the gap and migration would only be possible together with the disk itself on its viscous timescale (Ward 1997). Multiple non-linear numerical simulations

have since shown that the planet can migrate independently of the gap, recreating it as it migrates (e.g. Dürmann & Kley 2015). While still being the subject of ongoing research, the updated type 2 migration is attributed to the wave torques acting through the spiral arms which are present in the disk interior and exterior of the planet. Qualitatively, the migration can be explained by the interaction of the spiral arms which are launched at the Lindblad resonance with the inner and outer disk (Goldreich & Tremaine 1979; Dürmann & Kley 2017). The balance of the resulting inner and outer torques yields a torque onto the planet which is net-negative for most disk conditions, causing inward migration. However, the migration speeds are much smaller compared to type 1 migration, explaining in part why not all giant planets migrated quickly into their host stars.

The final case of viscous single planet migration is *type 3 migration* (Masset & Papaloizou 2003; D'Angelo & Lubow 2008; Lin & Papaloizou 2010), which is the result of an asymmetry in the co-orbital and horseshoe regions which arise due to the migration of the planet. Because the process is dependent on the migration speed itself it can result in runaway migration leading to an exponential behavior of the semi-major axis which is either directed inward or outward, depending on the initial direction of migration. In the case of inviscid disks, the migration landscape can become even more complicated as additional effects can become dominant. For an overview of these additional processes, see McNally et al. (2019).

When planets orbit at distances such that the ratio of their periods is a rational number, they are said to be in resonance. Resonances are special dynamical configurations that can lead to increased stability of the system (Murray & Dermott 2000). For two planets, 1 and 2, with semi-major axes $a_{1,2}$ and orbital periods around the central star $P_{1,2}$, the planets are in a mean motion resonance (MMR) when $P_2/P_1 = (p+q)/p$ for some integers p and q where q is called the order of the resonance.

Due to differential migration speeds, planets can migrate into a resonance. In several resonances, planets can remain locked in the resonance, e.g. in the 3:2 and the 2:1 MMRs. Masset & Snellgrove (2001) observed an interesting consequence of the dynamical coupling of giant planets in MMR. As long as the planets are massive enough to clear a common gap and the inner planet is more massive than the outer one, the migration direction can be reversed and the pair of planets can undergo a phase of resonant outward migration.

2.4 Vortices in disks

A vortex is a patch of fluid revolving around a common center. Vortices might either be isolated in a laminar background flow or appear in a multitude. The vorticity

$$\vec{\omega} = \nabla \times \vec{u} \tag{2.17}$$

is the fundamental quantity for the characterization of vortices. Depending on the rotation direction of a vortex (in a certain definition of the coordinate system), a vortex might either raise or lower the vorticity compared to a laminar background flow.

The temporal and spatial evolution of the vorticity can be calculated starting from the fluid dynamics equations Eqs. (2.1) to yield

$$\frac{\partial \vec{\omega}}{\partial t} + (\vec{u} \cdot \nabla)\vec{\omega} = (\vec{\omega} \cdot \nabla)\vec{u} - \vec{\omega}(\nabla \cdot \vec{u}) + \frac{1}{\rho^2}\nabla\rho \times \nabla p + \nabla \times \left(\frac{\nabla\tau}{\rho} + \vec{k}\right) . \tag{2.18}$$

The term $\frac{1}{\rho^2}\nabla\rho \times \nabla p$ is called the baroclinic term. This term vanishes for a barotropic flow for which pressure is only a function of density, i.e. $p = p(\rho)$. In the case that the external force is conservative, as it is for gravity, the corresponding term $\vec{k}$ vanishes as well. Because τ depends linearly on the shear viscosity μ, the changes of vorticity due to viscous effects can be expected to scale linearly with viscosity.

In the context of thin disks, for which the vertically integrated equations are often used, the vortensity

$$\varpi = \frac{\vec{\omega} \cdot \hat{z}}{\Sigma} \tag{2.19}$$

is a useful quantity, where $\hat{z}$ is the unit vector in the vertical direction. Its evolution equation can be derived starting with Eq. (2.18) and reads

$$\frac{\partial \varpi}{\partial t} + (\vec{u} \cdot \nabla)\varpi = \frac{\nabla\Sigma \times \nabla P}{\Sigma^3} \cdot \hat{z} + \frac{1}{\Sigma}\left(\nabla \times \frac{\nabla\tau}{\Sigma}\right) + \frac{1}{\Sigma}\left(\nabla \times \vec{k}\right) . \tag{2.20}$$

In the case of an inviscid and barotropic flow subject to a conservative force, the terms on the right hand side vanish and ϖ is conserved along streamlines.

In mathematical terms, a vortex is a patch of constant vorticity that is different from a background flow (e.g. a homogenous velocity field or a rotating disk). There are exact solutions to the Euler equations (Eqs. (2.1) without viscosity) in the form of elliptical vortices (Kida 1981). Even in the case of disks orbiting a central object, analytical vortex solutions exist (Goodman et al. 1987). They also have an elliptical

shape, but this time in the $r\phi$-plane of cylindrical or polar coordinates.

From the analytical solutions for vortices in disks, it follows that the density peak is expected to follow a Gaussian bell shape elongated according to the vortex aspect ratio (Lin & Pierens 2018, see their Sect. 3.1 for a good explanation). In cylindrical coordinates, the density peak then follows

$$\rho(r, \phi, z) = \rho_p \exp\left(-\frac{(r - r_0)^2}{2\sigma_r^2} - \frac{(\phi - \phi_0)^2}{2\sigma_\phi^2} - \frac{(z - z_0)^2}{2\sigma_z^2}\right) \tag{2.21}$$

where r_0, ϕ_0, and z_0 are the coordinates of the vortex center, σ_r, σ_ϕ, σ_z are the spread of the Bell curve in each direction, and ρ_p is the peak density. For a vertically integrated 2D disk model, the last term in the exponential function is dropped and ρ is replaced by Σ. In Rometsch et al. (2021), I used the fact that vortices are patches of constant vorticity — even though the edges are smeared out by viscosity and numerical diffusion and the inside of a vortex might change due to instabilities (Lesur & Papaloizou 2009) — and the functional form of the density peak to detect and characterize vortices.

2.5 Numerical simulations

The simulation program I used in this thesis is a continuation of the FARGO code, initially developed by Masset (2000). The code is based upon a second-order upwind scheme first introduced in Stone & Norman (1992), meaning it is accurate up to second order in space and up to first order in time. Masset (2000) expanded the scheme with the *fast advection of rotating gaseous objects* algorithm (FARGO), which uses the axisymmetry present in the flow of accretion disks to allow for the use of a much larger timestep which significantly reduces computational costs.

Figure 2.1 shows a flowchart of the typical simulation workflow. At first, the simulations are initialized with equilibrium profiles of unperturbed disks. Then, simulations are allowed to adjust to the perturbations by the embedded planets over an equilibration time T_{eq}. During this time, the mass of the planet is gradually increased in order to avoid unnecessary shocks. To avoid unphysically fast migration, the planets are kept on fixed orbits by ignoring the gravitational force from the disk onto the planets until a gap has formed. After the simulation has reached a quasi-steady state, the current state of the system can be taken as the physical initial condition of the model and the planets are released and free to migrate. It then continues for the time T_{sim} which might either be dynamically chosen according to some criterion, e.g. until the planets migrated to a certain point, or predetermined due to theoretical considerations.

During the execution of the simulations, the state of the system, i.e. the main quantities ρ, ϵ, and $\vec{u}$, are regularly saved to permanent storage in order to be

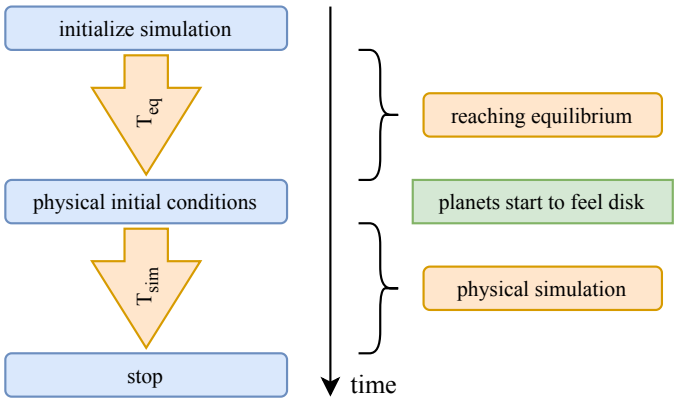

Figure 2.1: Visualization of the simulation procedure. Adapted from Rometsch et al. (2020).

able to analyze the simulations at a later point in time or to restart them after the allocated runtime expired when run on a compute cluster. Additionally, many quantities that are derived from the basic system variables are monitored, usually at a much higher frequency compared to the frequency of full outputs, which require much more storage space. These monitored quantities might be averages or sums of the system variables, such as the total mass of the disk or the average temperature, or more complex variables like the time-averaged mass flux across a simulation boundary, which can not be reconstructed from the primitive quantities due to the longer time interval between full snapshots. In addition, the properties of the planets and their orbits are usually also saved at the high output frequency.

3 Publications

This chapter introduces my publications written in the context of this thesis by describing the methodological approach and outlining my own and the contributions of my co-authors. The two publications are:

1. Rometsch et al. (2020): (paper 1)
   T. Rometsch, P. J. Rodenkirch, W. Kley, and C. P. Dullemond
   Migration jumps of planets in transition disks
   Astronomy & Astrophysics, 643, A87, November 2020

2. Rometsch et al. (2021): (paper 2)
   T. Rometsch, A. Ziampras, W. Kley, W. Béthune
   Survival of planet-induced vortices in 2D disks
   Astronomy & Astrophysics, 656, A150, December 2021

At the end of this document, publications 1 and 2 are reprinted in the versions published in the journal Astronomy & Astrophysics. They are reproduced with permission from Astronomy & Astrophysics, © ESO.

Paper 1 assesses the proposition that type II TDs can be explained by a system of embedded planets. Simulations of disks with pairs of embedded giant planets are performed to study the emerging structures in the disks and the accretion rate across the common gap and onto the planets. A parameter study is conducted by varying the mass and initial location of the planets and the disk mass, and different numerical and physical choices are considered. Furthermore, synthetic observations of the simulated systems are produced to compare the appearance to real disks. Finally, models resembling the PDS 70 system — a PPD with two accreting embedded planets — are used to assess the state of migration in this system.

This publication was created in collaboration with Peter Rodenkirch (PR), Prof. Dr. Wilhelm Kley (WK), and Prof. Dr. Cornelis Dullemond (CP). All the simulations and analysis of the results were performed by me. Most of the manuscript was written by myself with two exceptions. The introduction and summary were partly provided by WK and the synthetic observations and the section describing them were produced by PR.

In paper 2, the lifetime of properties of vortices that are created by the growth of giant planets is revisited with improved treatment of radiative processes while

varying the viscosity parameter and conducting a detailed resolution study. Simulations are conducted with two simulation codes using different numerical schemes, `FARGO` and `PLUTO`, in order to fortify the validity of the numerical results.

The paper was written in collaboration with Alexandros Ziampras (AZ), Prof. Dr. Wilhelm Kley (WK), and Dr. William Béthune (WB). The majority of models were simulated with both simulation codes. AZ conducted the `PLUTO` simulations and the `FARGO` simulations were done by myself. Analysis of the simulations was done in collaboration with AZ. In order to extract vortex properties out of the simulation output, I developed a new methodology that enables automatic detection and analysis of vortices. This framework is available as a `Python` library under `https://github.com/rometsch/vortector`. AZ and I contributed to all parts of the paper while WK and WB mainly provided feedback and WK contributed a few passages throughout the paper. AZ wrote most of the methodology section, the appendix about numerical convergence, and the discussions about in-plane radiation transport and the differences between the two codes. The rest of the paper, i.e., the introduction, the results sections, the remaining discussions and the summary were mostly written by myself.

4 Results

This chapter summarizes the most important results from the publications presented in Chapter 3 and adds some additional findings. Its starts with the study of the dynamical evolution of embedded planetary systems and the reproduction of the observable characteristics of type II TDs by the models. This is followed by the description of the newly discovered phenomenon of migration jumps and finally, the study of planet-induced vortices and their properties is presented. The results are discussed later in Chapter 5.

4.1 Planetary systems can shape type II transition disks

Paper 1 studied the evolution of a system of two planets in the range of 3 to 9 Jupiter masses (M_J) which were embedded in a disk. The system was simulated in two dimensions (see Sect. 2.2) in the $r\phi$–plane using the `FARGO` code. Planets were treated as point masses with a smoothed potential and were allowed to interact gravitationally with the disk and each other. They were also allowed to accrete mass from their surroundings. The disk was treated as a viscous gas which was assumed to be either locally isothermal or to follow the ideal gas law with the inclusion of viscous heating, irradiation from the star, and radiative cooling off the disk surfaces (see Sect. 2.2).

Two different behaviors were observed for the migration of the pair of embedded planets. While for any ratio of planet masses tested the planets engaged in a 2:1 resonance, more massive outer planets caused the planets to migrate inward. For a more massive inner planet, the migration was reversed and directed outward (mass ratios of 2:1 and 3:1 were tested). This is in line with the results of previous numerical studies which found outward migration for a pair of planets in MMR (Masset & Snellgrove 2001; Pepliński et al. 2008; Crida et al. 2009). In addition to smooth inward and outward migration, a new migration phenomenon was observed for which the outer planet can migrate very quickly, leaving the common gap, only to return to the MMR with the inner planet shortly after. This phenomenon is presented in Sect. 4.2.

To be able to compare the numerical results to observations of TDs, the accretion rate onto the central star $\dot{M}_*$, which is one of the characteristic observables of TDs, was monitored throughout the simulations. For outward migration, $\dot{M}_*$ was significantly higher compared to the inward migration, up to more than one order of magnitude (see also Fig. 9 in paper 1 for an illustrative example). The increase

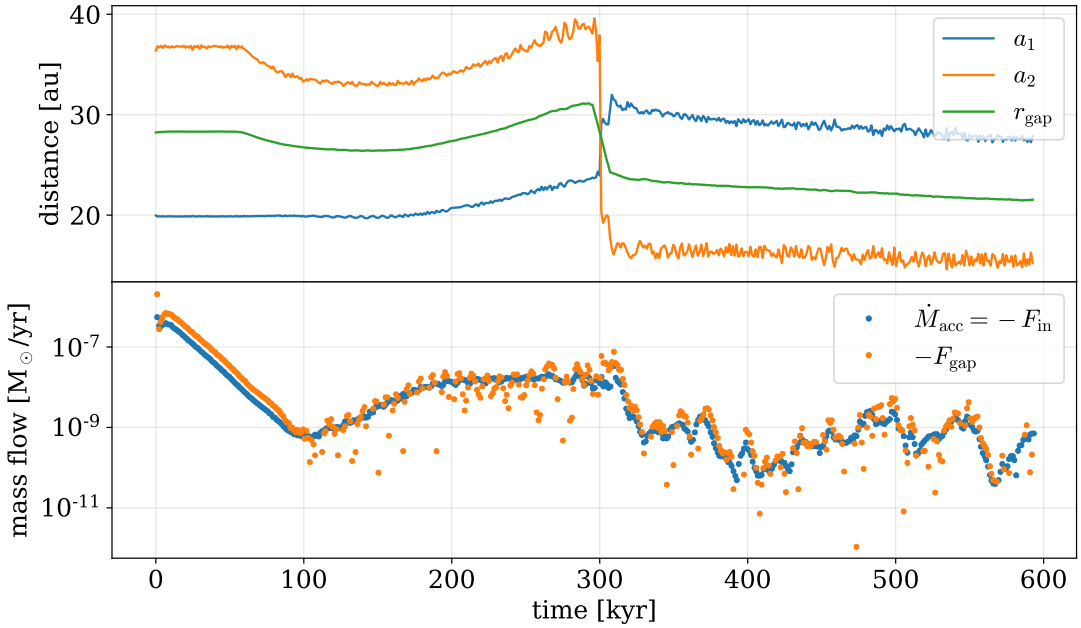

Figure 4.1: Mass flow through the planetary gap and accretion rates in dependence of the migration direction. Top: semi-major axis of the two planets $a_{1,2}$ and the gap location $r_{\mathrm{gap}} = (a_1 + a_2)/2$ (smoothed over 0.52 kyr). Bottom: mass flow through the inner boundary F_{in} (which is identified with $\dot{M}_{\mathrm{acc}}$) and through the gap F_{gap}. The data is taken from model `L` in paper 1 (see Fig. 9 therein).

results from an exchange of angular momentum between the planets and the disk. As they migrate outward, they gain angular momentum which must be supplied by the disk material. In turn, the gas in the disk loses angular momentum which results in some of the gas moving inward. This shoveling action of the planets demonstrates that a wide common planetary gap is no barrier to gas accretion. Mass accretion in the simulated disk was as high as $10^{-7}\,\mathrm{M}_\odot/\mathrm{yr}$, an order of magnitude higher than the viscous mass accretion rate of the unperturbed disk of $\sim 10^{-8}\,\mathrm{M}_\odot/\mathrm{yr}$. The increase is only present during phases of outward migration and disappears for inward migration. The mechanism is, therefore, able to produce the mass accretion characteristic of type II TDs.

To support the argument that mass flow through the common planetary gap F_{gap} is responsible for the increase in stellar mass accretion $\dot{M}_{\mathrm{acc}}$, I calculated F_{gap} for model `L` (outer boundary at 502 au) from paper 1. In this model, the pair of planets first migrates outward via the Masset–Snellgrove mechanism before they swap their order, resulting in a configuration where the pair of planets migrates back inward. Thus, the model shows the consequences of outward and inward migration for mass

accretion onto the star.

Figure 4.1 shows the time evolution of the semi-major axis of both planets $a_{1,2}$ and the gap location $r_{\rm gap}$ (top), and the mass flow through the inner boundary $F_{\rm in}$ and through the gap $F_{\rm gap}$ (bottom). The gap location is defined to be $r_{\rm gap} = (a_1 + a_2)/2$ which is then averaged over a rolling window of 0.52 kyr to avoid strong fluctuations. The mass flow through the gap, $F_{\rm gap}$ is calculated by tracking the change of the mass interior to $r_{\rm gap}$, $M_{\rm in}$, and the mass flow through the boundaries. Using the conservation of mass, the flow through the gap then follows from $\dot{M}_{\rm in} + F_{\rm gap} + F_{\rm in} = 0$. The mass flow through the inner boundary $F_{\rm in}$ is an output variable of the simulations. The change of the mass of the inner disk $\dot{M}_{\rm in}$ is calculated from the density field in the simulation output data by summing up the mass interior to $r_{\rm gap}$ and using a first-order time derivative. In paper 1, the mass flow through the inner boundary was identified with the accretion onto the star, thus, $\dot{M}_{\rm acc} = -F_{\rm in}$.

The top panel of Fig. 4.1 shows the change from outward to inward migration at $t \approx 300$ kyr as a consequence of the more massive planet moving to the outside of the pair. During the time that planets are on fixed orbits (until 64 kyr) and up to around 100 kyr, the accretion rate drops as the inner disk is accreted away through the inner boundary. At around 100 kyr the trend reverses, as the planetary orbits get more eccentric and more mass is transferred through the gap. The bottom panel of Fig. 4.1 illustrates the connection between $F_{\rm gap}$ and $\dot{M}_{\rm acc}$. As more mass is shoveled across the gap, accretion also rises. This is due to the increase in surface density in the inner disk which is then accreted onto the star.

By the process of outward migration, the outer planet can easily reach tens of astronomical units. Therefore, the common planetary gap can extend out to similar distances. Though not simulated in paper 1, dust can be expected to stop close to the outer gap edge. Just outside the outer gap, a radial pressure maximum exists, which acts as a barrier for dust drift (Weidenschilling 1977). In the inner disk, dust drift can continue unhindered while the dust accretion from the outer disk is stopped. This causes the inner disk to become devoid of gas on a short timescale (Marzari et al. 2019; Bae et al. 2019). Following this line of argument, the location of the outer gap edge with its pressure maximum corresponds to the distance from the star inside of which nearly no dust is present in the disk anymore. This missing dust in the inner parts of the disk would then show up as a large hole in continuum dust emissions of these disks or as missing near-infrared flux (see Fig. 10 of paper 1) which reproduced the second characteristic property of type II TDs.

Figure 4.2 shows a combination of TD observations and selected disks from the simulations in a $\dot{M}_{\rm acc}$–$r_{\rm hole}$ diagram. It summarized the previous two results and contextualizes the simulations in paper 1 by placing the disks from the models at different times during their evolution in the same diagram as observational data from Ercolano & Pascucci (2017) and the parameter space which can be explained by X-ray photoevaporation (Picogna et al. 2019). The orange shaded region encloses the area of the parameter space which was explained by X-ray photoevaporation

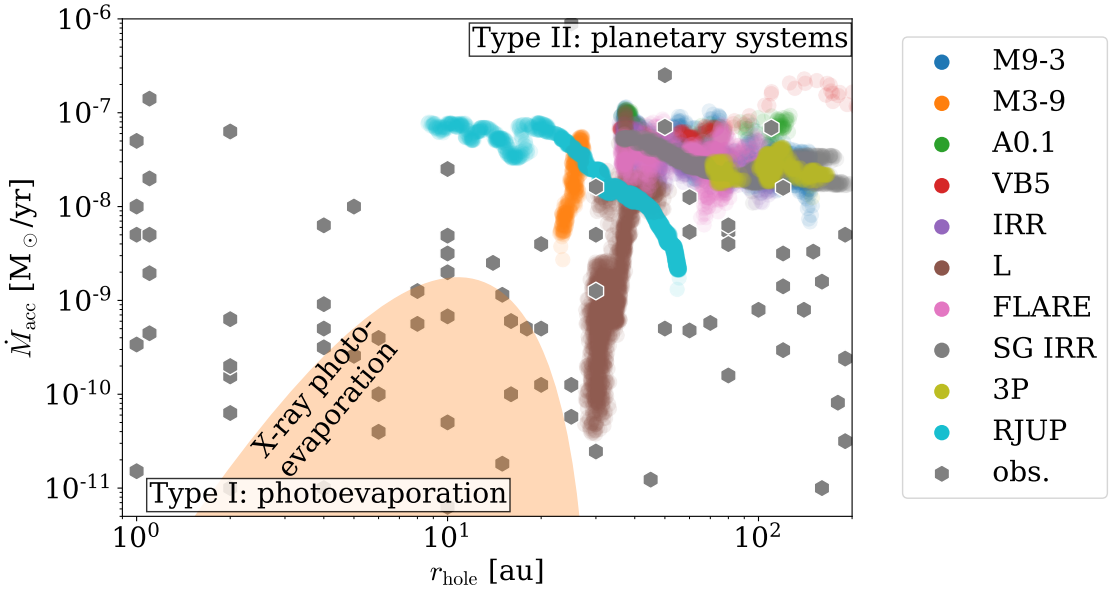

Figure 4.2: $\dot{M}_{\rm acc}$–$r_{\rm hole}$ diagram showing observed TDs (gray hexagons), planetary system models (colored data points as indicated in the legend), and the parameter space explained by X-ray photoevaporation (orange shaded area). The observational data is reproduced based on Fig. 5 of Ercolano & Pascucci (2017). The parameter space explained by X-ray photoevaporation is extracted from Fig. 10 in Picogna et al. (2019). Planetary system models are taken from paper 1 (refer to Table 1 therein for simulation parameters of the model names in the legend) where the $r_{\rm hole}$ is assumed to be the location of the outer planet. For these models, data points throughout the evolution of the system are shown resulting in streaks of data points. The `3P` model is the one discussed in Sect. 4.2 and the `RJUP` model is analogous to the `M9-3` model but with the planet initialized further in such that the inner planet starts at 5.2 au.

models in Picogna et al. (2019) (see the center panel of Fig. 10 therein). The mass accretion rate $\dot{M}_{\rm acc}$ is calculated as the mass flow over the inner simulation boundary and the hole size is taken to be the apastron distance to the star of the outer planet which is an approximation to the location of the outer gap edge. Each simulation data point, represented by a semi-transparent colored circle, was sampled from the respective simulation from paper 1, where each sample is 0.24 kyr apart from the last one. The dynamical evolution of the system then creates the colored streak as the system moves through the parameter space. Table 1 in paper 1 explains the meaning of the names in the legend, except for the `3P` model which has three embedded planets (see Sect. 4.2) and the `RJUP` model which has the inner planet initialized at $r = 5.2$ au and the outer planet just outside 2:1 MMR.

Most simulation data points cluster in the r_{hole} range between 36.4 au (the initial location of the outer planet) and 140 au, and between $\dot{M}_{\mathrm{acc}} = 10^{-8}$–$10^{-7}\,\mathrm{M}_{\odot}/\mathrm{yr}$ which is above the viscous accretion rate of the unperturbed disk $\dot{M}_{\mathrm{visc}} = 3\pi\nu\Sigma = 5 \times 10^{-9}\,\mathrm{M}_{\odot}/\mathrm{yr}$ at $r = 2\,\mathrm{au}$. There are three apparent exceptions to this behavior. The first is the `M3-9` model (orange) in which the inner planet is less massive than the outer planet, in which migration is directed inward and the system moves towards the lower left as r_{hole} decreases due to the inward migration and $\dot{M}_{\mathrm{acc}}$ shrinks as the inner disk is accreted away. The same effect happens for the `L` model (brown), which nearly reaches the parameter space explained by X-ray photoevaporation. Model `RJUP` on the other side has an outward migrating pair of planets that starts further in. It moves towards the lower right as r_{hole} increases while $\dot{M}_{\mathrm{acc}}$ decreases again as the disk is accreted away.

In summary, we see that outward migrating pairs of planets can lead to an increased mass accretion rate while reaching large distances to their host star at the same time. Hence, this scenario can explain the two dynamic characteristics of type II TDs, mass accretion rate and hole size.

4.2 Migration jumps

Aside from the explanation for type II TDs, the parameter study in paper 1 revealed a new phenomenon which I called a *migration jump*. An example of a migration jump for a system with a $9\,\mathrm{M_J}$ inner planet and $3\,\mathrm{M_J}$ outer planet is shown in Fig. 4.3. From top to bottom, the panels show the semi-major axis, eccentricity, and the 2:1 and 4:1 MMR angles for the inner and outer planet in orange and blue, respectively. If an MMR angle is librating, the planets are in the respective MMR. The migration jump is visible as the peak in the semi-major axis of the outer planet.

For models exhibiting outward migration via the Masset–Snellgrove mechanism, a vortex formed in the outer disk. Due to mutual gravitational interaction between the planets, eccentricities build up before the migration jump, where especially the eccentricity of the inner planet undergoes a steady increase. The eccentricity and semi-major axis of the outer planet begin to fluctuate substantially before the migration jump, which is a sign of interaction with a vortex.

Just before the migration jump, the inner planet loses eccentricity and thereby increases its angular momentum — the angular momentum of a planet is given by $L = M_{\mathrm{p}}\sqrt{a(1-e^2)}$ — which is supplied by the outer planet. The outer planet in turn decreases its angular momentum by gaining eccentricity. This gain in eccentricity is sufficiently large for the outer planet to come into contact with the outer gap edge which gives the outer planet access to gas in its co-orbital region and triggers a phase of type 3 rapid outward migration (see Sect. 2.3). The planet migrates several tens of au in only a few thousand years.

As a consequence of the type 3 migration, the eccentricity of the outer planet is

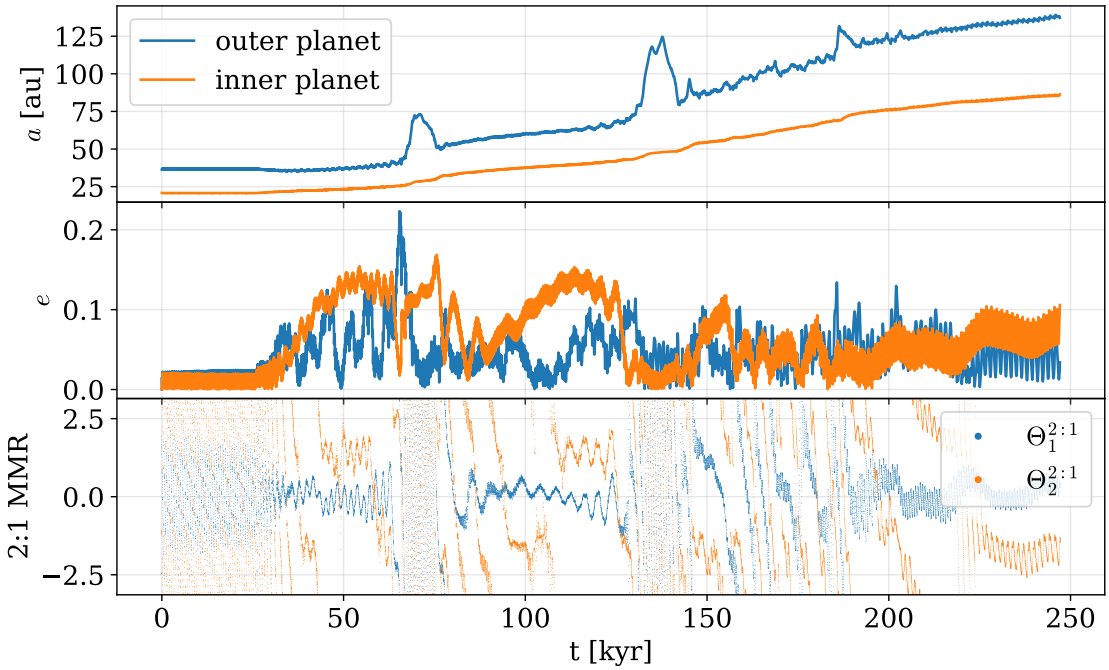

Figure 4.3: Migration jumps as seen in the time evolution of orbital elements of a system with two massive embedded planets. From top to bottom, the panels show the semi-major axis, eccentricity, and the 2:1 MMR resonant angles for the inner and outer planet in orange and blue, respectively. The figure shows the `M9-3` simulation (9 M_J inner and 3 M_J outer planet) from paper 1 (see Fig. 4 therein) over its full duration.

dampened down by about an order of magnitude. Rapid outward migration stops, roughly after the planet passed the radial extent of the vortex. For some cases, this stopping location coincides with another MMR (4:1 with the inner planet in the example case), but no direct link between the stopping location and MMR locations could be established in general. After spending several thousand years at the stopping location, the planet then quickly migrated back inward into 2:1 MMR with the inner planet over a span of, again, only several to tens of thousands of years.

The process can then repeat, given that the disk is large enough to accommodate the outward movement. Inspired by the relative quickness and the back and forth movement I called this phenomenon a *migration jump*.

From the set of simulations carried out in paper 1, three conditions for the occurrence of migration jumps can be extracted:

1. the embedded planets must be gas giants that open a common gap,

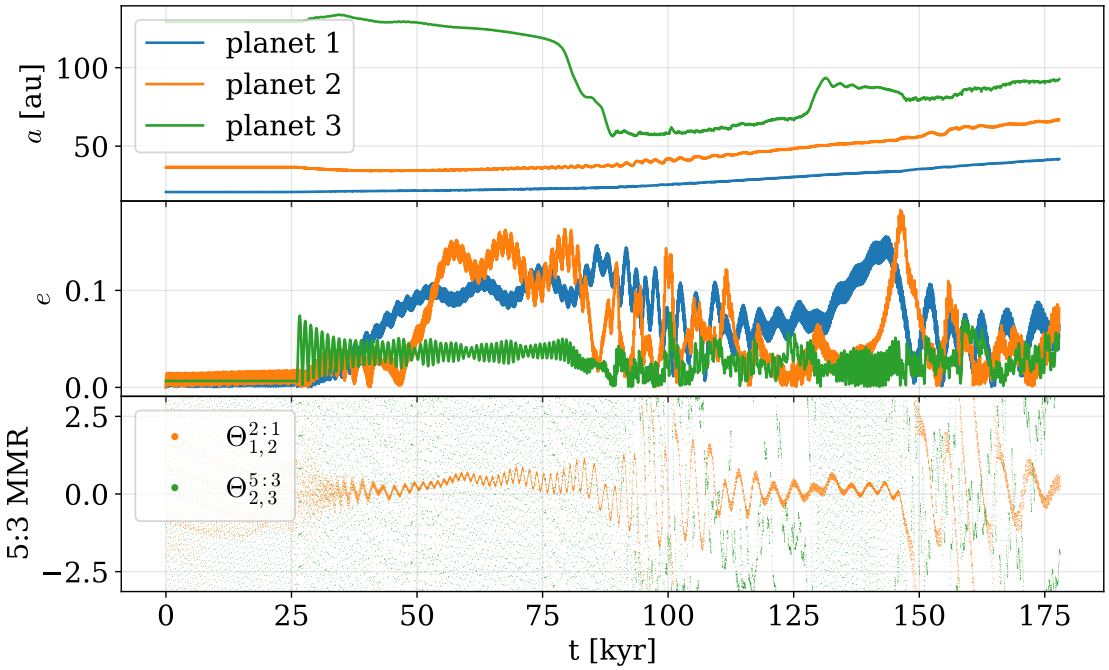

Figure 4.4: Migration jump in a system of three embedded giant planets (9, 3, and 1 M_J from inside out). From top to bottom, the panels show the semi-major axis, eccentricity, and MMR resonant angles. The mean motion angles are for a 2:1 MMR for the inner pair (orange) and a 5:3 MMR for the outer pair (green). At 26 kyr, the planets are released from the initial fixed orbits.

2. the inner planet must be more massive than the outer one to facilitate resonant outward migration, and

3. the disk must be massive enough such that the outward migration rate is high enough to cause vortex formation and the triggering of type III rapid migration.

To test the robustness of the phenomenon, analogous simulations with pairs of embedded planets were carried out while varying the choices of physical and numerical parameters. The variations include

- resolutions higher and lower by a factor of $\sqrt{2}$ in each direction,
- different equations of state including locally isothermal with a flared and non-flared disk, and ideal gas with radiative cooling, viscous heating, and irradiation,
- different domain sizes with $r \in [2.08, 520]$ au,

- the inclusion of planetary accretion,
- outflow, reflective, and viscous damping inner boundary conditions with and without a wave-damping zone, and
- the inclusion of self-gravity.

Migration jumps appeared in all of the tested combinations as long as the three conditions mentioned above were fulfilled.

As an extension to paper 1, I checked for the existence of migration jumps in systems with three embedded planets by modifying the fiducial `M9-3` model by adding a third planet. Figure 4.4 shows the results of a simulation with a chain of three planets with masses of 9, 3, and 1 M_J from the inside out. The figure shows, from top to bottom, the semi-major axis and eccentricity for all three planets and two MMR angles. For the inner and middle planets, the 2:1 MMR angle is shown in orange and for the middle and outer planets, the 5:3 MMR angle is shown in green.

The inner two planets were again initialized close to 2:1 MMR and the outer planet was initialized further out at 130 au. If the planet is initialized further in, the outer planet pair can enter into 2:1 MMR earlier than the inner pair resulting in a situation in which the inner planet is left behind and the outer pair migrates outward, which effectively results in a two-planet case again.

A migration jump is observed for the outer planet at around 130 kyr. In the case of three planets, the situation is slightly different compared to the explanations above. The inner two planets are in 2:1 MMR and the outer planets are in 5:3 MMR before and after the migration jump, which is shown by the libration of the respective 2:1 and 5:3 MMR angles in the bottom panel of Fig. 4.4. Additionally, there is not one large-scale vortex developing in the outer disk but multiple small vortices and the eccentricity of the outer planet just before the jump is smaller. Nonetheless, this result demonstrates that the Masset–Snellgrove effect also works for a resonant chain of 3 planets and that migration jumps also happen in such a configuration.

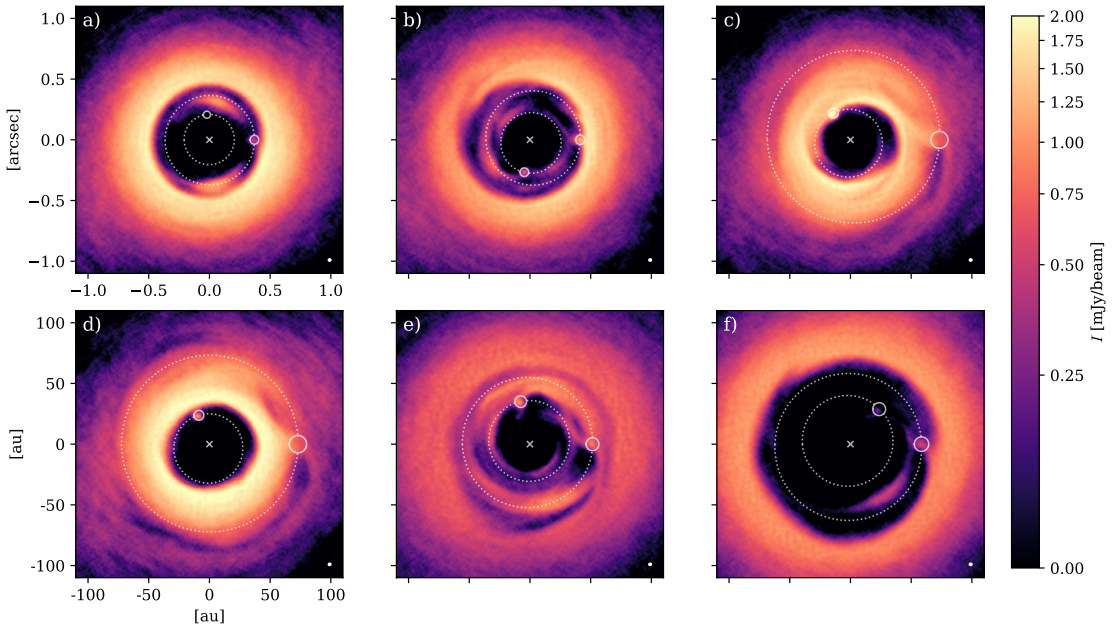

Figure 4.5: Simulated ALMA observations at 855 μm of the disk in model `M9-3` in paper 1 with a beam size of 33 × 30 mas where the disk is assumed to be face-on located at 100 pc distance. The panels show the disk prior (a and b), during (c and d), and after (e and f) the migration jump. The location of the star is indicated by the × symbol, the location of the planets and the size of their Hill spheres are shown with white circles and the instantaneous planetary orbits are marked with dotted lines. Taken from paper 1.

4.3 A bridge between models and reality

With the advent of high-resolution disk observations with ALMA (ALMA Partnership et al. 2015), substructures inside of PPDs became accessible by observational means. This means that direct links between the structure of model disks and observations can be made.

To simulate how the model disks would appear in ALMA observations, the two-dimensional models were first expanded to three-dimensional models by assuming the disks to be in hydrostatic equilibrium at every point in the disk and then expanding the vertically integrated surface densities to volume densities. Additionally, it was assumed that the dust is distributed with a constant dust-to-gas ratio of 1 % throughout the disk and that the dust size distribution follows an MRN distribution (the number density of dust particles with size a scales as $n(a) \propto a^{-3.5}$). Then, the dust temperatures due to irradiation from the central star and thermal emission

were simulated using the Monte-Carlo radiative transfer code `RADMC3D` (Dullemond et al. 2012). Finally, an ALMA observation at 855 μm for the disk located face-on at a distance of 100 pc was simulated using the `CASA` package (McMullin et al. 2007), making use of the best capabilities of the ALMA observatory.

Figure 4.5 shows simulated observations from the fiducial `M9-3` model from paper 1 prior (panels a and b), during (panels b and c) and after the first migration jump. The location of the star is indicated by the cross in the center of the panels, the instantaneous orbits of the planets are shown with dotted white lines and their location is shown with white circles which also show the size of the corresponding planet's Hill sphere. Prominent features include a lopsided structure due to the vortex (panel b) where the planet is close to the outer gap edge, voids behind the planet during the migration jump (panels c and d), and material inside of the gap region (panel e and f). These features can be regarded as observational tracers of strong dynamic interactions of planets with their host disks.

To make the link between models and reality stronger, a model was tuned to the PDS 70 system (which has observational parameters compatible with the scenario studied in the models in paper 1) and the observability of a migration jump was assessed for this case. To this date, PDS 70 is the only system in which planets were observed embedded in a PPD while still accreting (Haffert et al. 2019). Located at a distance of 113.43 ± 0.52 pc (Gaia Collaboration et al. 2018), PDS 70a is a $0.76 \pm 0.02\,M_\odot$ star (Müller et al. 2018) and the two giant planets are located at a distance of 20.6 ± 1.2 au and 34.5 ± 2 au (Keppler et al. 2018, 2019; Haffert et al. 2019) with masses estimated to be between 5–14 M_J and 4–12 M_J (Haffert et al. 2019). The results of the PDS 70 models indicate that the mass of its disk is too low for a migration jump to occur, but if it were sufficiently high, it would be observable as an arc-like feature intruding into the gap region in very high-resolution observations (see Fig. 12 in paper 1).

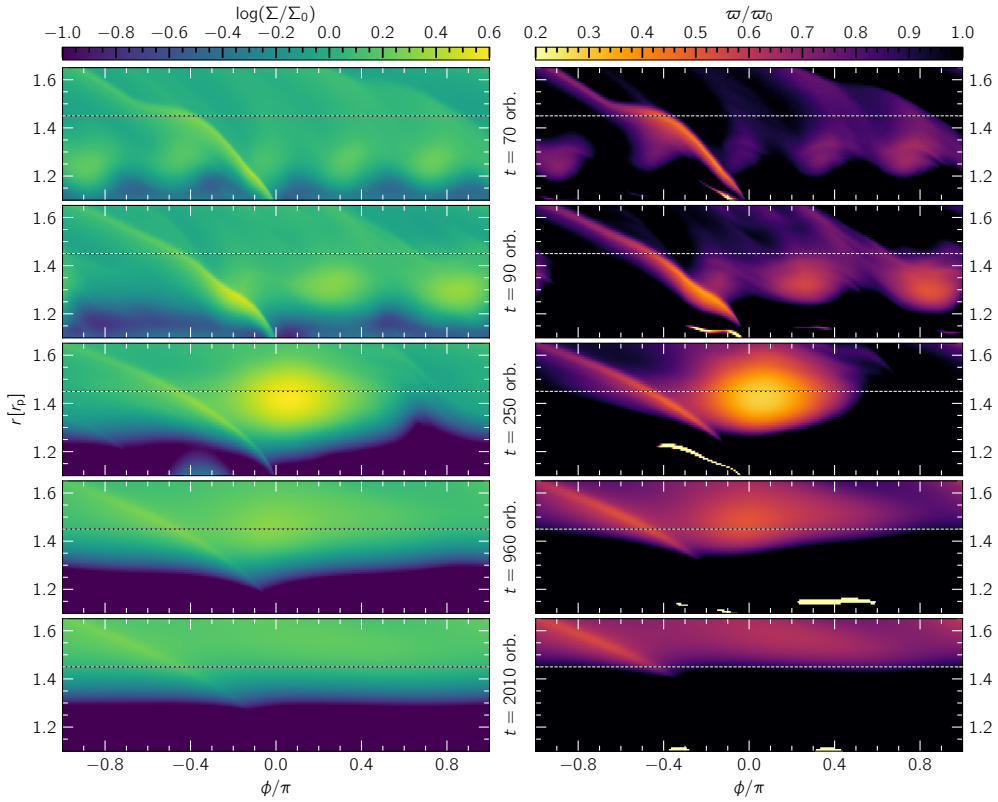

Figure 4.6: Typical life track of a vortex formed at the outer gap edge caused by a growing giant planet. In each panel, the planet is located at $\phi = 0$ and $r = 0$, outside of the panel towards the bottom center. The left column shows the surface density and the right column shows the vortensity, each normalized by the initial profile. Vortices correspond to bright spots in both quantities. The horizontal dashed lines mark the final location of the vortex. From top to bottom, the rows show the emergence of multiple small vortices due to the RWI, the merging of the small vortices into one large-scale vortex and its subsequent decay. Taken from paper 2.

4.4 Vortices

Substructures such as gaps and rings are inevitable in the presence of embedded giant planets. Additionally to these axis-symmetric disk substructures, lopsided substructures frequently appear due to the interaction of the planets with the disk. Large-scale vortices play an important role in the migration jump phenomenon and are also expected to be detectable in observations due to their property of accumulating dust particles (Marel et al. 2013; Bae et al. 2016).

In paper 2, planet-induced vortices in PPDs were studied by means of two-dimensional fluid dynamics simulations using the `FARGO` and `PLUTO` codes, thus employing two different numerical schemes. The gas was assumed to be an ideal gas with radiative processes being parameterized by the β formalism and viscosity following the α model. A focus was put on vortices emerging at the outer edge of the gap created by a single Jupiter mass planet, treated as a non-accreting point mass, which was artificially grown over a timescale of 100 or 1000 planetary orbits.

The typical life track of a vortex in the simulations is visualized in Fig. 4.6. It shows the region of the disk just outside the planet for different stages during its lifetime. The left and right columns show the normalized surface density and vortensity, respectively. Vortices are visible as bright spots on either side. The bright streak on the left side of each panel is the planetary spiral arm. The life track begins with the embedded planet carving a gap in the disk as its mass is increased over 100 or 1000 orbits. The gap edge steepens as the gap becomes deeper triggering the RWI (Lovelace et al. 1999). Multiple small vortices form (top row) which successively merge (second row) into one large-scale vortex (center row) over less than the planetary growth time.

Figure 4.7 shows an overview of the vortex lifetimes as a function of the cooling timescale parameter β (see Sect. 2.2) where results from simulations at 8 cps and 16 cps are shown on the left and right, respectively. The viscous α is encoded with color and the symbol shape refers to the simulation code. Vortex lifetime increases for decreasing α, which is the expected behavior (Godon & Livio 1999; Val-Borro et al. 2007; Ataiee et al. 2013; Fu et al. 2014; Regály & Vorobyov 2017). While vortices decay nearly immediately for $\alpha = 10^{-3}$, they live for up to 1000 orbits for $\alpha = 10^{-4}$ and up to several thousand orbits for even lower α. In simulations with self-gravity, the initial vortices did not merge into one large vortex but remained as two to three separate smaller vortices which then decayed faster leading to reduced lifetimes. This consistent with earlier studies (Lovelace & Hohlfeld 2013; Zhu & Baruteau 2016; Regály & Vorobyov 2017; Pierens & Lin 2018).

In contrast to previous numerical studies, increasing the planet growth timescale from 100 to 1000 planetary orbits only extended the vortex formation process (Hammer et al. 2017). After the vortex has fully formed, the decay process is nearly identical for both planet growth timescales (see also Fig. 6 in paper 2).

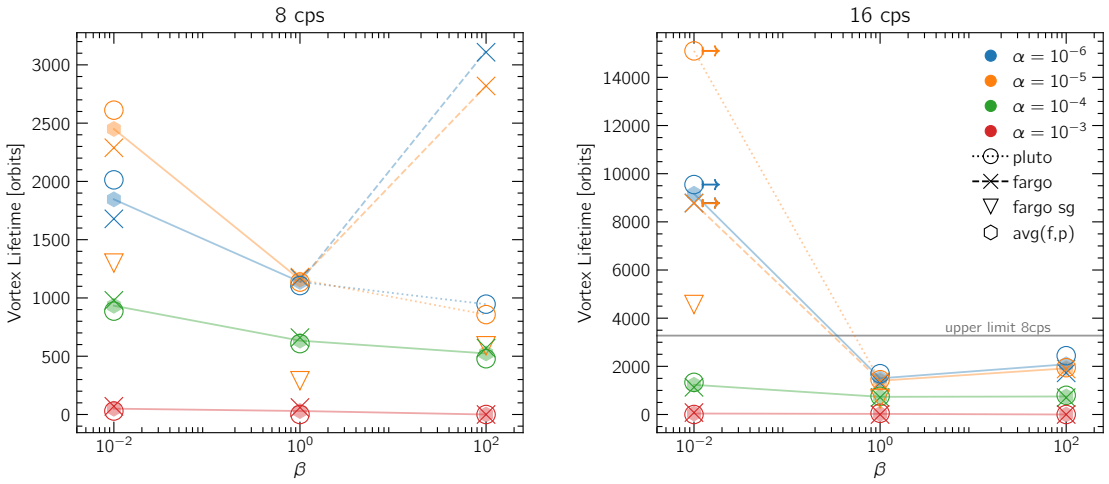

Figure 4.7: Vortex lifetime as a function of the β-parameter for different choices of α. The left and right panels show lifetimes for resolutions of 8 cps and 16 cps, respectively. Circles indicate `PLUTO` results, crosses and triangles indicated `FARGO` results without and with the inclusion of self-gravity, respectively, and hexagons indicate an average between `PLUTO` and `FARGO` results. Lines are added as visual guides to highlight trends. Note the increase of lifetime with α, the decrease of lifetime for the inclusion of self-gravity, and the long-lived vortices for $\beta = 0.01$ and low α at 16 cps. Taken from paper 2.

The dependence of vortex lifetime on the cooling parameter β in the presence of a planet is one of the new results of the study. For $\alpha = 10^{-3}$ and 10^{-4}, the lifetime decreases with increasing β whereas for lower α the shortest lifetimes are observed for $\beta = 1$. While there is a discrepancy between the results of the two simulation codes in the lower resolution 8 cps simulations, the results agree well with a resolution of 16 cps. For the higher resolution case with $\alpha \leq 10^{-5}$, vortex lifetimes are around 2000 orbits for $\beta = 1$, slightly higher for $\beta = 100$, but significantly higher for $\beta = 0.01$ with lifetimes exceeding 10 000 orbits. The excess in lifetime indicates that vortex evolution happens in a separate, long-lived regime for $\beta = 0.01$ with $\alpha \leq 10^{-5}$, which is only resolved at higher resolutions.

In models with a long-lived vortex, the vortex was observed to migrate outward towards a second pressure bump (Paardekooper et al. 2010). The second pressure dump is a result of the vortex spiral arms transporting angular momentum. Between the migrated vortex and the planet, additional short-lived vortices formed in some cases. One such example is illustrated in Fig. 4.8 which shows a 16 cps `FARGO` model with $\alpha = 10^{-6}$ and $\beta = 0.01$ as analyzed by the `vortector` tool.

In summary, the results in paper 2 show that the lifetime and properties of vortices are sensitive to the thermodynamics of the disk, the viscosity, the inclusion

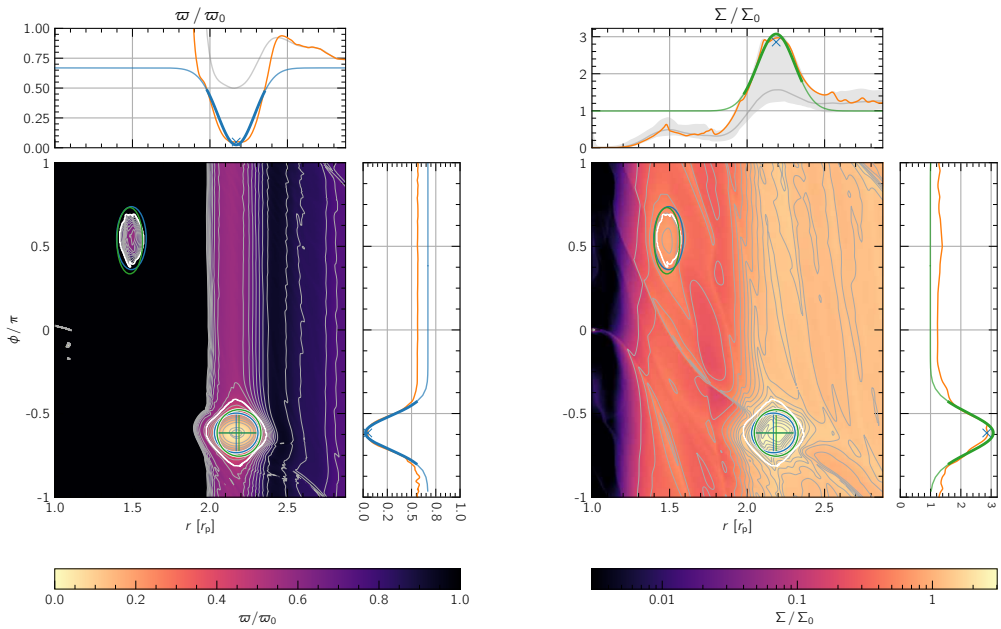

Figure 4.8: A long-lived vortex that has migrated outward and a secondary short-lived vortex to its left in the FARGO model with $\alpha = 10^{-6}$, $\beta = 0.01$, and 16 cps resolution at time $t = 7150$ orbits. The left and right panels shows vortensity and surface density, respectively, normalized by the values of the initial conditions. The two vortices which are detected by the vortector tool are marked by the ellipses indicating the full width at half maximum of the Gaussian fits of vortensity (blue) and surface density (green). To the sides of the heatmap panels, radial (top) and azimuthal (right) cuts through the main vortex (marked by the crosshair) are shown. Reproduction of Fig. B.2 in paper 2.

of self-gravity, and choices concerning the numerics of the simulations. Special care has to be taken in the simulations of large-scale vortices to resolve the physics, as seen by the dependence of vortex lifetime on resolution. Vortices are strongest and live longest for low viscosity, short cooling timescales and low disk masses due to the weaker effects of self-gravity.

5 Discussion and outlook

This chapter discusses the results presented in Chapter 4 and provides an outlook on the different topics. The sections cover the explanation of type II TDs, migration jumps and the complex interactions of multi-planet systems, large-scale vortices, and the comparison of models to observations.

5.1 Explaning transition disks

Two of the three characteristics of type II TDs as defined by Owen (2016) were shown to be explained by a system of embedded planets in paper 1: the wide hole sizes of tens of astronomical units and the large accretion rates. Fig. 4.2 shows that the outward migration scenario can explain the large $r_{\rm hole}$ and high $\dot{M}_{\rm acc}$ quadrant of the parameter space of observed TDs, extending the region already explained by X-ray photoevaporation (Picogna et al. 2019). The third characteristic property, the mm-brightness, is still missing in the explanation. At this stage of the models, however, the mm-brightness of the disks can not be reliably assessed because it depends on too many unknowns, such as the dust distribution and the dust properties and opacities, all of which were not addressed in the models and leave room for improvements in many directions.

The models in paper 1 were not tuned to reproduce the largest possible area of the parameter space, but the parameters were simply an estimate to achieve a mass accretion rate of the order of $10^{-8}\,\mathrm{M}_\odot/\mathrm{yr}$. The area of parameter space covered by the dynamical evolution of the embedded planetary system is therefore remarkable. The fact that no fine-tuning is required can be taken as an indication that the outward migration scenario is indeed a viable option to explain type II disks.

From the tendency of $\dot{M}_{\rm acc}$ to decrease over time in the planetary scenario with a viscous disk model, it can be expected that more of the parameter space below $\dot{M}_{\rm acc} = 10^{-8}\,\mathrm{M}_\odot/\mathrm{yr}$ can be explained by simply evolving the models for a longer time. Viscous mass accretion scales as $\dot{M}_{\rm visc} = 3\pi\nu\Sigma$ (Lynden-Bell & Pringle 1974), and therefore two additional possibilities to lower $\dot{M}_{\rm acc}$ are using lower α values or using models with lower initial disk masses. However, the limits of these basic scaling arguments are not yet known. One natural question in this context is, how much of the parameter space can actually be explained by varying the parameters of the planet models and where the limits of this scenario lie.

A possible improvement to this study is the inclusion of dust particles of micrometer to centimeter sizes in the simulations in a similar way as done by Marzari et al. (2019) and additionally monitoring the accretion rates of solids across the common

planetary gap, as well as the accretion of solids onto the planets and onto the star. The version of the FARGO code used in this thesis is already equipped with a module for the evolution of small solid particles. This would need to be extended by a model of dust diffusion, otherwise, all dust particles with a Stokes number close to unity would end up in pressure maxima such as vortices, having no restoring force that moves them away from the pressure maxima after they drifted there. Smaller dust particles are well coupled to the gas and trace its density distribution and are not susceptible to the pressure gradients to such a large degree and even larger particles are decoupled from the gas enough and practically unaffected by dust traps. The availability of information about the distribution of millimeter-sized dust in the disks would also improve the predictive power of synthetic observations because those presented rely on the assumption that the millimeter-sized dust is distributed exactly like the gas is distributed. However, in a more realistic model, the dust is actually filtered at the outer gap edge and accumulates in vortices (Marzari et al. 2019). Additionally, having access to the dust distribution would allow for an informed measurement of the mm-brightness of the model disks, addressing the third characteristic property in the Owen (2016) TD classification.

5.2 The complex dance of disk and planets

Migration jumps are presented in Sect. 4.2. They are a composite phenomenon where the dynamical gravitational interaction between the planets and the interaction with a vortex in a disk lead to emergent behavior. To my knowledge, paper 1 contains the first description of this process. However, the phenomenon previously appeared unmentioned in the literature, e.g. in Fig. 7b of Chametla et al. (2020).

With the range of physical and numerical choices that were tested, one can be confident that the migration jumps are not a numerical artifact but indeed a physical feature of the model. Further study of this phenomenon could go in several directions. The local conditions in the disk during the migration jump need to be investigated in more detail as the study in paper 1 left some questions unanswered. Why does the planet stop at a specific location, and why is it sometimes a resonance location with the inner planet? What determines the migration speed back into resonance? What role does the vortex play in determining these processes?

Reproducing the phenomenon with another code than FARGO would further evidence that the phenomenon is indeed physical. Following the publication, I tested an equivalent setup with the FARGO3D code (Benítez-Llambay & Masset 2016) which also showed a migration jump. However, FARGO3D is based on the same ZEUS2D (Stone & Norman 1992) scheme, so additional simulations with a code such as PLUTO (Mignone et al. 2007) with a different underlying scheme would be helpful.

The three-planet configuration introduces a much wider configuration space concerning the initial conditions. Which combination of planet masses enables outward

migration in a resonant chain via the Masset–Snellgrove effect? With up to how many planets does the Masset–Snellgrove effect work? Do the planets need to decrease in mass with radius outward for the chain to remain stable?

Repeating the experiment in three dimensions could even further fortify the phenomenon. In three dimensions, especially the phase of fast outward migration is of interest because it is mainly determined by the flow around the planet and the interaction with the vortex. Both the flow of gas around the planet (e.g. Szulágyi et al. 2014; Teague et al. 2019) and vortices (e.g. Lesur & Papaloizou 2009) can show different behavior in three dimensions.

Another open question is where the outward migration stops. This question was already studied previously to some extent (Crida et al. 2009), but only for very high viscosity where the stopping location is determined by the disk's ability to close the gap of the outer, less massive planet. In one of the simulations in paper 2, the outer planet migrated out to a distance of 133 au after 226 kyr. The reached distance can be expected to be a balance between initial disk size, migration rates, and the disk dispersion timescale. All three were not varied in this study, so including a model to properly account for disk size by using a disk with an exponential cutoff at the outside, varying the disk mass to achieve different migration rates, and accounting for disk dispersal (e.g. via an exponentially decreasing mass similar to the models in Bae et al. 2019), would provide a more controlled environment. Learning more about the stopping location of outward migrating chains of planets might reveal more about this possible formation route for directly observed systems such as HR 8799 which is in a 8:4:2:1 configuration (Marois et al. 2010; Goździewski & Migaszewski 2014) where the outer planet is located at around 70 au (Wang et al. 2018).

5.3 Simulating large-scale vortices in PPDs

Previous studies either manually identified vortices, centered the vortex around the coordinate center in sheering sheet simulations (Lesur & Papaloizou 2009; Lin & Pierens 2018; Tarczay-Nehéz et al. 2020; Fung & Ono 2021) or used techniques such as taking extremes or averages of vorticity or surface density in some restricted region in order to describe the vortex (Godon & Livio 1999; Les & Lin 2015; Hammer et al. 2017). To reduce the error introduced by the manual detection of vortices, I developed a novel method based on the elliptical shape of vortensity and surface density iso-value lines and their detection with a computer vision algorithm, which can be expected to work in a wide range of systems and conditions. This allows for the detection of any number of vortices in arbitrary locations in the simulation domain which enables the study of processes like vortex migration. Additionally, the vortices are characterized based on 2D Gaussian fits to the surface density which allows for detailed statistics about size, strength and internal structure. The

process is implemented in the Python tool `vortector` which is freely available to the community.

Paper 2 shows the importance of the thermal relaxation timescale parameterized in the β formalism for the lifetime of vortices that emerge at the edge of a planet-opened gap. This confirms earlier results that found a dependence of vortex lifetime on β in shearing sheet simulations of a vortex forming at the edge of a viscosity transition. They found that vortex lifetime is smaller when increasing β from the locally isothermal regime ($\beta \to 0$) towards β of the order of 1 (Tarczay-Nehéz et al. 2020) and a minimum in vortex lifetime for intermediate values of β (Fung & Ono 2021).

Tarczay-Nehéz et al. (2020) argued that the shorter lifetimes are due to higher temperatures which increase viscosity as $\nu \propto c_s^2 \propto T$, and thus viscous dissipation should be enhanced accordingly. Although temperatures were found to be higher in the models with $\beta = 100$, the increase in the vortex region was usually lower than 10%. Given that viscous dissipation is expected to scale linearly with viscosity (see Eq. (2.20)), this can not be the explanation for the two different regimes found in paper 2 which are separated by at least one order of magnitude.

The remaining term in Eq. (2.20) is the baroclinic term. Fung & Ono (2021) recently proposed an explanation of the variation of the lifetime with β based on a multipole structure of the baroclinic term centered on the vortex and the elliptical motion of gas around the vortex. Contrary to this, the simulations with planets in paper 2 show a dipolar structure of the baroclinic term which is to be expected for a density maximum and a radial temperature gradient.

However, the baroclinic term is significantly impacted by the presence of the planetary spiral arm (see Fig. 10 in paper 2). Vortensity generation at the spiral arm shock (Kevlahan 1997; Lin & Papaloizou 2010; Cimerman & Rafikov 2021) might play an important role. The question of how thermal relaxation, and therefore radiative processes, affect vortex lifetime seems not yet answered and further investigations will be necessary.

The numerical viscosity in the simulations of paper 2 was gauged to be of the order of $\alpha = 10^{-6}$ for 16 cps and in the range $\alpha = 10^{-6}$–10^{-5} for 8 cps. Simulations of vortices at 16 cps should therefore be conducted with $\alpha \geq 10^{-6}$ to have a controlled numerical experiment, otherwise, numerical diffusion can dominate processes such as the dissipation of vortices. Alternatively, the simulations can be performed at higher resolution with the cost of higher runtime (for an example of this strategy, see McNally et al. 2019). The runtime of a smooth disk simulation without turbulence can be expected to scale cubically with linear resolution — one power for the increased number of cells in both directions and one power for the stricter time step criterion because of the shrunken minimum cell size — which sets a practical limit on the resolution that can be used, given that the 16 cps simulations in paper 2 ran for around one month on the University of Tübingen's local HPC cluster with the number of processors chosen for optimal scaling for the given system.

The simulations presented in paper 2 were performed in two dimensions. However, there are important 3D effects such as the elliptical instability (Lesur & Papaloizou 2009) that attack vortices and can lead to faster decay and shorter lifetimes. At the same time, the SBI could sustain the vortices through its vertical modes (Klahr & Bodenheimer 2003; Lesur & Papaloizou 2010) and the VSI might lead to either vortex growth or decay (Flock et al. 2020). It is therefore important to investigate the dependence of vortex properties on β using 3D simulations. To estimate the impact of 3D effects on vortex properties for the models in paper 2, I conducted one 8 cps 3D simulation using `FARGO3D` (Benítez-Llambay & Masset 2016) which took four months to simulate on four NVIDIA K80 GPUs to reach a simulation time of 7000 orbits after which the vortex dissipated. Given that the resolution requirements to observe the long-lived vortex regime was 16 cps, an analogous 3D simulation to reproduce this effect can be expected to take of the order of years (over 5 years with the same number of GPUs by estimating the runtime increase with an additional factor of 2 for all three spatial directions and an additional factor of 2 for the decreased timestep) which practically rules out a parameter study. To solve this problem, the simulation grid in paper 2 can be used to guide the selection of two or three promising models.

5.4 Towards comparing models and observations

The consequences of migration jumps for the substructure of the disk were assessed in paper 1 by simulating the dust continuum emission of the model disks and the observation with ALMA relying on the assumption of constant dust-to-gas ratio and the MRN dust size distribution. The appearance of the disk and the visible substructure was dependent on the phase of the migration jump in which the system was, demonstrating that a single disk can appear with a different substructure depending on the dynamical state of the embedded planetary system. Previous studies with an outward migrating pair of planets and the inclusion of dust dynamics have already shown that effects such as dust trapping and filtration at the outer gap edge are important for the dust distribution Bae et al. (2019); Marzari et al. (2019). Therefore, one important improvement to the models presented in paper 1 and paper 2 is the inclusion of proper dust treatment.

Based on the simulation results, the long-lived regime for $\beta \to 0$ especially, and the expected values of β to decrease radially outward in PPDs (Ziampras et al. 2020), vortices should be expected to be observed primarily in the outer parts of disks. However, there are already observations hinting at vortices in the inner region of disks, e.g. in the inner 0.3 au of the disk of HD 163296 (Varga et al. 2021).

Testing these predictions made by the numerical experiments requires a careful comparison between models and observations for each individual example where one disk is simulated (see, e.g. the models of PDS 70), but also on a statistical

basis where the properties of whole populations need to be studied. This requires the conception of suitable parameter studies and the selection of observed systems to be reproduced.

One prominent example of an individual observed disk is PDS 70, which displays multiple physical effects important for planet formation, e.g. dust size filtration (Bae et al. 2019), and most prominently the existence of two massive embedded planets (Keppler et al. 2018; Müller et al. 2018; Haffert et al. 2019). During my work on this thesis, I used both strategies, reproducing the characteristic properties of type II TDs on one hand and trying to model PDS 70 on the other hand. Both attempts will profit from a proper dust treatment to close the gap between numerical models and observations.

6 Summary

The goal of this thesis was to study the hypothesis that type II transition disks — protoplanetary disks with large inner holes or wide gaps and high mass accretion rates onto the central star — can be explained by an embedded system of planets.

Using two-dimensional fluid dynamics simulations, I was able to show that an outward migrating pair of giant planets can explain large parts of the previously unexplained parameter space in the stellar mass accretion vs. inner hole size domain (see Sec. 4.1).

During this investigation, I discovered and described a novel dynamical phenomenon in the realm of planet–disk interactions called a *migration jump* (see Sec. 4.2). During resonant outward migration of a giant pair of planets, the outer planet can suddenly speed up its migration exponentially and shoot out by several tens of astronomical units in only some thousands of years, before migrating back into resonance with the inner planet. This process is a result of the excitation of eccentricities of the planets, the excitation of a vortex in the outer disk just outside the outer gap edge, and the interaction of the outer planet with the vortex.

In addition to the dynamical analysis, synthetic ALMA observations of the simulated systems were produced in order to predict the observational features of migration jumps (see Sec. 4.3). Due to the similarity between the model systems in which migration jumps were found in the simulations and the real protoplanetary disk and planet system PDS 70, models geared towards this system were analyzed to answer the question of whether migration jumps might happen in PDS 70. This scenario turns out to be unlikely because the surface density in the disk of PDS 70 is lower than that required for a migration jump.

Sparked by the role of the vortex in migration jumps, an investigation into large-scale vortices in protoplanetary disks was performed to identify the role of the timescale of thermal cooling in the disk on the lifetime of vortices (see Sec. 4.4). Two-dimensional fluid dynamics simulations with two different simulation tools were performed for each set of parameters scanning the parameter space of thermal cooling timescale and viscosity. Vortices were strongest and lived longest for low viscosities and low cooling timescales while they lived shortest for cooling timescales comparable to the orbital period, largely consistent with previous studies. For the detection of vortices in fluid dynamics simulations of PPDs, a novel framework called `vortector` was developed. This framework is based on computer vision algorithms and implemented in the Python programming language and made available to the astrophysics community.

Acknowledgments

I feel huge gratitude for the mentoring and supervision of my late supervisor Willy Kley, who sparked my interest in Astrophysics, taught me invaluable lessons and became a dear friend over the last six years.

Big thanks go to my two friends and collaborators Peter Rodenkirch and Alex Ziampras. I enjoyed working, writing and coding together with you.

Another huge thanks goes to the CPT group, for all the wonderful lunch and coffee break discussions, seminars and activities. A special thanks go to my friends and office mates Tobias Moldenhauer and Lucas Jordan, who accompanied me throughout the last years, with whom I discovered and from whom I learned a great number of invaluable lessons. Thank you for all the wonderful discussions and your help. Also a big thanks to Aaron, André, Anna, Barbara, Christoph, Christoph, Daniel, Dennis, Evita, Gabriel, Hugo, Heike, Jibin, Johannes, Jonas, Marius, Max, Michael, Moritz, Oliver, Patrícia, Prakruti, Ricardo, Shrikant, Sareh, Will, and Zahra for all the wonderful time we spend together.

During this PhD, I was part of the DFG research group on transition disks (RUTD). I want to thank all my colleagues and friends in the group for the wonderful meetings and scientific and personal conversations.

I want to thank all my mentors who guided me through many years of school and university, with a special thank you to my high school teacher and Jugendforscht mentor Uwe Klein, who was a constant source of advice and wisdom throughout my later school years and my studies.

Invaluable support to this thesis came from my beloved wife Franziska, my dear family and all my close friends. Thank you for supporting me in life, with my studies and struggles, for celebrating my achievements and for lifting me up and encouraging me when I needed it most.

This work has been funded by the Deutsche Forschungsgemeinschaft (DFG, German Research Foundation) - 325594231. I also acknowledge support by the High Performance and Cloud Computing Group at the Zentrum für Datenverarbeitung of the University of Tübingen, the state of Baden-Württemberg through bwHPC and the German Research Foundation (DFG) through grant no INST 37/935-1 FUGG.

Bibliography

ALMA Partnership, Brogan, C. L., Pérez, L. M., et al. 2015, The Astrophysical Journal, 808, L3, doi:10.1088/2041-8205/808/1/L3

Andrews, S. M. 2020, Annual Review of Astronomy and Astrophysics, 58, 483, doi:10.1146/annurev-astro-031220-010302

Andrews, S. M., Huang, J., Pérez, L. M., et al. 2018, The Astrophysical Journal, 869, L41, doi:10.3847/2041-8213/aaf741

Andrews, S. M. & Williams, J. P. 2005, The Astrophysical Journal, 631, 1134, doi:10.1086/432712

Artymowicz, P. 1993, The Astrophysical Journal, 419, 155, doi:10.1086/173469

Ataiee, S., Pinilla, P., Zsom, A., et al. 2013, Astronomy & Astrophysics, 553, L3, doi:10.1051/0004-6361/201321125

Bae, J., Zhu, Z., Baruteau, C., et al. 2019, The Astrophysical Journal, 884, L41, doi:10.3847/2041-8213/ab46b0

Bae, J., Zhu, Z., & Hartmann, L. 2016, The Astrophysical Journal, 819, 134, doi:10.3847/0004-637X/819/2/134

Balbus, S. A. & Hawley, J. F. 1990, 22, 1209, ADS:1990BAAS...22.1209B

Barge, P. & Sommeria, J. 1995, Astronomy & Astrophysics, 295, L1, ADS:1995A&A...295L...1B

Barraza-Alfaro, M., Flock, M., Marino, S., & Pérez, S. 2021, Astronomy & Astrophysics, 653, A113, doi:10.1051/0004-6361/202140535

Baruteau, C. & Masset, F. 2013, Lecture Notes in Physics, Berlin Springer Verlag, 861, 201, doi:10.1007/978-3-642-32961-6_6

Benítez-Llambay, P. & Masset, F. S. 2016, The Astrophysical Journal Supplement Series, 223, 11, doi:10.3847/0067-0049/223/1/11

Calvet, N., D'Alessio, P., Watson, D. M., et al. 2005, The Astrophysical Journal, 630, L185, doi:10.1086/491652

Chametla, R. O., D'Angelo, G., Reyes-Ruiz, M., & Sánchez-Salcedo, F. J. 2020, Monthly Notices of the Royal Astronomical Society, 492, 6007, doi:10.1093/mnras/staa260

Cimerman, N. P. & Rafikov, R. R. 2021, Monthly Notices of the Royal Astronomical Society, 508, 2329, doi:10.1093/mnras/stab2652

Crida, A., Masset, F., & Morbidelli, A. 2009, The Astrophysical Journal, 705, L148, doi:10.1088/0004-637X/705/2/L148

Crida, A., Morbidelli, A., & Masset, F. 2006, Icarus, 181, 587, doi:10.1016/j.icarus.2005.10.007

D'Angelo, G. & Lubow, S. H. 2008, The Astrophysical Journal, 685, 560, doi:10.1086/590904

Dullemond, C. P., Hollenbach, D., Kamp, I., & D'Alessio, P. 2007, in Protostars and Planets V (University of Arizona Press), 555–572, ADS:2007prpl.conf..555D

Dullemond, C. P., Juhasz, A., Pohl, A., et al. 2012, RADMC-3D: A multi-purpose radiative transfer tool, ADS:2012ascl.soft02015D

Dürmann, C. & Kley, W. 2015, Astronomy & Astrophysics, 574, A52, doi:10.1051/0004-6361/201424837

Dürmann, C. & Kley, W. 2017, Astronomy & Astrophysics, 598, A80, doi:10.1051/0004-6361/201629074

Ercolano, B. & Pascucci, I. 2017, Royal Society Open Science, 4, 170114, doi:10.1098/rsos.170114

Flock, M., Nelson, R. P., Turner, N. J., et al. 2017, The Astrophysical Journal, 850, 131, doi:10.3847/1538-4357/aa943f

Flock, M., Turner, N. J., Nelson, R. P., et al. 2020, The Astrophysical Journal, 897, 155, doi:10.3847/1538-4357/ab9641

Fu, W., Li, H., Lubow, S., & Li, S. 2014, The Astrophysical Journal, 788, L41, doi:10.1088/2041-8205/788/2/L41

Fung, J. & Ono, T. 2021, The Astrophysical Journal, 922, 13, doi:10.3847/1538-4357/ac1d4e

Gaia Collaboration, Brown, A. G. A., Vallenari, A., et al. 2018, Astronomy & Astrophysics, 616, A1, doi:10.1051/0004-6361/201833051

Gammie, C. F. 2001, The Astrophysical Journal, 553, 174, doi:10.1086/320631

Garufi, A., Quanz, S. P., Avenhaus, H., et al. 2013, Astronomy & Astrophysics, 560, A105, doi:10.1051/0004-6361/201322429

Godon, P. & Livio, M. 1999, The Astrophysical Journal, 523, 350, doi:10.1086/307720

Goldreich, P. & Tremaine, S. 1979, The Astrophysical Journal, 233, 857, doi:10.1086/157448

Goldreich, P. & Tremaine, S. 1980, The Astrophysical Journal, 241, 425, doi:10.1086/158356

Goodman, J., Narayan, R., & Goldreich, P. 1987, Monthly Notices of the Royal Astronomical Society, 225, 695, doi:10.1093/mnras/225.3.695

Goździewski, K. & Migaszewski, C. 2014, Monthly Notices of the Royal Astronomical Society, 440, 3140, doi:10.1093/mnras/stu455

Greene, T. 2001, American Scientist, 89, 316, doi:10.1511/2001.28.738

Haffert, S. Y., Bohn, A. J., de Boer, J., et al. 2019, Nature Astronomy, doi:10.1038/s41550-019-0780-5

Haisch, Jr., K. E., Lada, E. A., & Lada, C. J. 2001, The Astrophysical Journal, 553, L153, doi:10.1086/320685

Hammer, M., Kratter, K. M., & Lin, M.-K. 2017, Monthly Notices of the Royal Astronomical Society, 466, 3533, doi:10.1093/mnras/stw3000

Hammer, M., Pinilla, P., Kratter, K. M., & Lin, M.-K. 2019, Monthly Notices of the Royal Astronomical Society, 482, 3609, doi:10.1093/mnras/sty2946

Hartmann, L., Calvet, N., Gullbring, E., & D'Alessio, P. 1998, The Astrophysical Journal, 495, 385, doi:10.1086/305277

Hawley, J. F., Gammie, C. F., & Balbus, S. A. 1995, The Astrophysical Journal, 440, 742, doi:10.1086/175311

Hubeny, I. 1990, The Astrophysical Journal, 351, 632, doi:10.1086/168501

Ikoma, M., Nakazawa, K., & Emori, H. 2000, The Astrophysical Journal, 537, 1013, doi:10.1086/309050

Johansen, A., Andersen, A. C., & Brandenburg, A. 2004, Astronomy & Astrophysics, 417, 361, doi:10.1051/0004-6361:20034417

Kanagawa, K. D., Tanaka, H., Muto, T., & Tanigawa, T. 2017, Publications of the Astronomical Society of Japan, 69, doi:10.1093/pasj/psx114

Kanagawa, K. D., Tanaka, H., Muto, T., Tanigawa, T., & Takeuchi, T. 2015, Monthly Notices of the Royal Astronomical Society, 448, 994, doi:10.1093/mnras/stv025

Kenyon, S. J. & Hartmann, L. 1995, The Astrophysical Journal Supplement Series, 101, 117, doi:10.1086/192235

Keppler, M., Benisty, M., Müller, A., et al. 2018, Astronomy & Astrophysics, 617, A44, doi:10.1051/0004-6361/201832957

Keppler, M., Teague, R., Bae, J., et al. 2019, Astronomy & Astrophysics, 625, A118, doi:10.1051/0004-6361/201935034

Kevlahan, N. K.-R. 1997, Journal of Fluid Mechanics, 341, 371, doi:10.1017/S0022112097005752

Kida, S. 1981, Journal of the Physical Society of Japan, 50, 3517, doi:10.1143/JPSJ.50.3517

Klahr, H. H. & Bodenheimer, P. 2003, The Astrophysical Journal, 582, 869, doi:10.1086/344743

Kley, W. 1999, Monthly Notices of the Royal Astronomical Society, 303, 696, doi:10.1046/j.1365-8711.1999.02198.x

Kley, W. & Nelson, R. 2012, Annual Review of Astronomy and Astrophysics, 50, 211, doi:10.1146/annurev-astro-081811-125523

Les, R. & Lin, M.-K. 2015, Monthly Notices of the Royal Astronomical Society, 450, 1503, doi:10.1093/mnras/stv712

Lesur, G. & Papaloizou, J. C. B. 2009, Astronomy & Astrophysics, 498, 1, doi:10.1051/0004-6361/200811577

Lesur, G. & Papaloizou, J. C. B. 2010, Astronomy & Astrophysics, 513, A60, doi:10.1051/0004-6361/200913594

Li, H., Li, S., Koller, J., et al. 2005, The Astrophysical Journal, 624, 1003, publisher: IOP Publishing, doi:10.1086/429367

Lin, D. N. C. & Papaloizou, J. 1979, Monthly Notices of the Royal Astronomical Society, 186, 799, doi:10.1093/mnras/186.4.799

Lin, M.-K. & Papaloizou, J. C. B. 2010, Monthly Notices of the Royal Astronomical Society, doi:10.1111/j.1365-2966.2010.16560.x

Lin, M.-K. & Pierens, A. 2018, Monthly Notices of the Royal Astronomical Society, 478, 575, doi:10.1093/mnras/sty947

Lodato, G. 2008, New Astronomy Reviews, 52, 21, doi:10.1016/j.newar.2008.04.002

Lovelace, R. V. E. & Hohlfeld, R. G. 2013, Monthly Notices of the Royal Astronomical Society, 429, 529, doi:10.1093/mnras/sts361

Lovelace, R. V. E., Li, H., Colgate, S. A., & Nelson, A. F. 1999, The Astrophysical Journal, 513, 805, doi:10.1086/306900

Lynden-Bell, D. & Pringle, J. E. 1974, Monthly Notices of the Royal Astronomical Society, 168, 603, doi:10.1093/mnras/168.3.603

Lyra, W. & Umurhan, O. M. 2019, Publications of the Astronomical Society of the Pacific, 131, 072001, doi:10.1088/1538-3873/aaf5ff

Marcus, P. S., Pei, S., Jiang, C.-H., & Barranco, J. A. 2016, The Astrophysical Journal, 833, 148, doi:10.3847/1538-4357/833/2/148

Marcus, P. S., Pei, S., Jiang, C.-H., et al. 2015, The Astrophysical Journal, 808, 87, doi:10.1088/0004-637X/808/1/87

Marel, N. v. d., Dishoeck, E. F. v., Bruderer, S., et al. 2013, Science, 340, 1199, doi:10.1126/science.1236770

Marois, C., Zuckerman, B., Konopacky, Q. M., Macintosh, B., & Barman, T. 2010, Nature, 468, 1080, doi:10.1038/nature09684

Marzari, F., D'Angelo, G., & Picogna, G. 2019, The Astronomical Journal, 157, 45, doi:10.3847/1538-3881/aaf3b6

Masset, F. 2000, Astronomy and Astrophysics Supplement Series, 141, 165, doi:10.1051/aas:2000116

Masset, F. & Snellgrove, M. 2001, Monthly Notices of the Royal Astronomical Society, 320, L55, doi:10.1046/j.1365-8711.2001.04159.x

Masset, F. S. & Papaloizou, J. C. B. 2003, The Astrophysical Journal, 588, 494, doi:10.1086/373892

Mathis, J. S., Rumpl, W., & Nordsieck, K. H. 1977, The Astrophysical Journal, 217, 425, doi:10.1086/155591

McMullin, J. P., Waters, B., Schiebel, D., Young, W., & Golap, K. 2007, in Astronomical Society of the Pacific Conference Series, Vol. 376, Astronomical Data Analysis Software and Systems XVI, ed. R. A. Shaw, F. Hill, & D. J. Bell, 127, ADS:2007ASPC..376..127M

McNally, C. P., Nelson, R. P., Paardekooper, S.-J., & Benítez-Llambay, P. 2019, Monthly Notices of the Royal Astronomical Society, 484, 728, doi:10.1093/mnras/stz023

Mignone, A., Bodo, G., Massaglia, S., et al. 2007, The Astrophysical Journal Supplement Series, 170, 228, doi:10.1086/513316

Miranda, R. & Rafikov, R. R. 2020, The Astrophysical Journal, 904, 121, doi:10.3847/1538-4357/abbee7

Mizuno, H. 1980, Progress of Theoretical Physics, 64, 544, doi:10.1143/PTP.64.544

Murray, C. D. & Dermott, S. F. 2000, Solar System Dynamics (Cambridge University Press), doi:10.1017/CBO9781139174817

Müller, A., Keppler, M., Henning, T., et al. 2018, Astronomy & Astrophysics, 617, L2, doi:10.1051/0004-6361/201833584

Müller, T. W. A. & Kley, W. 2012, Astronomy & Astrophysics, 539, A18, doi:10.1051/0004-6361/201118202

Nelson, R. P., Gressel, O., & Umurhan, O. M. 2013, Monthly Notices of the Royal Astronomical Society, 435, 2610, doi:10.1093/mnras/stt1475

Nesvorný, D. 2018, Annual Review of Astronomy and Astrophysics, vol. 56, p.137-174, 56, 137, doi:10.1146/annurev-astro-081817-052028

Offner, S. S. R., Moe, M., Kratter, K. M., et al. 2022, The Origin and Evolution of Multiple Star Systems, ADS:2022arXiv220310066O

Ogilvie, G. I. & Lubow, S. H. 2002, Monthly Notices of the Royal Astronomical Society, 330, 950, doi:10.1046/j.1365-8711.2002.05148.x

Owen, J. E. 2016, Publications of the Astronomical Society of Australia, 33, e005, doi:10.1017/pasa.2016.2

Paardekooper, S.-J., Dong, R., Duffell, P., et al. 2022, Planet-Disk Interactions, ADS:2022arXiv220309595P

Paardekooper, S.-J., Lesur, G., & Papaloizou, J. C. B. 2010, The Astrophysical Journal, 725, 146, doi:10.1088/0004-637X/725/1/146

Pepliński, A., Artymowicz, P., & Mellema, G. 2008, Monthly Notices of the Royal Astronomical Society, 387, 1063, doi:10.1111/j.1365-2966.2008.13339.x

Picogna, G., Ercolano, B., Owen, J. E., & Weber, M. L. 2019, Monthly Notices of the Royal Astronomical Society, 487, 691, doi:10.1093/mnras/stz1166

Pierens, A. & Lin, M.-K. 2018, Monthly Notices of the Royal Astronomical Society, 479, 4878, doi:10.1093/mnras/sty1314

Pérez, L. M., Benisty, M., Andrews, S. M., et al. 2018, The Astrophysical Journal, 869, L50, doi:10.3847/2041-8213/aaf745

Pérez, L. M., Isella, A., Carpenter, J. M., & Chandler, C. J. 2014, The Astrophysical Journal, 783, L13, doi:10.1088/2041-8205/783/1/L13

Quillen, A. C., Blackman, E. G., Frank, A., & Varnière, P. 2004, The Astrophysical Journal, 612, L137, doi:10.1086/424693

Rafikov, R. R. 2002, The Astrophysical Journal, 569, 997, doi:10.1086/339399

Regály, Z. & Vorobyov, E. 2017, Monthly Notices of the Royal Astronomical Society, 471, 2204, doi:10.1093/mnras/stx1801

Rice, W. K. M., Wood, K., Armitage, P. J., Whitney, B. A., & Bjorkman, J. E. 2003, Monthly Notices of the Royal Astronomical Society, 342, 79, doi:10.1046/j.1365-8711.2003.06515.x

Rodenkirch, P. J., Rometsch, T., Dullemond, C. P., Weber, P., & Kley, W. 2021, Astronomy & Astrophysics, 647, A174, doi:10.1051/0004-6361/202038484

Rometsch, T., Rodenkirch, P. J., Kley, W., & Dullemond, C. P. 2020, Astronomy & Astrophysics, 643, A87, doi:10.1051/0004-6361/202038311

Rometsch, T., Ziampras, A., Kley, W., & Béthune, W. 2021, Astronomy & Astrophysics, 656, A130, doi:10.1051/0004-6361/202142105

Shakura, N. I. & Sunyaev, R. A. 1973, Astronomy & Astrophysics, 500, 33, ADS:1973A&A....24..337S

Shu, F. H. 1992, The physics of astrophysics. Volume II: Gas dynamics. (University Science Books), ADS:1992pavi.book.....S

Stoll, M. H. R. & Kley, W. 2014, Astronomy & Astrophysics, 572, A77, doi:10.1051/0004-6361/201424114

Stone, J. M. & Norman, M. L. 1992, The Astrophysical Journal Supplement Series, 80, 753, doi:10.1086/191680

Szulágyi, J., Morbidelli, A., Crida, A., & Masset, F. 2014, The Astrophysical Journal, 782, 65, doi:10.1088/0004-637X/782/2/65

Tanga, P., Babiano, A., Dubrulle, B., & Provenzale, A. 1996, Icarus, 121, 158, doi:10.1006/icar.1996.0076

Tarczay-Nehéz, D., Regály, Z., & Vorobyov, E. 2020, Monthly Notices of the Royal Astronomical Society, 493, 3014, doi:10.1093/mnras/staa364

Teague, R., Bae, J., & Bergin, E. A. 2019, Nature, 574, 378, doi:10.1038/s41586-019-1642-0

Val-Borro, M. d., Artymowicz, P., D'Angelo, G., & Peplinski, A. 2007, Astronomy & Astrophysics, 471, 1043, doi:10.1051/0004-6361:20077169

Varga, J., Hogerheijde, M., van Boekel, R., et al. 2021, Astronomy & Astrophysics, 647, A56, doi:10.1051/0004-6361/202039400

Wang, J. J., Graham, J. R., Dawson, R., et al. 2018, The Astronomical Journal, 156, 192, doi:10.3847/1538-3881/aae150

Ward, W. R. 1997, Icarus, 126, 261, doi:10.1006/icar.1996.5647

Weidenschilling, S. J. 1977, Monthly Notices of the Royal Astronomical Society, 180, 57, doi:10.1093/mnras/180.2.57

Williams, J. P. & Cieza, L. A. 2011, Annual Review of Astronomy and Astrophysics, 49, 67, _eprint: 1103.0556, doi:10.1146/annurev-astro-081710-102548

Zhu, Z. & Baruteau, C. 2016, Monthly Notices of the Royal Astronomical Society, 458, 3918, doi:10.1093/mnras/stw202

Ziampras, A., Ataiee, S., Kley, W., Dullemond, C. P., & Baruteau, C. 2020, Astronomy & Astrophysics, 633, A29, doi:10.1051/0004-6361/201936495

A&A 643, A87 (2020)
https://doi.org/10.1051/0004-6361/202038311
© ESO 2020

Astronomy & Astrophysics

Migration jumps of planets in transition discs

Thomas Rometsch[1], Peter J. Rodenkirch[2], Wilhelm Kley[1], and Cornelis P. Dullemond[2]

[1] Institut für Astronomie und Astrophysik, Universität Tübingen, Auf der Morgenstelle 10, 72076 Tübingen, Germany
e-mail: thomas.rometsch@uni-tuebingen.de
[2] Institute for Theoretical Astrophysics, Zentrum für Astronomie, Heidelberg University, Albert Ueberle Str. 2, 69120 Heidelberg, Germany

Received 29 April 2020 / Accepted 5 September 2020

ABSTRACT

Context. Transition discs form a special class of protoplanetary discs that are characterised by a deficiency of disc material close to the star. In a subgroup, inner holes in these discs can stretch out to a few tens of au while there is still mass accretion onto the central star observed at the same time.
Aims. We analyse the proposition that this type of wide transition disc is generated by the interaction of the disc with a system of embedded planets.
Methods. We performed two-dimensional hydrodynamics simulations of a flat disc. Different equations of state were used including locally isothermal models and more realistic cases that consider viscous heating, radiative cooling, and stellar heating. Two massive planets (with masses of between three and nine Jupiter masses) were embedded in the disc and their dynamical evolution due to disc–planet interaction was followed for over 100 000 yr. The simulations account for mass accretion onto the star and planets. We included models with parameters reminiscent of the system PDS 70. To assess the observability of features in our models we performed synthetic ALMA observations.
Results. For systems with a more massive inner planet, there are phases where both planets migrate outward engaged in a 2:1 mean motion resonance via the Masset-Snellgrove mechanism. In sufficiently massive discs, the resulting formation of a vortex and the interaction with it can trigger rapid outward migration of the outer planet where its distance can increase by tens of au in a few thousand years. After another few thousand years, the outer planet rapidly migrates back inwards into resonance with the inner planet. We call this emerging composite phenomenon a migration jump. Outward migration and the migration jumps are accompanied by a high mass accretion rate onto the star. The synthetic images reveal numerous substructures depending on the type of dynamical behaviour.
Conclusions. Our results suggest that the outward migration of two embedded planets is a prime candidate for the explanation of the observed high stellar mass accretion rate in wide transition discs. The models for PDS 70 indicate it is not currently undergoing a migration jump but might very well be in a phase of outward migration.

Key words. accretion, accretion disks – protoplanetary disks – planet–disk interactions – hydrodynamics – methods: numerical

1. Introduction

Observationally, transition discs are characterised by a lack of flux in the micrometre (near- to mid-infrared) range as seen in the spectral energy distributions (SEDs) of young stars. This flux deficit is typically associated with "missing" dust and with temperatures of 200–1000 K (Calvet et al. 2002; D'Alessio et al. 2005) corresponding to the inner regions of accretion discs. Despite this lack of dust, there are still signatures of gas accretion in several systems with large inner (dust) holes that are a few tens of astronomical units (au) in width (see e.g. Espaillat et al. 2014).

The observational properties of transitional discs (TDs) and previous modelling attempts have been reviewed by Owen (2016) and here we mention only the main aspects relevant to this paper. The origin of the inner disc clearing is primarily attributed to three different processes: photoevaporation from the inside out through high-energy radiation from the central young protostar (e.g. Shu et al. 1993; Alexander et al. 2006), magnetically driven disc winds (e.g. Rodenkirch et al. 2020), or embedded massive companions that carve deep gaps into the disc (e.g. Varnière et al. 2006). Additionally, TDs appear to come in two flavours, millimetre(mm)-faint discs with low mm fluxes, small inner holes ($\lesssim$10au), and low accretion rates onto the stars ($\approx 10^{-10}$–$10^{-9}\ M_\odot\,\mathrm{yr}^{-1}$), and mm-bright discs with large mm fluxes, large holes ($\gtrsim$20 au), and high accretion rates $\approx 10^{-8}\ M_\odot\,\mathrm{yr}^{-1}$ (Owen & Clarke 2012) to which we refer here as Type I and Type II discs, respectively.

While photoevaporation is certainly at work in some systems (Type I TDs), it is believed that it can only operate for systems with a sufficiently low mass accretion rate below $10^{-8} M_\odot\,\mathrm{yr}^{-1}$ and is otherwise quenched by the accretion flow (Owen & Clarke 2012). At the same time the persistence of gas accretion within the inner (dust) holes is taken as an additional indication that other mechanisms should operate that create these gaps (Manara et al. 2014). The very likely mechanism for this second class of TDs is related to the growth of planets in the discs, because young planets embedded in their nascent discs will not only open a gap in the gas disc but will create an even stronger depletion of the dust near the planetary orbit (Paardekooper & Mellema 2004).

Consequently, it was suggested early on that the presence of a massive (Jupiter-sized) planet might be responsible for the gap creation (Varnière et al. 2006; Rice et al. 2006), but at the same time it has been reported that the gap created by a single embedded planet is significantly narrower than suggested by

observations of transition discs. Given the problems with a single planet and the photoevaporation models, it has been proposed that the main observational features can be created by the presence of a system of (three to four) massive planets. Following this line of thought, Zhu et al. (2011) and Dodson-Robinson & Salyk (2011) performed numerical simulations and argue that TDs are in fact signposts of young multi-planet systems. In this scenario, the embedded planets act as a "barrier" for the gas flow through the disc, allowing some gas to enter the inner region, causing the observed accretional features near the star, while the dust is filtered out at the pressure maximum just beyond the outer edge of the gap and cannot enter the inner disc regions. Following this line of thought, theoretical models with embedded planets and dust in discs have been constructed to match the observed spectral energy distributions at sub-millimetre wavelengths (de Juan Ovelar et al. 2013; Pinilla et al. 2015).

New ALMA observations focusing on CO-rotational lines have allowed the gas content to be determined in the inner disc region in more detail. These results show that the inner disc gas depleted by factors of about 10^2 (van der Marel et al. 2015), or even by a factor of 10^4 with gas holes about a factor 2–3 smaller than the dust gaps (van der Marel et al. 2016), which is taken as another example of massive planets in discs (Ho 2016). The conclusion that all or the majority of Type II TDs are shaped by massive planets was questioned by Dong & Dawson (2016) who argue that there may not be enough giant planets to explain all the observed Type II TDs; see also Cumming et al. (2008) for the occurrence rate of massive planets at larger separations. The solution to this problem is either that current numerical models of planet–disc interactions are too inefficient at gap opening compared to what is seen in nature, or that Type II TDs are intrinsically rare objects rather than being common and short-lived as is probably the case for their Type I counterparts. Considering that the arguments of Dong & Dawson (2016) are based on analytical approximations of gap widths and sizes that are based on isothermal disc models, it may well be that the theoretical models have not reached the degree of sophistication necessary to produce reliable results.

Recent evidence in favour of the planet-based origin of Type II TDs came through the direct detection of embedded planets in such systems. For the T Cha system, the presence of a planet was suggested based on observations in the *L*-band (Huélamo et al. 2011) which were later supported by ALMA observations indicating a gap in the disc ranging from 18 and 28 au compatible with a $1.2\,M_{\rm Jup}$ planet (Hendler et al. 2018). However, direct confirmation is still pending. A point-like source was detected in the *L*-band in the transition disc system MWC 758 at a deprojected distance of about 20 au from the star (Reggiani et al. 2018), directly hinting at the presence of an embedded planet. However, the clearest evidence comes from the PDS 70 system. A first point like object was detected in the near-infrared at a projected distance of 22 au, which was attributed to a planet (PDS 70b) orbiting within a gap that stretches from about 17–54 au in size (Keppler et al. 2018). The large gap size in PDS 70 suggested a second companion which was detected last year (Haffert et al. 2019). The authors confirmed the earlier Hα detection of PDS 70b and found a second point-like Hα source near the outer edge of the gap. This Hα emission is taken as evidence for ongoing accretion onto two proto-planets (Haffert et al. 2019). In addition, the spatial separation of the two planets indicates that they are close to a 2:1 mean motion resonance (MMR).

With respect to PDS 70, a few simulations of embedded planets have been performed. The first study (Muley et al. 2019) considered only one planet and a possible explanation of the wide gap was the creation of a large eccentric cavity by a massive planet of about $2.5\,M_{\rm Jup}$. While this is in principle a possible scenario for sculpting transition discs, as shown also by Müller & Kley (2013), the direct observation of a second planet ruled out this scenario for PDS 70. Consequently, two-planet simulations were presented that show that a system engaged in a 2:1 MMR can in fact be stable for several million years (Bae et al. 2019).

In this paper we study the evolution of planets embedded in protoplanetary discs using two-dimensional hydrodynamical simulations. Our simulations include planet migration and mass accretion and either assume a locally isothermal equation of state or incorporate stellar heating and radiative cooling from the disc. This work extends an earlier study (Müller & Kley 2013) where only one planet was considered, which remained on a fixed orbit around the star and was not allowed to migrate through the disc. First, we present generic models to demonstrate our new findings on the occurrence of migration jumps. We then present our study of the system PDS 70. For both cases, we generate synthetic images and discuss the observability of the features.

In Sect. 2, we introduce our numerical model. In Sect. 3, we present the evolution of the planetary system in our numerical simulations and describe migration jumps in detail. In Sect. 4, we generate synthetic images of a disc in our simulations and identify possible observational features. Section 5 is a case study of how migration jumps apply to the PDS 70 system. We discuss our findings in Sect. 6 and give a summary in Sect. 7.

2. Modelling

In this section we describe the physical and numerical setup used in our simulations. To give an overview of the cases investigated, Table 1 lists all models and summarises their most important parameters. Specific models are referred to using a sans serif font.

2.1. Physical setup

We model an accretion disc around a young protostar solving the two-dimensional (2D, r–ϕ) viscous hydrodynamical equations obtained by averaging over the vertical direction. Most of our models assume a locally isothermal equation of state ($T = T(r)$ is constant over time). For selected models (IRR, PDS70 IRR, PDS70 IRR M/5) we solve the energy equation and include heating by irradiation from the star (analogous to Ziampras et al. 2020), viscous heating, and radiative cooling, using an averaged opacity. All the details of the used set of equations are stated in Müller & Kley (2012, 2013). Here, we do not solve for radiative transport within the plane of the disc.

For the systems investigated here, the locally isothermal assumption and the inclusion of the radiative effects yield comparable results as the test in Appendix B shows.

Viscosity is parameterised with the α viscosity model (Shakura & Sunyaev 1973) using a value $\alpha = 10^{-3}$. The kinematic viscosity is then $\nu = \alpha c_{\rm s} H$ with the sound speed $c_{\rm s}$ and the vertical pressure scale height of the disc H. Together with the choices for Σ and H/r (as given below) this value of α corresponds to a viscous mass accretion rate $\dot{M}_{\rm disc} = 3\pi\Sigma\nu = 5.3 \times 10^{-9}\,M_\odot\,{\rm yr}^{-1}$ at 2 au for the initial profile (see also panel 2 of Fig. 1).

The host star mass is $M_* = 1\,M_\odot$. There are two planets embedded in the disc. The inner planet (1) is initially located at $a_1 = 4\,a_{\rm Jup} = 20.8$ au with a mass of $M_1 = 3$–$9\,M_{\rm Jup}$ and the outer planet (2) is initially located at $a_2 = 7\,a_{\rm Jup} = 36.4$ au with a mass of $M_2 = 1$–$9\,M_{\rm Jup}$. These models are labelled with Mk-l where k/l

Table 1. Model parameters and outcome of the simulations.

Label	Bound [a]	Res [b]	M_1 [c]	M_2 [c]	f_{acc}	Σ [d]	Migration [e]	Jump [f]	Events [g]	Fig.
M9-3, A0.0	O		9	3			↗	✓		[h]
M6-2	O		6	2			↗	✓		
M3-1	O		3	1			↗	✓		
M9-4.5	O		9	4.5			↗	✓	DS	3
M6-3	O		6	3			↗	✓		
M6-6	O		6	6			↘			3
M3-9	O		3	9			↘			3
M2-6	O		2	6			↘			
M3-1.5	O		3	1.5			↘			
M9-3 HR	O	1/2	9	3			↗	✓		A.1
M9-3 DR	O	2	9	3			↗	✓		A.1
M9-3 M/10	O		9	3		1/10	↗			
IRR	O		9	3			↗	✓		B.1, B.2
FLARE	O		9	3			↗	✓		B.1, B.2
A0.0001	O		9	3	10^{-4}		↗	✓		7, 8
A0.001	O		9	3	10^{-3}		↗	✓		7, 8
A0.01	O		9	3	10^{-2}		↗	✓	DS	7, 8
A0.1	O		9	3	10^{-1}		↗	✓		7, 8
L	O	1/2	9	3			↗ ↘	✓	S	9
L M/2	O	1/2	9	3		1/2	↗	✓		
L M/10	O	1/2	9	3		1/10	↗			
VB	V		9	3			↗	✓	E	
VB5	V5		9	3			↗	✓	E	
WD	O+WD	1/2	9	3			↗	✓	E	
WDR	R+WD	1/2	9	3			↗	✓	E	
VB-P	V		9	3			↗	✓		
VB5-P	V5		9	3			↗	✓		
WD-P	O+WD	1/2	9	3			↗	✓		
WDR-P	R+WD	1/2	9	3			↗	✓		
SG	V5		9	3			↗ ↘	✓	S	
SG IRR	V5		9	3			↗ ↘	✓	DS, S	
PDS70 ISO	O		9	3			↗	✓		11
PDS70 IRR	O		9	3			↗	✓		11
PDS70 IRR M/5	O		9	3		1/5	↗			11

Notes. If a field is empty in the Res, f_{acc}, or Σ column, the values are the same as for the reference model M9-3. [a]For the inner boundary, the following choices are possible: O means an outflow boundary, R a closed reflective boundary, V a viscous boundary, V5 a viscous boundary with five times viscous speed, and +WD indicates an additional wave damping zone close to the inner boundary, see Sect. 2.4 for more detail. [b]The factor refers to the 2D resolution compared to the M9-3 case (Sect. 2.2). [c]Planet masses in units of M_{Jup}. [d]Surface density in units of the reference density Σ_0 (see Eq. (1)). [e]Direction of migration where ↗ and ↘ indicate outward and inward migration, respectively. [f]✓, if at least one migration jump happened in the simulation. [g]Additional events of interest, where S indicates a single orbit swap, DS a double orbit swap, and E stands for planet ejection. [h]The standard model M9-3 is used in Figs. 3, 4, 5, 6, 8, A.1, B.1, B.2, 6 and C.1.

is the mass of the inner/outer planet in M_{Jup}, respectively. The exact combinations of masses can be found in Table 1. For all combinations of planet masses, a large deep gap can be expected in the disc.

To simplify the simulations, self-gravity of the disc is neglected in most of them. For the initial conditions of our standard model M9-3 the Toomre Q parameter is above 3 at 100 au and above 8 close to the location of the planet. Thus, self-gravity should not play a dominant role in the system considered. This assumption is verified by two additional models with self-gravity included. The corresponding models are described in Sect. 2.8.

2.2. Simulation code

The hydrodynamics equations are solved on a 2D polar grid (using r–ϕ coordinates). Radially, the domain ranges from 2.08–208 au covered by 602 cells that are logarithmically spaced. Azimuthally, the grid is uniformly spaced from 0 to 2π with 821 cells.

We use a custom version of the FARGO code (Masset 2000), which was also used by Müller & Kley (2013) in an earlier version, and is further developed and maintained by our group at the University of Tübingen. N-body calculations are performed with

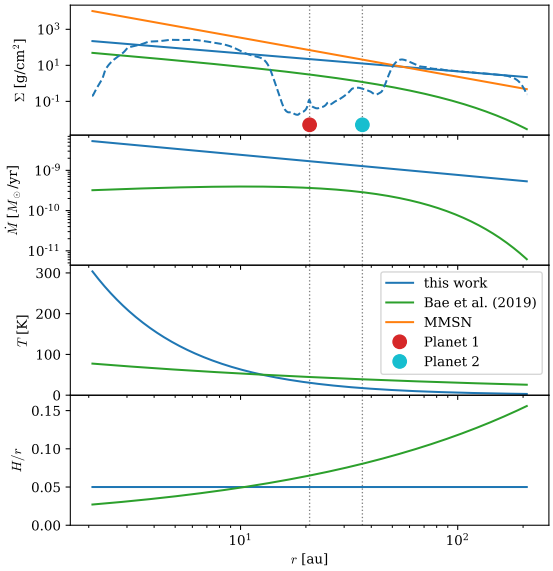

Fig. 1. Initial conditions for the disc around the $1\,M_\odot$ star used in our simulations (blue). These are compared to the initial conditions of the disc in Bae et al. (2019) (green) in which the PDS70 system ($0.85\,M_\odot$ star) was modelled. For context, the surface density of the minimum mass solar nebula (MMSN; Hayashi 1981) is plotted in orange. Physical initial conditions after the equilibration phase (see Fig. 2) at $t = 26$ kyr are shown for model M9-3 as a dashed blue line. The panels, *from top to bottom*, show the radial profile of the: surface density, viscous mass accretion rate ($\dot{M}_{\rm disc} = 3\pi\Sigma\nu$ with $\alpha = 10^{-3}$), temperature, and aspect ratio. The initial location of the planets are marked by the vertical, dotted lines which span over all panels and are indicated by the red and cyan circles.

the IAS15 integrator in REBOUND (Rein & Liu 2012) which is integrated into our version of FARGO.

2.3. Initial conditions

Initially, the surface density of the disc Σ is set to a power-law profile of the form

$$\Sigma(r) = \Sigma_0 \left(\frac{r}{\rm au}\right)^{-1}, \quad \Sigma_0 = 461.76\,\frac{\rm g}{\rm cm^2}. \tag{1}$$

The aspect ratio of the disc is chosen as $h = \frac{H}{r} = 0.05$ throughout the disc, which is equivalent to choosing a temperature power law of

$$T(r) = T_0 \left(\frac{r}{\rm au}\right)^{-1}, \quad T_0 = 632.86\,{\rm K}. \tag{2}$$

We checked this assumption by performing additional simulations using irradiated discs; see Appendix B.

Both initial conditions are visualised in Fig. 1. The top panel shows $\Sigma(r)$. The second panel from the top shows the viscous mass accretion rate, $\dot{M}_{\rm disc} = 3\pi\Sigma\nu$, at each radius in the disc assuming $\alpha = 10^{-3}$. The panel below that, and the bottom panel, show $T(r)$ and the resulting disc aspect ratio, H/r, respectively. To establish a context, we also show the initial conditions of a PDS 70 simulation by Bae et al. (2019, hereafter B19) and the minimum mass solar nebula (MMSN; Hayashi 1981). Our disc has a lower Σ than the MMSN in the inner $\approx$60 au and is about five times larger than the Σ in B19, who model the 5.4 Myr old

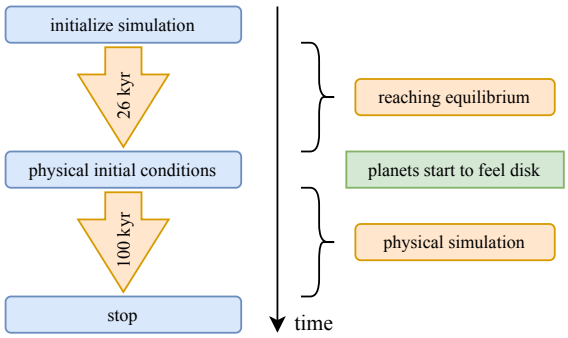

Fig. 2. Flow chart illustrating the equilibration and simulation phase. The disc properties are initialised according to the power laws in Eqs. (1) and (2). During the equilibration process (taking 26 kyr, equivalent to 274 orbits at the initial location of the inner planet) where the disc begins to "feel" the planets, the density profile changes significantly; see the first panel of Fig. 1 for the difference, where the equilibrated profile is shown as the dashed blue line.

PDS 70 system with a $0.85\,M_\odot$ star. Their disc is lighter, as might be expected for an older system due to disc dispersal, and has lower temperatures in the inner parts of the disc due to lower stellar luminosity. The first panel also displays $\Sigma(r)$ after the initial equilibration phase as the dashed blue line. The locations of the planets are marked by the dotted vertical lines and the red and cyan circles in the top panel.

These power-law initial conditions do not take into account the presence of embedded planets. To obtain more physical initial conditions which are consistent with two massive embedded planets, we insert the planets by ramping up their masses over 0.5 kyr while they are fixed at their orbits for an initial equilibration time, $T_{\rm eq}$. During this time, the N-body system evolves without being subjected to the gravitational force of the disc while the disc is exposed to the forces of the N-body system and a common gap forms around the planets. To determine $T_{\rm eq}$, we analysed test simulations and checked for the time when the density waves caused by the insertion of the planets left the computational domain and the time after which the gap depth no longer changed significantly. The second condition is fulfilled at a later time and yields $T_{\rm eq} = 26$ kyr which corresponds to 274 orbits at the initial location of the inner planet. After this time, the disc feedback onto star and planets is turned on which causes them to migrate. The equilibration process is sketched by the flow chart in Fig. 2.

2.4. Boundary conditions

We employ an outflow boundary (O) condition at both radial boundaries, $R_{\rm min}$ and $R_{\rm max}$. This is done to let the disc evolve on its own, for example by allowing for an eccentric disc close to the inner boundary which might be unphysically suppressed by the use of a wave damping boundary, for example, that imposes an azimuthal symmetry close to the boundary. Additionally, this choice of boundary condition allows density waves that are created by the insertion of the planets to leave the computational domain.

For our outflow boundary condition, only mass flow leaving the domain is allowed. This is implemented by enforcing a vanishing gradient of the energy density and Σ, and by setting the radial velocity to zero at the boundary in cases where the velocity vector points into the domain and by setting its gradient to zero

otherwise. This way, no mass can be generated. The azimuthal velocity is left unchanged.

In order to check the validity of these boundary conditions for our physical setup, we studied other options. This is important because the open boundary condition leads to an unphysical drop in surface density close to the boundary, as can be seen in the top panel of Fig. 1.

One alternative is to employ an additional wave damping (WD) zone (de Val-Borro et al. 2006) between $R_{\rm min}$ and $2\,R_{\rm min}$ where Σ and the velocities are exponentially damped to their initial values on a timescale of 5% of the orbital timescale at $R_{\rm min}$ (models WD at half resolution). We combine this wave damping zone with the outflow boundary and with another common choice: a closed, reflective boundary. This reflective boundary does not allow mass flow through the boundary which is implemented by applying a zero gradient for energy density and Σ, and by setting the radial velocities of the ghost cells to zero at the boundary and to the negative of the first active cell's radial velocity at the next ghost cell interface, thus reflecting momentum at the boundary. A combination of a reflective boundary and a wave damping zone is used in model WDR.

An outflow boundary as used in our simulations might overestimate the mass flow across the inner domain. In a real system, the properties of the accretion process onto the star are likely to limit the mass flow at the inner disc edge. To test for the implication of this, we also employed a viscous internal boundary. For this, the velocities of the inner ghost cells are set to a multiple of the viscous speed:

$$v(r_{\rm in}) = \beta\, v_{\rm visc}(r_{\rm in}), \qquad v_{\rm visc}(r_{\rm in}) = -\frac{3\nu}{2r_{\rm in}}, \tag{3}$$

with ν being kinematic viscosity. We used $\beta = 1$ (model VB) and $\beta = 5$ (model VB5) which was found to yield a boundary comparable to simulations where the 2D grid is embedded in a larger 1D domain (Crida et al. 2007). This boundary is also used to compare to similar models in the literature (e.g. Marzari et al. 2019).

2.5. Centre-of-mass frame

Many simulations of planet–disc interactions use a grid centred on the primary star. If there is only one gravitating object, this is an inertial frame. However, with the addition of one or more planets, it is not an inertial system any more and the so-called indirect term, which is the negative of the force acting on the star,

$$\boldsymbol{F}_{\rm ind,\,star} = -\left(\boldsymbol{F}_{\rm disc} + \boldsymbol{F}_{\rm planets}\right), \tag{4}$$

has to be applied to the bodies and the gas. For more massive planets, this causes the disc to oscillate for as much as the star oscillates around the centre of mass, which is undesirable from a numerical point of view. For a full planetary system, we obtain an inertial system by choosing the centre of mass of the N-body system as the origin. The indirect term therefore vanishes except for the contribution from the disc, which reads

$$\boldsymbol{a}_{\rm ind.,\,COM} = -\frac{1}{\sum_n M_n}\sum_n M_n\, \boldsymbol{a}_{\rm disc,\,n}, \tag{5}$$

for all N-body objects indexed by n with mass M_n. To avoid any numerical drift of the centre of mass away from the origin, we shift the whole N-body system at every hydrodynamical time-step such that the centre of mass coincides with the origin, see also Thun & Kley (2018).

2.6. Gravitational interactions

Star and planets are modelled as point masses. The gravitational pull from the point masses onto the disc is implemented via their gravitational potential, which is

$$\Psi(\boldsymbol{r}) = -\mathrm{G}\sum_n \frac{M_n}{\sqrt{(\boldsymbol{r}-\boldsymbol{r}_n)^2 + \epsilon_{\rm sm}^2}} \tag{6}$$

at location $\boldsymbol{r}$, and the index n runs over all point masses with masses M_n and position vectors $\boldsymbol{r}_n$. The smoothing length is chosen to be $\epsilon_{\rm sm} = 0.6H(\boldsymbol{r})$, with the local disc scale height $H(\boldsymbol{r})$, to approximate the gravitational force in a 3D disc (Müller et al. 2012).

The back reaction from the disc onto the point masses is calculated by direct summation over all grid cells, which are indexed by k, and have masses m_k and positions $\boldsymbol{r_k}$. The total disc force acting on a point mass with index n is

$$\boldsymbol{F}_{\rm disc,\,n} = -\mathrm{G}M_n\sum_k \frac{m_k}{(\boldsymbol{r_n}-\boldsymbol{r_k})^2 + \epsilon_{\rm sm}^2}\frac{\boldsymbol{r_n}-\boldsymbol{r_k}}{|\boldsymbol{r_n}-\boldsymbol{r_k}|}, \tag{7}$$

where $\epsilon_{\rm sm}$ is the same as used for the potential.

2.7. Implementation of planetary accretion

In some simulations we include the possibility of mass accretion onto the embedded planets. We use the prescription from Dürmann & Kley (2017) and remove a fraction of mass every time-step Δt from the hydrodynamical simulation in the vicinity of the planet. More mass is removed from close to the planet than from further away. No mass is removed beyond a distance of $0.5\,R_{\rm Hill}$ from the planet's location. For full details see Dürmann & Kley (2017). The mass removed at each time-step follows the relation

$$\Delta M = f_{\rm acc}\, M_{\rm vicinity}\, \Delta t\, \Omega_{\rm K}, \tag{8}$$

where $f_{\rm acc}$ is a free parameter to control the efficiency of the accretion process. We use values of $f_{\rm acc} = 10^{-4}, 10^{-3}, 10^{-2}$ and 10^{-1} (models A$f_{\rm acc}$ with $f_{\rm acc}$ in decimal notation). Mass and angular momentum are conserved by adding the mass removed from the hydrodynamical simulation to the mass of the planet and adding an equivalent amount of angular momentum.

2.8. Additional models

In order to test our model choices, we ran additional simulations with different parameters.

To check the impact of a constant aspect ratio, we reran the standard model M9-3 with a flaring aspect ratio of $h(r) = 0.019\left(\frac{r}{\rm au}\right)^{2/7}$ (model FLARE). This flaring corresponds to a disc dominated by irradiation and $h = 0.05$ is reached at 30 au.

A resolution test was carried out by reducing or increasing the resolution by a factor of two ($\sqrt{2}$ in each direction, models M9-3 HR and M9-3 DR). See Appendix A for the comparison. To test the influence of the domain size, half resolution models (same $\Delta r/r$ as M9-3 HR) were done with a larger grid spanning from 5.2 to 520.0 au (models L, L M/2, L M/10). For the larger domain, density waves which are caused by the insertion of planets take longer to leave the domain. Therefore, $T_{\rm eq} = 59$ kyr is chosen.

Some models were run with a lower surface density but otherwise identical parameters to their sibling models. These are indicated by the M/N in their label and were initialised with N times smaller surface density compared to Eq. (2) (models M9-3 M/10, L M/2, L M/10 and PDS70 IRR M/5).

To test the effect of the centre of mass frame, we repeated some models with a coordinate system centred on the primary star. These are indicated by a -P in their labels (models VB-P, VB5-P, WD-P, WDR-P).

Most of our models do not include self-gravity. To test the implications of self-gravity, we ran two additional models with self-gravity included. This was implemented in the same way as in Baruteau (2008), but with a modified smoothing length that includes a dependence on radius in order to fulfil Newton's third law (Moldenhauer & Kley, in prep.). The two models are based on model VB5-P for runtime reasons because this model has the largest time-step. Model SG has only self-gravity enabled and SG IRR additionally solves the energy equation and considers irradiation like model IRR.

We also ran a set of models to simulate the PDS 70 system. The parameters and results are discussed separately in Sect. 5.

3. Results

In this section, we analyse the simulations listed in Table 1 with respect to their dynamical evolution and accretion properties. Each effect is described in a separate subsection.

Due to the large number of simulations performed, we do not visualise all of them. Instead, we used a representative selection to highlight the various dynamical evolutions. Unless stated otherwise, the features observed in those simulations that are not displayed are very similar but might happen at a different point in time.

The simulation outcomes are described in the following sections and an overview can be found in Table 1. The different properties listed are: outward and inward migration (↗ and ↘, Sect. 3.1), migration jumps (indicated by ✓, Sect. 3.2), single/double orbit swaps (S/DS, Sect. 3.3), and planet ejections (E, Sect. 3.6). Table 1 also refers to the corresponding figures, which show the migration history of the respective simulations.

3.1. Direction of migration

In all simulations, the planets start to migrate after gravitational feedback from the disc onto the planets is turned on. A selection of migration tracks for simulations with different planetary masses and mass ratios is shown in Fig. 3. The selection showcases the different possible behaviours of the systems.

For all combinations of planetary masses, the inner planet is migrating outward for the first 10 kyr because it only feels the positive torque contribution from the inner disc. There is no substantial contribution to the torque from the outer disc because of the large common gap opened by the two planets. Regions where the interaction of the disc would be strongest (Ward 1997) are cleared by the outer planet (Sándor et al. 2007). Vice versa, the outer planet migrates inward for the first 10 kyr. After this time, the planets are captured in a 2:1 MMR. We verified this by checking the resonant angles for an inner MMR, $\Theta_{1,2}^{2:1} = 2\lambda_2 - \lambda_1 - \varpi_{1,2}$ (Forgács-Dajka et al. 2018), where $\lambda = M + \varpi$ is the mean orbital longitude with the mean anomaly, M, and $\varpi = \omega + \Omega$ is the longitude of periapsis with the argument of periapsis, ω, and the longitude of the ascending node, Ω. These angles are indeed librating around zero (see Fig. 4 where $\Theta_{1,2}^{2:1}$ are displayed). Being

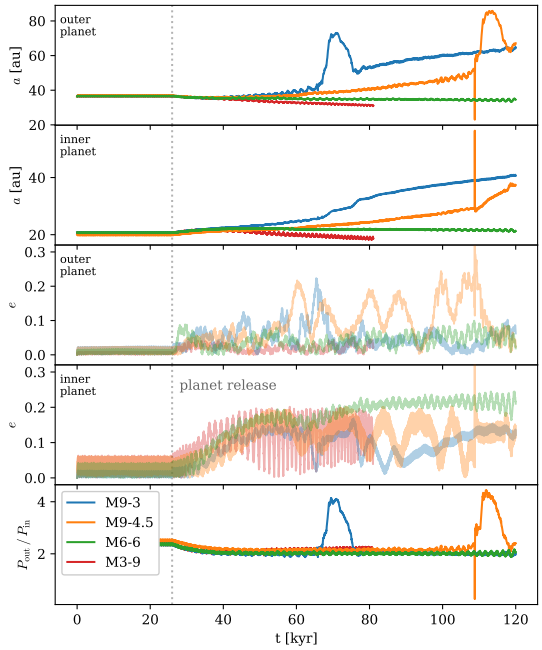

Fig. 3. Migration history for a selection of models described in Table 1 to highlight the different possible dynamical evolution of the embedded planets. The panels show, *from top to bottom*, the evolution of: the semi-major axis, a, of the outer and inner planet, their eccentricities, e, and their period ratio. The release time of the planets is marked by the vertical dotted line. Most prominent is the occurrence of fast outward migration (migration jump) for model M9-3 (blue) between 60 and 80 kyr, and a double orbit swap at 110 kyr followed by a migration jump for model M9-4.5. At the time of the double orbit swap at $t \sim 110$ kyr, $e_{in} = 0.38$ and $e_{out} = 0.58$. They are cut out to increase the visibility of the rest of the data.

locked in resonance, the planets then migrate in unison with a direction that depends on whether the positive torque contribution of the inner disc (inside the common gap) is larger in magnitude than the negative torque contribution from the outer disc (outside the common gap). As these torque contributions depend on the respective planetary mass, the direction of migration can vary. If the inner planet is more massive than the outer planet, the system can migrate outwards as found initially for the Jupiter–Saturn system by Masset & Snellgrove (2001). Indeed, Fig. 3 shows outward migration for the M9-3 and M9-4.5 models for which the inner planet is more massive than the outer one. Conversely, the planets migrate inward for a more massive outer planet as in model M3-9. For equal-mass planets (M6-6), the system still migrates inward, but with a lower migration rate.

3.2. Migration jumps

Simulations in which the planet pair shows outward migration occasionally exhibit an additional process, which we call a "migration jump":

1. the outer planet embarks on a rapid outward migration covering tens of au in a time period of a few thousand years;
2. after reaching a maximum radius, it stays in this region for several thousand years, occasionally for up to tens of thousands of years;
3. it migrates back inward, again on a short timescale, until it locks back into resonance with the inner planet.

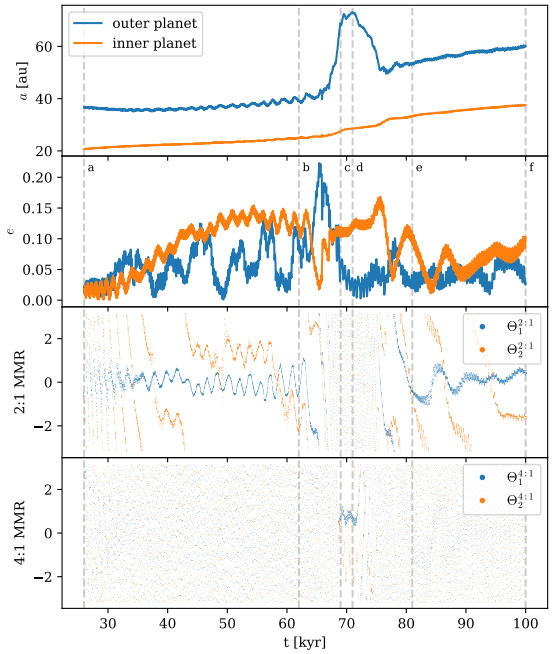

Fig. 4. Zoom-in on a migration jump in model M9-3 including the time leading up to and following the event. The panels show, *from top to bottom*, the evolution of: the semi-major axis of both planets, their eccentricities, the 2:1 MMR angles, $\Theta^{2:1}_{1,2} = 2\lambda_2 - \lambda_1 - \varpi_{1,2}$, and 4:1 MMR angles, $\Theta^{4:1}_{1,2} = 4\lambda_2 - \lambda_1 - 3\varpi_{1,2}$. The vertical lines correspond to the snapshots shown in Fig. 5.

Two examples of a migration jump can be seen in Fig. 3. This process can repeat itself multiple times (see Fig. B.1).

Figure 4 shows a zoom into one migration jump of our standard M9-3 model focussed on the time leading up to the event and some time afterwards. It shows from top to bottom: the semi-major axis of both planets, their eccentricities, the 2:1 MMR angles, and the 4:1 MMR angles. The MMR angle variables correspond to an inner MMR (Forgács-Dajka et al. 2018). The two-dimensional surface density distribution of model M9-3 is displayed in Fig. 5, where panels a–f show the disc prior, during, and after the migration jump. The times of the individual snapshots are indicated in Fig. 4 by the vertical lines. Panel a of Fig. 5 shows the disc at that point in time when disc feedback is turned on and the planets are allowed to migrate.

In the following paragraphs we examine the migration jump process more closely by analysing the behaviour around the time of each of the six snapshots of model M9-3.

a) Prior to the migration jump, both planets migrate outward in 2:1 MMR. During this time, the eccentricity of the inner planet, $e_{\rm in}$, grows up to 0.15, while the eccentricity of the outer planet, $e_{\rm out}$, fluctuates up to 0.125. The increase in eccentricity comes from the interaction of the planets with the vortex that is formed outside the common gap. Faint spiral arms are visible in the common gap during this epoch (see panel b in Fig. 5).

b) At 64 kyr, $e_{\rm in}$ drops significantly while $e_{\rm out}$ rises up to 0.2 and the 2:1 MMR is broken. Due to its eccentric orbit, the outer planet comes close to the inner edge of the outer disc (see panel b of Fig. 5). This is close enough to sufficiently enhance the mass flow across the planet's orbit and produce co-orbital torques. These torques are positive, because gas with higher angular momentum flows inwards where it has a lower angular momentum. The difference in angular momentum is deposited onto the planet causing a positive torque. What follows is a phase of type III rapid outward migration (Pepliński et al. 2008) and the outer planet moves out from 40 au at 65 kyr to 72 au at 70 kyr, covering 32 au in only 5 kyr. More complex structures can be seen in the disc (see panel c in Fig. 5) which are the result of overlapping spiral arms and the outer planet opening a gap. During this time $e_{\rm out}$ relaxes back to low values.

c) The fast outward migration stops at the location of the 4:1 MMR with the inner planet (see the third panel from the top in Fig. 4 where the resonant angles $\Theta^{4:1}_{1,2}$ are displayed). The two planets remain in the 4:1 MMR for about 4 kyr at $t \sim 70$ kyr, where the outer planet remains around 75 au.

d) Afterwards the 4:1 resonance is broken and the outer planet migrates back inward by 22 au within 3.5 kyr.

e) It ends up back in 2:1 MMR with the inner planet. The inner planet migrates outwards during the jump since the positive torque from the inner disc is dominating over the negative contribution from the outside which is weakened due to the common gap.

Migration jumps occur in a variety of models but details such as the distance or duration of specific sub-processes vary from model to model. The location where the jump stops is not necessarily at the 4:1 period commensurability for all simulations, as can be seen for example in Fig. B.1 which also shows period ratios close to 4.5 and 5. In general, the location can be expected to be determined by the interplay of N-body dynamics (the resonances), gas dynamics, and the rearrangement of gas density around the outer planet. Migration jumps only happen in the models in which: migration is directed outward, a vortex forms outside the common gap, and the disc mass is sufficiently high.

From these observations we can decipher two criteria that must be met for migration jumps to occur. First, the planet mass ratio must be such that the pair of planets migrates outwards. This can be the case when the inner planet is more massive than the outer one. Second, the disc mass needs to be high enough to facilitate sufficiently fast outward migration. This migration speed is needed to allow for the formation of a significantly massive vortex which in turn leads to large eccentricities of the outer planet. These large eccentricities are needed for type III rapid outward migration to be triggered. For insufficiently high disc masses, the system only migrates outward smoothly and no vortex forms (see also the low-disc-mass results for model PDS70 IRR M/5, Fig. 11).

3.3. Orbit swaps

In addition to migration jumps, some models show other features as well. For example, the planets in model M9-4.5 swap their orbits in close succession just before a migration jump (Fig. 3 at 110 kyr). The orbital eccentricities reach very high values during the swapping process, for example $e_{\rm out} = 0.58$ in model M9-4.5. The accreting model, A0.01, also experiences a double swap (Fig. 7 at 90 kyr). A model with different resolution, model L, shows a single orbit swap (see Fig. 9). As a consequence, the inner planet is less massive than the outer one and the migration direction changes from outward to inward. Just after the single orbit swap, the outer, more massive planet undergoes a small migration jump (5 au). The models with self-gravity enabled also show orbit swaps. Model SG shows a single orbit swap following two migration jumps and model SG IRR shows a migration jump followed by a double orbit swap and a subsequent single orbit swap. In each of our non-self-gravitating simulations where an orbit swap (single or double) happens, a migration

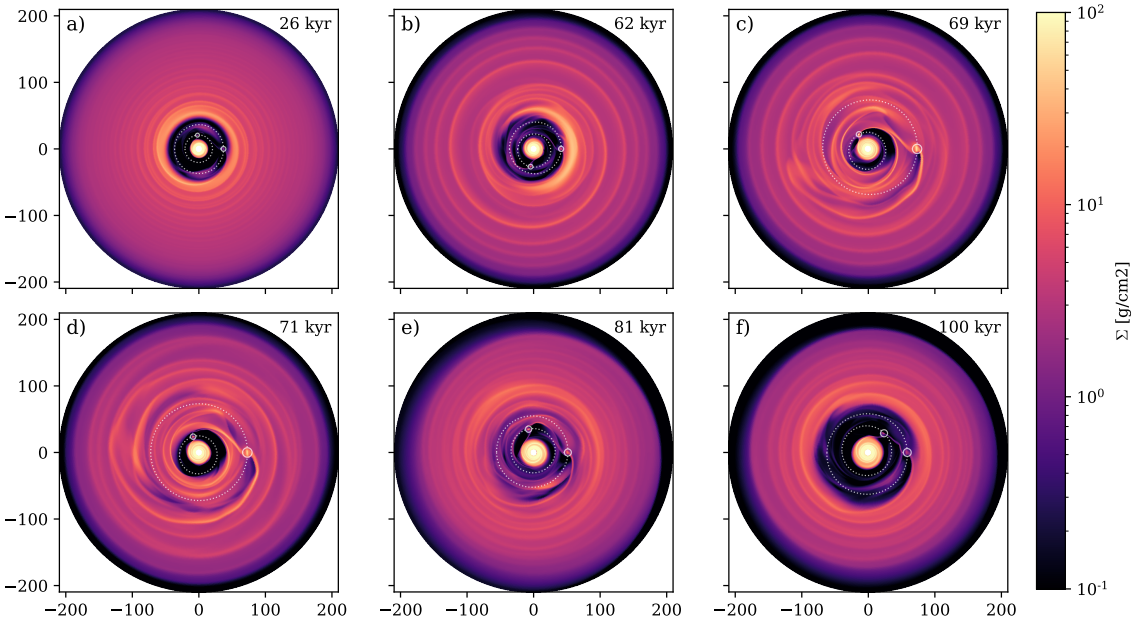

Fig. 5. Snapshots of the surface density for model M9-3 showing the disc at different times: prior (*panels a and b*), during (*c and d*), and after (*e and f*) a migration jump. The current orbits of the two planets are marked by the dotted white ellipses and the planetary Hill spheres are indicated by the small circles. Coordinate labels show the position in au. The snapshots are rotated to have the outer planet fixed on the horizontal axis to the right of the origin. Time inside the simulation is shown in the upper right corner. The time of a particular snapshot in the time-line of the simulation can be located on the annotated vertical lines in Fig. 4. For synthetic observations of the snapshots, see Fig. 10.

jump follows after a few more orbits. Events like orbit swaps have already been observed in the literature, especially in planetary systems with more than two massive planets (e.g. Marzari et al. 2010; Zhu et al. 2011).

3.4. Vortex outside the gap

During the regular outward migration of the planet pair, an overdensity is formed just outside the common gap, which is visible as the banana-shaped high-density structure just beyond the outer planet in panel b of Fig. 5. This is a sign of vortex formation by embedded planets in discs, which are known to occur for massive planets and/or low viscosity discs (e.g. Koller et al. 2003; Ataiee et al. 2013). Figure 6 shows a zoomed-in view of the overdensity and shows the surface density and streamlines in a system corotating with the overdensity. The eye of the vortex is visible in the upper right quadrant. Vortensity and surface density are analysed in more detail in Appendix C, where it is confirmed that the overdensity is indeed a vortex. In all our simulations in which a migration jump happened we also observed a vortex forming outside the common gap.

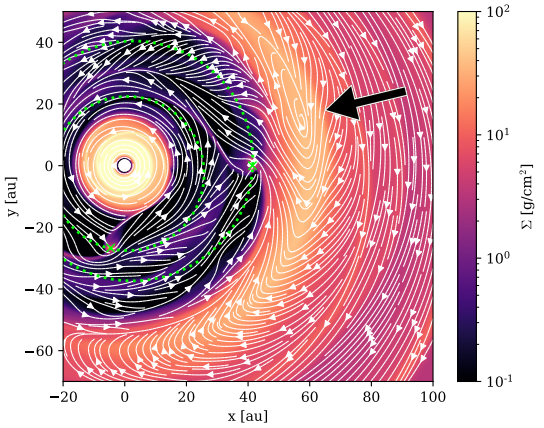

Fig. 6. Zoom-in on panel b of Fig. 5 showing the surface density and velocity streamlines. The streamlines are computed in a frame corotating with the disc at 59 au. The streamlines are closed in the region indicated by the black arrow, showing that the overdensity is a vortex. The orbits of the planets are indicated as the green dotted lines.

3.5. Accretion onto the star and planets

3.5.1. Planetary accretion

The accretion rates onto the planets and the star are shown alongside the dynamical evolution of the system in Fig. 7. Mass accretion onto the planets is turned on when the planets are released. The accretion rates onto the inner planet and the outer planet, $\dot{M}_{\rm in/out}$, scale approximately linearly with $f_{\rm acc}$, as one might expect (see Eq. (8)). This behaviour holds during the inward migration of the outer planet into 2:1 MMR and during outward migration of the pair as long as the eccentricity of the outer planet remains below $e_{\rm out} = 0.1$. Due to the larger relative size of the inner planet's Hill sphere ($R_{\rm Hill}/a \propto M_{\rm pl}^{1/3}$) and its smaller orbital period, $\dot{M}_{\rm in}$ is larger than $\dot{M}_{\rm out}$. This is because the mass available for accretion onto the inner planet is supplied via the streamers within the common gap. The accretion rate is then determined by the ratio between a planet's region of influence ($R_{\rm Hill}$) and the length of its orbit (a), that is, by how much of the mass around its orbit is accessible to it, and by its orbital frequency, in other words, how often it encounters these streamers. The larger accretion rate of the inner planet

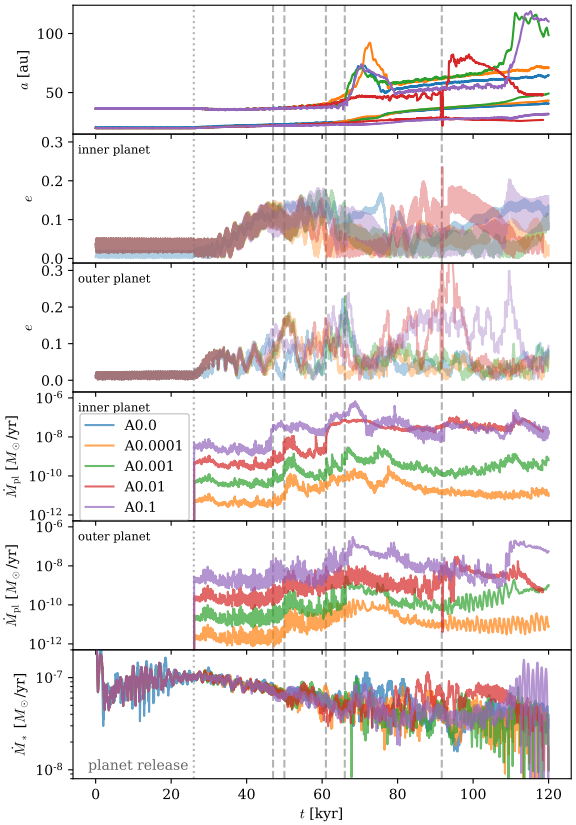

Fig. 7. Evolution of accretion rates, migration, and eccentricities for the models with planetary accretion. Then panels show *from top to bottom*: the semi-major axis of both planets, $a_{\rm in/out}$, the eccentricity of the inner planet and that of the outer planet, $e_{\rm in/out}$, planetary mass accretion rate onto the inner and outer planet, $\dot{M}_{\rm in/out}$, and the mass accretion rate onto the star smoothed with a moving average of length 1.185 kyr, $\dot{M}_*$. The vertical dashed lines indicate events of interest and are referred to in Sect. 3.5. Model A0.0 is an alias for model M9-3.

also shows that the outer planet only receives a small fraction of the gas that otherwise travels through the common gap and does not starve the accretion of the inner planet. During these quieter times, the models behave very similarly, and independently of $f_{\rm acc}$, although the $f_{\rm acc} = 0.1$ case shows the same events at a slightly earlier time.

Around $t = 47$ kyr (first vertical dashed line in Fig. 7) when $e_{\rm out}$ rises to values above 0.1, $\dot{M}_{\rm in/out}$ increases as well. This can be explained by the following argument. When the outer planet comes close to the outer gap edge at apastron, it "shovels" disc material inwards into the common gap (see panel b in Fig. 5 for the emerging structures). Thus, there is more gas available inside the planets' Hill spheres to be accreted. This way, outward migration with pumping of eccentricities can enhance planetary accretion. Variabilities of $\dot{M}_{\rm in/out}$ occur on timescales of around two times the period of the outer orbit. $\dot{M}_{\rm in}$ follows the same trends as $\dot{M}_{\rm out}$ with a delay of around one outer period (∼200 yr) because of the finite gap-crossing time.

At around $t = 50$ kyr (second vertical dashed line in Fig. 7), $\dot{M}_{\rm in/out}$ reach their highest values prior to the migration jumps before they decrease when $e_{\rm out}$ relaxes to lower values. During the smooth phase of outward migration, $\dot{M}_{\rm in/out}$ can be increased by a factor of 10–20 compared to inward migration.

Just before the onset of a migration jump (third vertical dashed line in Fig. 7), $e_{\rm out}$ and $\dot{M}_{\rm in/out}$ rise again. Models A0.0001, A0.001, and A0.1 show a migration jump soon after, at around $t \sim 66$ kyr. During the jump (fourth vertical dashed line in Fig. 7), $\dot{M}_{\rm out}$ is comparable to $\dot{M}_{\rm in}$ because the outer planet moves through the disc and has a higher density of gas inside its Hill sphere. $\dot{M}_{\rm in}$ also rises as significant amounts of gas are scattered inward during the jump. This can result in a 50–100 fold increase compared to the values during inward migration.

A notable exception to the described behaviour is model A0.01. There, the first migration jump fails, which gives rise to another distinct behaviour. Similar to the other models, the outer planet increases the mass flow through the gap by "shovelling" gas into it. However, unlike the other models, it does not embark on a jump and continues to supply material to the inner planet. This causes the gas density of the inner planets Hill sphere to rise and $\dot{M}_{\rm in}$ to rise tenfold, matching the rates of the A0.1 model. At $t = 91.7$ kyr (fifth vertical dashed line in Fig. 7), $\dot{M}_{\rm out}$ on A0.01 also matches the values of A0.1, where it finally embarks on a jump and its eccentricity has risen to $e_{\rm out} = 0.2$.

Figure 8 shows the time evolution of the mass accreted onto the planets and the star and the total disk mass. Depending on the efficiency of planetary accretion, $f_{\rm acc}$, the changes in planet mass can be substantial, as seen in the first two panels. The most extreme case is the outer planet of model A0.1 which has almost doubled its mass at the end of the simulation.

3.5.2. Stellar accretion

Mass accretion onto the star, $\dot{M}_*$, is calculated by summing the mass that leaves the inner boundary over the output interval of 11.8 yr. It does not show a dependence on the efficiency of planetary accretion, $f_{\rm acc}$. The mass lost through the inner boundary is not added to the primary star because its contribution to the total stellar mass over the time-span of the simulations would be smaller than 1% (see third panel of Fig. 8) and can be neglected. For a theoretical estimate of the stellar mass accretion rate we can use the viscous mass accretion rate of the unperturbed disc at the inner boundary (≈2 au) which is $\dot{M}_{\rm disc} = 3\pi\Sigma\nu = 5.3 \times 10^{-9}\, M_\odot\,{\rm yr}^{-1}$. In the simulations, the mass accretion rates onto the star through the inner boundary fluctuate between 10^{-8} and $10^{-7}\, M_\odot\,{\rm yr}^{-1}$. One should keep in mind that the theoretical estimate does not take into account the presence of the massive embedded planets, which can be expected to substantially alter the dynamics of the disc. This discrepancy could be explained by the inner outflow boundary and changes in the disc structure. Because there is no pressure support from the inside, there is a high mass flow in the radial direction. An additional contribution arises when the disc becomes eccentric in its inner region. The simulations show gas eccentricities between 0.1 and 0.4 in the inner 10 au of the domain, which are a result of the gravitational interaction of the planets and the disc. Since the boundary is perfectly circular by design, any gas that is on an eccentric orbit which overlaps with the boundary is lost through the boundary because it cannot reenter, although its orbit would bring it back into the domain. Therefore, the accretion rate onto the star, $\dot{M}_*$, can only be seen as an upper limit.

Models VB-P and VB5-P, which employ a viscous boundary to avoid abnormally high mass flow through the inner boundary, show mass accretion rates at a similar level, with values around $\dot{M}_* \sim 2 \times 10^{-8}\, M_\odot\,{\rm yr}^{-1}$ for both choices of $v_{\rm in}$ ($\beta = 1$ or 5 in Eq. (3)). This means, that the surface density of the inner disc must be enhanced compared to the initial condition, which is indeed the case for simulations showing outward migration.

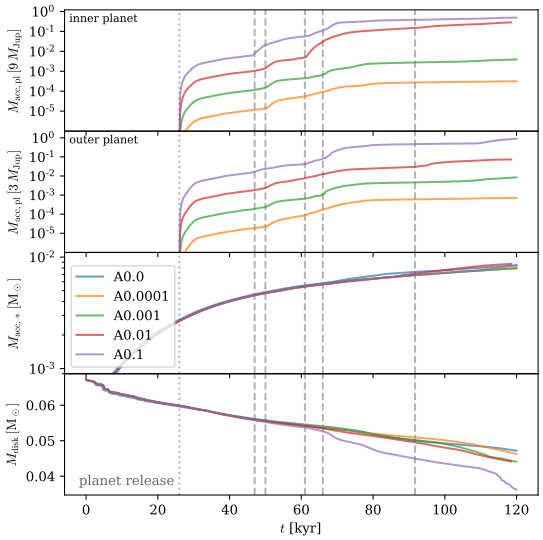

Fig. 8. Evolution of the mass accreted onto the planets and the star and the disk mass for the models with planetary accretion. The panels show *from top to bottom*: the mass accreted onto the inner and outer planet, $M_{\rm acc,pl}$, the mass which leaves the disc through the inner domain, $M_{\rm acc,*}$, (i.e. the mass that would be accreted onto the star, but which is not added to it in the simulations), and the evolution of the total disc mass, $M_{\rm disc}$. The evolution of $M_{\rm disk}$ also includes the mass leaving the outer domain. The values are in units of the initial mass of the respective object for the accreted masses and in stellar masses for the disc mass. The dashed vertical lines correspond to the ones in Fig. 7.

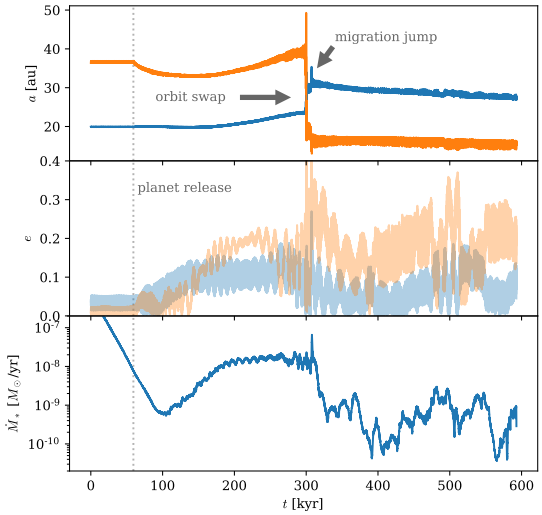

Fig. 9. Migration and accretion for model L showing the orbit swap and how $\dot{M}_*$ depends on the direction of migration. The panels show (*top*) semi-major axis, a, (*middle*) eccentricity, e, and (*bottom*) migration onto the star $\dot{M}_*$. The vertical dashed line indicates the time when planets are allowed to migrate.

This result can be taken as an indication that the outflow boundary in our simulations does not strongly overestimate the mass accretion through the inner boundary. On the contrary, in our simulations, the stellar accretion rate seems to be determined by the amount of gas that can be supplied from further out in the disc.

A special behaviour was observed in model L which exhibits a single orbit swap, as explained in Sect. 3.3. Because migration changes from outward to inward in an otherwise unchanged disc, this model gives us the opportunity to study how $\dot{M}_*$ depends on the direction of migration and the ordering of the planets. Figure 9 shows migration and eccentricities of both planets (top and middle panel) and $\dot{M}_*$ smoothed with a moving average of length 1.185 kyr (bottom panel) for model L. The small $\dot{M}_*$ at $t = 100$ kyr is due to the initialisation phase when the inner disc is mostly depleted by accretion through the inner boundary. In the time after planet release, the inner disc recovers parts of its mass and reaches up to a tenth of its initial value of Σ at $t = 150$ kyr and a fourth at $t = 250$ kyr by mass transfer through the gap. This is enough to start outward migration. In the 120 kyr of outward migration leading up to the migration jump, accretion is enhanced to $\dot{M}_* \approx 2 \times 10^{-8}\,M_\odot\,{\rm yr}^{-1}$ (see bottom panel of Fig. 9). After the planets swap orbits at 300 kyr, migration changes its direction to inward and accretion deceases to values $\dot{M}_* < 10^{-9}\,M_\odot\,{\rm yr}^{-1}$. The eccentricity of the massive planet and the value of $\dot{M}_*$ follow similar trends (see Fig. 9). However, both values are not proportional which can be seen by comparing the values at 200 and 520 kyr where the eccentricity of the massive planet is at a value of 0.1, but $\dot{M}_*$ is at least ten times smaller at the later time. This rules out the possibility that the increase in $\dot{M}_*$ during outward migration is a result of the outflow boundary effect explained in the last paragraph. During the event of the orbit swap, there is no abnormally high mass loss of the disc. The disc mass in the whole domain only changes from 0.145 to 0.14 $M_\odot$ after the planets are released, and so the change in $\dot{M}_*$ cannot be explained by the disc suddenly loosing most of its mass. Thus, $\dot{M}_*$ depends on the direction of migration and it is enhanced for outward-directed migration. The model also shows that mass can be transported through a common planet gap at a substantial rate. Summarising the results, we can report the following findings:

1. Mass accretion through the disc can be sustained even in the presence of a large common gap carved by a pair of massive planets.
2. Planetary accretion can be substantially increased when a pair of planets is migrating outward in 2:1 MMR where the increase in mass accretion can be 10–20 fold compared to inward migration.
3. During extreme events like a migration jump, when a planet travels through previously unperturbed disc regions, the increase can be even higher with values increased 50–100 fold compared to inward migration.
4. Migration rates seem not to be affected by the choice of $f_{\rm acc}$ during times of smooth outward migration. However, the accretion efficiency can change the type of occurring events and the timing when they happen.
5. Mass accretion rates onto the star seem not to be affected by the choice of $f_{\rm acc}$.

3.6. Planet ejection

In some models, the planetary system is ejected either during a first or second migration jump. The outer planet is ejected first and the inner planet is ejected 2–3 kyr later. The models affected are VB, VB5, WD, and WDR. All of them use a disc (hydrodynamical simulation) centred around the centre of mass of the star and the two planets and have an inner boundary condition different from outflow. The affected inner boundary conditions are the viscous boundary with $v_{\rm in} = v_{\rm visc}$ and $v_{\rm in} = 5v_{\rm visc}$, the

outflow boundary with an additional wave-damping zone, and the reflective boundary with an additional wave-damping zone. We repeated all the affected models with the disc (hydrodynamical simulation) centred on the primary star (models VB-P, VB5-P, WD-P, and WDR-P). In the primary frame, no ejection occurred during the simulation time which was chosen to be at least 50 kyr longer than the time when the ejection happened in the corresponding centre-of-mass model.

In all the models, the inner boundary is located at 2.08 au and the wave damping zone stretches from the inner boundary to 4.16 au. This comparison shows that the inner boundary can be crucial for determining the fate of an embedded planetary system, even if planets are further out at around 50 au.

All ejection occurred in models where the primary star was moving with respect to the boundary. In the centre-of-mass frame, the primary moves up to 0.4 au, which is 20% of the inner boundary radius. This equivalently means that the boundary is moving 0.4 au relative to the star.

The difference is not only a numerical artefact, but the physical boundary condition is different for the models in the centre-of-mass frame compared to the primary frame. Using the viscous boundary condition in the primary frame for example, the radial speed at a fixed radius from the star is set to the viscous speed. This is a physically motivated choice. Since the hydrodynamical grid is centred on the primary, this boundary condition can be implemented in a simple way by setting the velocity at the inner boundary, which is at a constant distance from the star in all directions. Using the same implementation in a centre-of-mass frame, as we did in our models, the distance at which the radial velocity is set to the viscous speed is different depending on the azimuthal direction and is even varying over time. Thus, the resulting boundary condition is physically different from the case of the primary frame and is no longer physically plausible.

In all cases, except the zero-gradient boundary condition case, the unphysical boundary condition leads to strong perturbations close to the inner boundary, which at some point in time can no longer be resolved by the hydrodynamical simulations. In the resulting numerical instability, the perturbations grow unbound and destroy the disc and coincidently also eject the planets without any close encounter or instability in the N-body system.

3.7. Final location of outward migration

Most models were run for a simulation time of 120 kyr. At this point in time, outward migration did not halt in any of the models. Some models were integrated for a longer time, such as for example the M9-3 model in which the outer planet reached 133 au at $t = 226$ kyr. In this specific case, the outer gap edge is located at 162 au and the surface density of the outer disc is two orders of magnitude lower than that of the inner disc. As a result, the negative torque contribution from the outer disc becomes diminished and outward migration continues. Our models suggest that, in the scenario studied here, in the case of outward migration of a pair of planets in a disc of sufficiently high mass, the final location of the planet pair will be near the outer edge of the disc.

4. Observability

To evaluate the possibility whether or not the effects of migration jumps could be observed in real systems we performed synthetic observations. Though the timescale of the processes discussed here is quite short, some tens of thousands of years if we also include the time the structural changes last in the disc (see panels e and f of Figs. 5 and 10), the synthetic observations might be applicable to systems in which we directly observe embedded planets, such as PDS 70. These observations are, after all, just snapshots in time of the real system. With a disc lifetime of the order of roughly 1 Myr, the migration jump timescale of 10 kyr amounts to a significant fraction, that is, in the region of 1%. Considering the ever-increasing number of detected (proto-)planetary systems and the apparent richness in substructure therein (Andrews et al. 2018), the following synthetic images might provide an explanation for a subset of future disc observations. Our synthetic images were produced by calculating the thermal emission using RADMC3D (Dullemond et al. 2012). This emission was then postprocessed using the CASA package (McMullin et al. 2007) to simulate the instrumental effects produced by ALMA. The resulting synthetic observations of the M9-3 model are shown in Fig. 10 and can be directly compared to the plots of surface density in Fig. 5. The simulation snapshots are the same in the respective panels.

4.1. Radiative transfer model

In order to compute the thermal dust emission for the individual snapshots of the M9-3 model we convert the gas surface density profiles into a three-dimensional dust density model which serves as input for the radiative transfer calculations with RADMC3D. Please keep in mind that, in principle, dust follows its own dynamics and is only partially coupled to the gas. Our synthetic images are therefore only an approximation of what would be the result of the actual dust distribution taking into account the proper gas–dust interaction. In the model we employ eight dust species with a combined dust to gas mass ratio of 10^{-2}. The dust grain sizes are logarithmically evenly spaced, ranging from 0.1 μm to 1 mm. The number density size distribution of the dust grains follows the MRN distribution $n(a) \propto a^{-3.5}$, where a is the grain size.

Dust settling towards the midplane is considered following the diffusion model of Dubrulle et al. (1995) with dust vertical scale height:

$$H_\mathrm{d} = \sqrt{\frac{\alpha}{\alpha + \mathrm{St}}} H, \tag{9}$$

where St is the local Stokes number,

$$\mathrm{St} = t_\mathrm{stop}\, \Omega_\mathrm{K} = \frac{\pi}{2} \frac{a \rho_\mathrm{d}}{\Sigma}, \tag{10}$$

where the grain density $\rho_\mathrm{d} = 3.0\,\mathrm{g\,cm^{-3}}$. We assume a Schmidt number of one. Furthermore, the aspect ratio is assumed to be flared with radius, that is, H/r scales as $(r/r_0)^\gamma$ where γ is the flaring index. In all the synthetic images, a flaring index of $\gamma = 0.25$ was chosen.

For the extension in the polar direction, 32 cells are equally spaced in their angular extent between $\theta_\mathrm{lim} = \pi/2 \pm 0.3$ resulting in a maximal spacial extent of $z_\mathrm{lim} = r\,\sin(\pm 0.3)$. The vertical disc density profile is assumed to be isothermal and the conversion from the surface density to the local volume density is calculated as follows:

$$\rho_\mathrm{cell} = \frac{\Sigma}{\sqrt{2\pi} H_\mathrm{d}} \cdot \mathrm{erf}^{-1}\left(\frac{z_\mathrm{lim}}{\sqrt{2} H_\mathrm{d}}\right) \tag{11}$$

$$\cdot \frac{\pi}{2} H_\mathrm{d} \frac{\left[\mathrm{erf}\left(\frac{z_+}{\sqrt{2} H_\mathrm{d}}\right) - \mathrm{erf}\left(\frac{z_-}{\sqrt{2} H_\mathrm{d}}\right)\right]}{z_+ - z_-}. \tag{12}$$

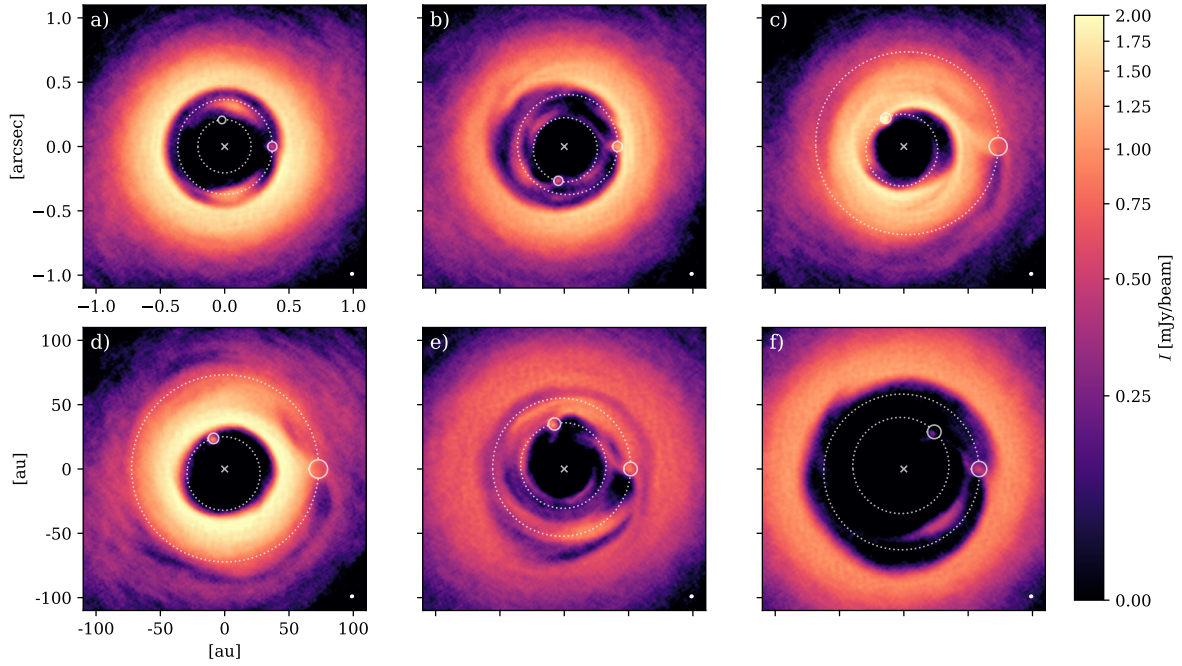

Fig. 10. Synthetic ALMA observations at 855 μm of the disc in model M9-3 (assuming a distance of 100 pc) at different times: prior (*a* and *b*), during (*c* and *d*), and after (*e* and *f*) a migration jump. The panels coincide with the ones in Fig. 5 but they show the intensity from simulated observations instead of surface density and are zoomed-in to the inner ±100 au of the disc. Coordinate ticks are the same in all panels and values are given in arcseconds in the *top left panel* and the corresponding values in au are shown in the *bottom left panel*. The ellipse in the bottom right corner of each panel indicates the beam size of 33 × 30 mas. The location of the star is indicated by the small cross symbol in the centre. The current orbits of the two planets are marked by the dotted white ellipses and the planetary Hill spheres are indicated by the small circles.

The error function term is a correction for the limited domain extent in the vertical direction that would otherwise lead to an underestimation of the total dust mass. Similarly, the second correction term accounts for the finite vertical resolution, which is especially important for thin dust layers with strong settling towards the midplane. The coordinates z_+ and z_- are the cell interface locations in the polar direction along the numerical grid. For each grain size bin and a wavelength of 855 μm, the corresponding dust opacities were taken from the `dsharp_opac` package which provides the opacities presented in Birnstiel et al. (2018). These opacities are based on a mixture of water ice, silicate, troilite, and refractory organic material. In the RADMC3D model, the central star is assumed to have solar properties with an effective temperature of 6000 K at a distance of 100 pc. For the thermal Monte-Carlo simulation a number of $n_{\rm phot} = 10^8$ photon packages were used, and $n_{\rm phot\_scat} = 10^7$ photon packages were used for the image reconstruction. Scattering of photons is assumed to be isotropic.

As a result of our assumption that gas and dust share the same spacial distribution, the surface density of dust in the inner disc is very high. This leads to the formation of a hot dusty wall on the inside that prevents us from seeing the features in the outer disc close to the planets. Therefore, we reduce the dust density for the inner region by a factor of 10^{-5} in the radiative transfer model. The cutoff radius for this reduction in dust density is set to 23 au for the first five snapshots in Fig. 10 whereas this is extended to 26 au in Fig. 10. Since dust is expected to drift within the inner disc isolated by the two planets, which leads to a reduction in dust density there, this numerically motivated measure has also some physical foundation. However, full consideration of the gas–dust interaction would be necessary to clarify the difference in strength between the effects. Here, the reduction is a numerical measure to help visualisation.

RADMC3D uses different and arguably more realistic opacities to calculate the dust temperatures compared to the opacities used in the hydrodynamical simulations, which is why the dust temperatures are different. Compared to the gas temperature in the IRR model (Fig. B.2) and depending on the dust grain size, the resulting dust temperatures are three to five times higher in the gap region, which is directly illuminated because of the reduction in dust density of the inner disc, and two to three times higher in the outer disc close to the gap and approximately the same value at 100 au.

4.2. Synthetic imaging

We use the task `simalma` from the CASA-5.6.1 software to simulate the detectability of the various features present in the model. A combination of the antenna configurations `alma.cycle5.8` and `alma.cycle5.5` was chosen. The simulated observation time for configuration "8" is 4 h while the more compact configuration is integrated over a shorter time of 53 min.

A simple auto-cleaning procedure was applied to reduce the artificial artefacts from the incomplete *uv*-coverage. In the scope of this paper the prescription is sufficient for estimating the observability of the features of interest. Consistent with the radiative transfer model, the observed wavelength is simulated to be at 855 μm, corresponding to ALMA band 7. The resulting beam size is 33 × 30 mas. For model M9-3, the rms noise intensity ranges from 40 μJy beam^{-1} to 70 μJy beam^{-1}. The synthetic images are shown in Fig. 10. In the rest of this section,

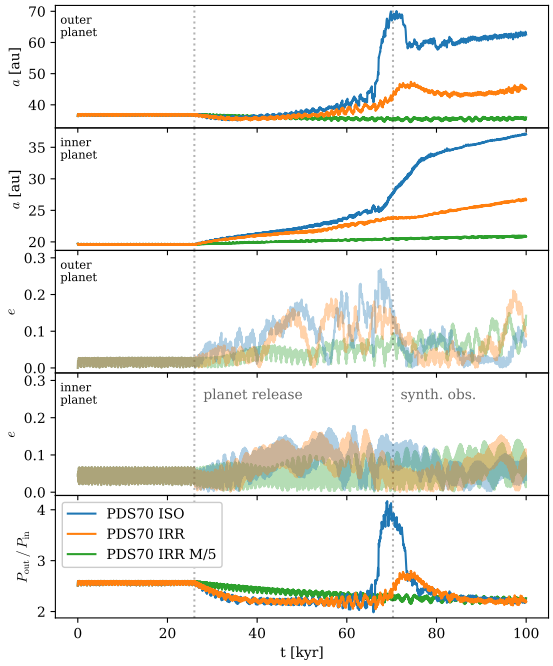

Fig. 11. Migration history (as in Fig. 3) for the PDS 70 models. A migration jump occurs for both equations of state in the case of a high-surface-density model (PDS70 ISO and PDS70 IRR). The model with a fifth of the surface density (PDS70 IRR M/5) shows only very moderate outward migration. The left vertical dotted line shows the time of planet release. The right vertical dotted line shows the time of the synthetic observations shown in Fig. 12.

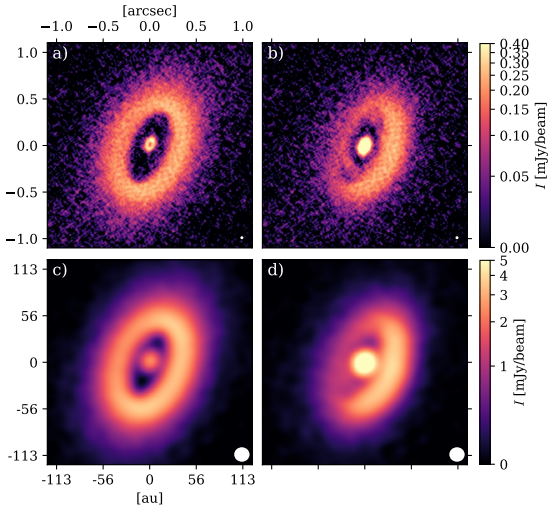

Fig. 12. Synthetic observations of the PDS 70 models. Disc mass increases *from left to right* and resolution decreases *from top to bottom*. For a lower disc mass, the appearance is smooth and symmetric, showing a large gap. At higher disc mass, azimuthal asymmetries appear and additional substructures emerge for higher resolution. *Left column (a and c)*: low-disc-mass model (PDS70 IRR M/5) at $t = 70.3$ kyr (see vertical line in Fig. 11) and *right column (b and d)*: high-disc-mass model (PDS70 IRR) at the same point in time. *Top row (a and b)*: generated with the same angular resolution as Fig. 10 while only the smaller ALMA antenna configuration was used for the *bottom row (c and d)*, resulting in a larger beam size. The beam size is indicated in the bottom right corner of each image.

we describe the different features that are visible in the synthetic images. All references are to Fig. 10, unless stating otherwise.

4.3. Features in synthetic images

Our synthetic images show a large inner hole in the disc which is growing over time. This can appear as a circular hole at some points in time (panels a and f of Fig. 10) or as an eccentric hole at other times (panels b–d). As we removed the dust artificially, the inner hole might actually be partially filled with dust and still be showing a visible inner disc. Because our cut-off radius is 26 au at maximum, such a system with an inner disc would show a large gap ranging from about 20 au in size for panel b to around 75 au for the disc in panel f. For an example where only part of the dust is removed, see the PDS 70 models in Fig. 12.

Our simulations produce a number of non-axisymmetric features in the synthetic observations. In the following sections, we investigate these in more detail. Emission from the location of the planets is clearly visible in the synthetic observations. Very localised, point-like features around the planet are visible either from a single planet (panels a, c, and d) or from both planets (panels b, e, and f). These emerge because of mass accumulations in the planets' Hill spheres. During a migration jump (panels c and d), the outer planet is deeply embedded in the disc, and so no separate point-like emission is visible from the outer planet.

The vortex discussed in Sect. 3.4 is also visible in the synthetic images. It appears as a bright region on the right side of panel b causing a visible non-axisymmetric feature. Depending on the line-of-sight inclination of the disc and beam size, the asymmetry caused by the vortex can even be enhanced (see panels b and d of Fig. 12).

When the outer or inner planet gets close to the gap edge, the outer part of the spiral arm can be visible in the synthetic images, connecting the planet with the outer disc with a visible spur. This is the case for panels b, e and f with the outer planet and panels c and e with the inner planet.

At the time when the planets are released, there is still some material present in the L_4 and L_5 points of the outer planet. This is an artefact of the initialisation process. Although it is also visible in the synthetic observations (panel a), it does not constitute a realistically observable feature but rather an artefact of the initialisation and the assumption that dust and gas share the same spacial distribution. However, when the outer planet migrates back in during a migration jump, a substantial amount of material survives as a mass accumulation in Lagrangian point L_5 (trailing the planet). The accumulation is clearly visible in panel e. This feature can persist for more than 20 kyr as shown by its presence in panel f.

During times of high mass transfer through the common gap, surface density in the spiral arms in enhanced. Panels b, c, and e show clear signs of spiral arms even in the synthetic images. The spiral arms of both planets are periodically cut off by the passing of the other planet and locally merge with parts of other spiral arms. This causes additional arc-like features such as the ones in panels b and e.

Another arc-like feature can be produced during the migration jump. Panels c and d show a void behind the planet in the lower right quadrant at a radius of approximately 75 au. These voids are 30 deg (panel c) to 60 deg (panel d) in width in the azimuthal direction and are caused by the gap being carved into

the previously unperturbed disc during rapid outward migration (Pepliński et al. 2008).

Just after the migration jump (panel e), multiple substructures can be seen inside the orbits of the planets. This shows that more than one of the features presented above can exist in a disc at the same time.

5. Modelling of a real system: PDS 70

PDS 70a is a 5.4 ± 1.0 Myr-old K7-type star with a mass of $0.76 \pm 0.02\,M_\odot$ and luminosity outflow $L_* = 0.35 \pm 0.09\,L_\odot$ (Müller et al. 2018). It is at a distance of 113.43 ± 0.52 pc (Gaia Collaboration 2018). Recently, it was found to host two giant planets, PDS 70b and PDS 70c, which were observed via direct imaging. Their orbits are close to a 2:1 MMR with distances of about $a_\mathrm{b} = 20.6 \pm 1.2$ au and $a_\mathrm{c} = 34.5 \pm 2$ au (Keppler et al. 2018; Haffert et al. 2019). The inner planet is believed to be more massive than the outer one while their mass estimates are still uncertain at $M_\mathrm{b} = 5{-}14\,M_\mathrm{Jup}$ (Keppler et al. 2018) and $M_\mathrm{c} = 4{-}12\,M_\mathrm{Jup}$ (Haffert et al. 2019). These masses were estimated by comparing photometry of the sources to synthetic colours from planet evolution models.

Recently, Bae et al. (2019) showed that ALMA dust continuum observations at 890 μm can be convincingly reproduced by a pair of outward migrating planets. These latter authors performed 2D locally isothermal hydrodynamical simulations with a temperature profile obtained from radiative transfer calculations and using a stellar mass of $0.85\,M_\odot$ and two planets close to 2:1 MMR with masses of $M_\mathrm{b} = 10\,M_\mathrm{Jup}$ and $M_\mathrm{c} = 2.5\,M_\mathrm{Jup}$. They found the system to be stable for 1 Myr while smoothly migrating outward.

We ran additional simulations to model PDS 70 in order to test whether migration jumps could occur in that system. The PDS 70 models differ only slightly from our standard M9-3 setup, that is, the stellar mass is lowered to $M_* = 0.76\,M_\odot$. One PDS 70 simulation uses the locally isothermal equation of state (PDS70 ISO), while a second and third one use the ideal equation of state with irradiation from the star, like the IRR model above, with stellar luminosity $L_* = 0.35 \pm 0.09\,L_\odot$ (Müller et al. 2018). The first two models use the standard $\Sigma(r)$ profile (PDS70 ISO, PDS70 IRR) and the last one has a five-times-smaller Σ (PDS70 IRR M/5). All three models were integrated for 100 kr and are included in Table 1. Our models have a higher surface density compared to the ones in Bae et al. (2019). At a distance of 40 au this amounts to $\Sigma = 11.6\,\mathrm{g\,cm^{-2}}$ and $\Sigma = 2.4\,\mathrm{g\,cm^{-2}}$ (PDS 70 IRR M/5) in our models compared to their $\Sigma = 1\,\mathrm{g\,cm^{-2}}$.

5.1. Dynamical results

Figure 11 shows the dynamical outcome of the PDS 70 models. The model with a lighter disc (PDS70 IRR M/5) shows no special events. The inner planet migrates outward very slowly while the outer planet migrates inward until the system is locked into 2:1 MMR around $t \approx 80$ kyr (54 kyr after planet release). The system then migrates slowly outward together, maintaining the 2:1 resonance. The inner planet moves less than 0.5 au over the remaining 20 kyr.

Both models with high Σ show one migration jump until the end of the simulation at 100 kyr. The outer planet first migrates inward for approximately 10 kyr until the planets lock in 2:1 MMR. Rapid outward migration then starts in both cases leading up to a migration jump 30 kyr later.

In the PDS70 ISO case, the outer planet travels 10 au during that time and a migration jump takes it out to nearly 70 au with a period commensurability of $P_\mathrm{out}/P_\mathrm{in} \approx 4$. During the 16 kyr duration of the migration jump, the inner planet travels out by 5 au, because the negative torque contribution from the outside is missing. Due to the fast outward migration of the inner planet, when the outer planet migrates back in from the jump, the location of the 2:1 MMR is much further out. When the system goes back into 2:1 MMR, the outer planet is at 60 au from which point outward migration continues.

The sibling simulation with a more realistic equation of state and irradiation from the star (PDS70 IRR) shows similar, though less extreme effects. The outer planet travels out by 4 au following the point at which the planets become locked into resonance 30 kyr before the migration jump is about to happen. The smaller migration jump moves the outer planet further out by 6–46 au, where it has a period commensurability of $P_\mathrm{out}/P_\mathrm{in} \approx 2.75$. Again, the migration jump takes around 16 kyr, but the inner planet only migrates approximately 1 au during that time. Thus the location of 2:1 MMR for the outer planet is further in, at 44 au, to where it migrates back over a time-span of 6 kyr (instead of jumping back) until it locks into 2:1 MMR again. The different stopping location of the jump between models PDS70 and PDS70 IRR does not seem to stem from a difference in aspect ratio. Indeed, the aspect ratio in model PDS70 IRR is nearly identical to the one in model IRR, which is displayed in Fig. B.2, and is close to 0.05 around 40 au, exactly as in the locally isothermal model.

Along with the migration jumps, both models with a higher surface density show the formation of a vortex outside the gap already when the planets lock into 2:1 MMR. In the PDS70 IRR model, the vortex survives the small migration jump and lives on until the end of the simulation. In the PDS70 ISO model, it lives until the migration jump when it is disrupted by the outer planet and does not form again during the simulation time.

5.2. Synthetic images

Similarly to the model outcomes presented in Sects. 4.1 and 4.2, the outcomes of the PDS 70 models are post-processed in order to allow a comparison to the observed system. A modification of the procedure was made regarding the temperature and radius of the central star which have been set to 3972 K and 1.26 $R_\odot$, respectively (Keppler et al. 2018). The mass of the inner disc was reduced by a factor of 10^{-2} instead of 10^{-5} to keep some emission from the inner disc which can be seen in the observation (Keppler et al. 2019). We additionally apply an inclination angle of 51.7 degrees and a position angle of 156.7 degrees.

Figure 12 shows the synthetic observations of the model PDS70 IRR (panels b and d) and the model with lower disc mass PDS70 IRR M/5 (panels a and c), where the synthetic observations are calculated using two different ALMA antenna configurations. The first configuration (panels a and b) is unchanged from the one in Sect. 4.2. The second configuration (panels c and d) only uses the smaller `alma.cycle5.5` antenna configuration which results in a larger beam size.

Because the inner disc is more massive in gas, our assumption of a gas to dust ratio of 100 results in a very bright inner disc for higher disc masses. For each configuration, the colour scale is chosen such that its maximum value is the maximum intensity from the low-disc-mass models (panels a and c). This is done to make the outer parts of the disc visible in both models on the same colour scale.

The low-mass disc at high resolution (panel a) shows a hole in the inner disc. This is due to the inner hole of the computational domain. In the high-disc-mass case (panel b) this is no

longer visible due to the selection of the maximum value for the colour scale. For the smaller ALMA configuration with larger beam size (panels c and d), the hole is simply smeared out.

There is a clear difference between the model PDS70 IRR M/5 with lower disc mass and smooth outward migration (panels a and c) and model PDS70 IRR with higher disc mass and a migration jump (panels b and d). The low-disc-mass model (panels a and c) qualitatively reproduces the dust continuum observations presented in Keppler et al. (2019) showing the dust ring at a large distance from the star and a clearly visible and wide gap. Here, the location of the dust ring is closer in compared to the observations.

For a higher disc mass, the ring becomes azimuthally asymmetric with the right side being pronounced due to the existence of a vortex. At lower resolution (panel d), only the brighter right side is visible. At higher resolution (panel b), additional substructure is visible in the disc; for example the spur feature is visible to the right of the centre. Also clearly visible is an arc-like feature in the gap in the bottom left quadrant. The arc is located closer to the centre of the gap and emerges because the spiral arm of the inner planet is enhanced in density at that point in time. During the previous orbits, the outer planet came close to the outer gap edge on its eccentric orbit which results in a higher mass flow across its orbit. This higher mass flow across the orbit of the outer planet subsequently leads to higher densities in the spiral arm of the inner planet. Therefore, the arc is a result of the dynamic nature of the system with its high eccentricities.

6. Discussion

In this section, we discuss the implications of our findings, put them into context, and discuss their limitations. Results are discussed in reverse chronological order starting with our PDS 70 models (Sect. 6.1) and followed by the synthetic observations (Sect. 6.2), their implications (Sect. 6.3), and migration jumps (Sect. 6.4). We then go on to discuss simulation aspects such as the role of the inner boundary condition (Sect. 6.5) and choices concerning the equation of state and self-gravity (Sect. 6.6). We conclude by discussing the implications of our findings for transition discs (Sect. 6.7) and directly imaged systems of planets at large distances from their host stars (Sect. 6.8).

6.1. PDS 70

Our synthetic observations of the PDS 70 system show a dust ring at slightly smaller radii compared to Keppler et al. (2019). If we had simulated the system for a longer time, the pair of planets would have migrated further out also pushing the location of the ring further out. This way the synthetic models could be fine-tuned to match the actual observations.

In the case of PDS 70, our results suggest that no migration jump is happening in the system at this moment in time. This is likely due to the disc mass being lower than needed for migration jumps to happen, as the comparison between models PDS70 IRR and PDS70 IRR M/5 shows. Following this line of thought, our results might be used to put an upper limit on the disc mass. The disc mass must be lower than the one in model PDS70 IRR, $M_{\rm disc} = 0.048\,M_\odot$, at the time when the migration jump happens. We note that for simulations, the disc mass depends on the extent of the domain and the numbers quoted here refer to a disc with the inner and outer radius of our models, $r_{\rm in} = 2.08$ au and $r_{\rm out} = 208$ au. Scaled with a power-law profile as in Eq. (1), this corresponds to a surface density of $\Sigma = 8.24\,{\rm g\,cm^{-2}}$ at 40 au which is in agreement with the $\Sigma \approx 1\,{\rm g\,cm^{-2}}$ at 40 au which has been used in models of PDS70 before (Keppler et al. 2018, 2019). Another upper bound could be obtained by verifying the non-existence of features due to gravitational instability such as fragmentation which would require even more massive discs. Our threshold is lower than this self-gravity-induced upper bound because our discs have a Σ which is lower than the value required for fragmentation. The Toomre Q parameter is larger than 1 at any location and time. The upper bound could likely be improved by performing a parameter study which is out of the reach of this work.

Given the age of PDS 70, namely 5.4 ± 1.0 Myr, it cannot be ruled out that a migration jump happened at earlier times, and that the system relaxed back into a quieter state as the disc dispersed due to effects like photoevaporation or magnetically driven disc winds (Rodenkirch et al. 2020). Long-term simulations including disc dispersal effects would be required to answer this question.

In our synthetic images, we also observe the spur at the outer gap edge reported by Keppler et al. (2018, 2019) which has already been reproduced using a similar model to ours (Bae et al. 2019). Such a feature also appeared in our generic models (see Fig. 10 panels b, e, and f), suggesting that this kind of feature can generally appear for an outward migrating pair of planets.

6.2. Synthetic observations and dust treatment

In Sect. 4.2, we model dust emission by assuming a uniform dust-to-gas mass ratio of 10^{-2}. Thus, we use gas dynamics as a proxy for dust dynamics. As a result, effects like dust drift, dust size filtration, and dust diffusion (Weber et al. 2018), which are probably at play in a protoplanetary disc, are not considered. The inclusion of a proper dust treatment might therefore change the appearance of some features in the synthetic images.

Nonetheless, similar features have been observed to also emerge when dust is handled properly. A dust ring growing in size because of outward migration of a pair of massive planets was reported by Marzari et al. (2019) for a close-in (inside 10 au) Jupiter–Saturn pair in a massive disc ($\Sigma_0(10\,{\rm au}) = 75\,{\rm g\,cm^{-2}}$ versus $\Sigma_0(10\,{\rm au}) \approx 46\,{\rm g\,cm^{-2}}$ here) and by Bae et al. (2019) for a model of the PDS 70 system with 10 and 2.5 $M_{\rm Jup}$ planets in a lighter disc ($\Sigma_0(10\,{\rm au}) \approx 9\,{\rm g\,cm^{-2}}$). The latter study also found the PDS 70 spur feature (Keppler et al. 2019; Bae et al. 2019), supporting the idea that similar features also appear with proper dust treatment. However, to judge how dust dynamics influences the features found in our synthetic observations, simulations including dust treatment are needed. We plan to investigate this in a follow-up study.

We want to highlight that multiple distinct observational features can be created by the same planetary system at different points in time if the system exhibits sufficiently strong dynamic effects such as a migration jump. Except for the choice of planet mass ratio, all presented observational features emerged for a disc with standard parameters without the need of fine-tuning.

6.3. Observational signposts for dynamic effects

For our PDS 70 models (see Sect. 5), we observed non-axisymmetric features in the higher disc mass model. The higher surface density caused faster outward migration and thus a higher mass flow through the common gap. The first effect was the appearance of a vortex, visible as asymmetry in the intensity distribution (Figs. 12 b and d). The second effect was an arc-like feature in the gap region caused by an enhancement of density in

the spiral arm of the inner planet. Together with the spur feature discussed above, if detected in real observations, these features might hint at outward migration and enhanced mass flow through the gap region.

Contrasting the smooth synthetic observations of our low-mass PDS 70 model, or the model by Bae et al. (2019) in which the planetary system undergoes smooth and slow outward migration, with our synthetic observations in Fig. 10, we can identify which features could be "signposts" for strong dynamical effects like migration jumps. We can identify these potential signposts as very eccentric holes or gaps, vortices, arc-shaped voids, mass accumulations in Lagrangian points, and visible spiral arms. The latter two might be the easiest to discover in real observations because they are located in the gap region where the surrounding emission is weak. Indeed, similar features such as an arc inside a gap have already been observed, for example in the disc of HD 163296 (Isella et al. 2018). Fast outward migration of a single planet might lead to comparable observational signatures such as arc-shaped voids behind the planet (Pepliński et al. 2008). Therefore, only the combination of one of the signposts listed above with a large gap will provide a strong indication for a migration jump.

Our simulations show that a higher disc mass facilitates stronger planetary system dynamics. Thus, by pointing toward strong dynamic effects, these signposts might indirectly hint at a high gas mass.

6.4. Migration jumps

Migration jumps are introduced in Sect. 3.2. To our knowledge, we are the first to name, describe, and analyse this dynamical process in detail. We observed migration jumps for different resolutions (Appendix A), for different choices of equation of state and treatments of the energy equation (Sect. 5 and Appendix B), for different domain sizes (models L and L M/2), independent of accretion onto the planet (Sect. 3.5), for different choices of inner boundary conditions (models VB* and WD*), and for models with and without self-gravity (models SG and SG IRR). These tests reinforce our confidence that migration jumps are indeed a physical effect.

There is at least one example in the literature where migration jumps appeared in simulations. Figure 1 of Chametla et al. (2020) shows two migration jumps in their model 7b in which a Jupiter–Saturn pair (mass ratio 3:1) is migrating outwards in 3:2 MMR and experiences two small migration jumps between 5 and 8 au. This indicates that migration jumps can also happen for other types of MMRs, at smaller radii, and for planet masses down to a Jupiter–Saturn-sized pair. A natural question to ask refers to why migration jumps were not found before, in studies like Marzari et al. (2019) or Bae et al. (2019), for example.

For the case of Marzari et al. (2019), we repeated similar simulations with different boundary conditions and the domain size from 0.5 to 15 au. We found smooth outward migration at similar rates. In these simulations, the surface density, Σ, is about twice as high as in our model M9-3. The non-appearance of a migration jump is likely due to the non-existence of a vortex in these simulations. This is probably due to the smaller outer radius and the wave damping zone close to the outer boundary which prevents the formation of a vortex at the location where we would expect it by scaling down the location from our simulations. This suggests that vortices are important for the mechanism of migration jumps.

In the case of Bae et al. (2019), the non-appearance of migration jumps is very likely due to the lower value of Σ, which is comparable to that of our model M9-3 M/10 which also does not show a migration jump.

Migration jumps could have profound effects for planetary systems. During the jump, dust can be gravitationally scattered by the planets which might be a way to redistribute dust trapped in a pressure maximum and possibly even dust trapped in the vortex. We plan to perform simulations with embedded dust to explore these hypotheses.

A jump might also have significant effects for the accretion process as shown in Sect. 3.5. Mass accretion rates onto the planets can be enhanced by two orders of magnitude by moving the outer planet to regions outside the planet gap where the surface density is high. This in turn also increases the mass accretion onto the inner planet. Together this might provide a mechanism by which massive planets can accrete mass more efficiently by tapping into mass reservoirs far away from their initial orbit.

In our view, migration jumps are a composite phenomenon in which resonant outward migration via the Masset & Snellgrove (2001) mechanism, the interaction of a planet with a vortex, and the subsequently triggered type III rapid outward migration are combined to give rise to an emerging effect.

6.5. Planet ejections and internal boundary condition

Planet ejections occurred in models where an inner boundary different from outflow was used in combination with a disc centred in the centre of mass of the N-body system due to a numerical instability (Sect. 3.6). Our results suggest that if a viscous boundary, a reflective boundary, or wave-damping zones are used, the hydrodynamical simulation should be centred on the primary star. It might also be possible to adjust the boundary condition to follow the moving star in the other case, but we did not implement this more complicated feature. Such a dependence of the dynamical behaviour of planets on the treatment of the inner boundary, which lies well inside the actual realm of the planets, has been observed in other simulations of embedded planets, for example for the system GJ 876 (Crida et al. 2008; Cimerman et al. 2018). The outflow boundary condition seems to give more freedom to the inner disc by allowing a moving inner disc edge. Indeed, this boundary condition is also a good choice to simulate eccentric discs around binary stars (Thun & Kley 2018).

6.6. Equation of state and self-gravity

Recent studies have shown that radiative effects can play an important role for the spiral arm and gap structure in the case of low-mass planets where radiative effects cause significant changes compared to a purely locally isothermal assumption (Ziampras et al. 2020). In our case, we see a qualitatively similar behaviour for locally isothermal simulations and simulations considering radiative effects (see Appendix B). However, the size of migration jumps and the rate of outward migration depend on the inclusion of radiative effects in our PDS 70 models (Sect. 11). The appearance of migration jumps for both radiative and locally isothermal models hints at the dynamic nature of the process. Migration jumps are likely dominated by resonant N-body interactions pumping eccentricities and the interaction with the vortex formed outside the gap.

For reasons of simplicity and runtime, we neglected self-gravity in most of our simulations. Judging by the value of the Toomre Q parameter which stays above 1 at all times, the disc is not prone to fragmentation. However, other processes might be slightly altered when self-gravity is taken into account. Firstly,

self-gravity might play a role in the migration of massive planets as is the case for low-mass planets (Ataiee & Kley 2020). Secondly, in our simulations, the occurrence of migration jumps coincides with the existence of a vortex. When self-gravity is considered, vortices will weaken and can stretch out even for low-mass discs as long as the Toomre Q parameter is lower than 50 or $hQ \lesssim \frac{\pi}{2}$ (Lovelace & Hohlfeld 2013; Regály & Vorobyov 2017; Zhu & Baruteau 2016). Both conditions are fulfilled in the standard M9-3 model with $Q \approx 6$ and $hQ \approx 0.3$ for the initial profile at the location of the vortex.

Models SG and SG IRR with self-gravity enabled indeed show that there is no disc fragmentation, but stretching of the vortex. Hence, our finding that migration jumps still occur with self-gravity considered is one more indication that they are indeed a physical phenomenon.

6.7. Mass accretion and Type II transition discs

In all our models, mass accretion onto the star, as measured by the mass flow rate through the inner boundary, was higher (10^{-8} to $10^{-7}\,M_\odot\,\mathrm{yr}^{-1}$) than the viscous mass accretion rate of the unperturbed disc ($<10^{-8}\,M_\odot\,\mathrm{yr}^{-1}$). The inner disc was building up mass over time in these models, showing higher surface densities compared to the initial profile. We suspect that mass transfer through the gap is enhanced by the "shoveling" mechanism (Sect. 3.5). As the outer planet comes close to the outer gap edge at apastron on its eccentric orbit, it scatters mass inwards. Additionally, outward migration must necessarily enhance mass flow through the gap. When the planets migrate outward, they gain angular momentum. Because angular momentum is conserved, the angular momentum gained by the planets has to be extracted from the gas requiring that some gas has to move from outside the gap (outside the planetary orbits) to inside the gap (inside the planetary orbits) to supply the angular momentum. This mechanism of shovelling matter from outside in is after all the basic mechanism behind the Masset–Snellgrove mechanism of outward migration, as the material crossing the joint gap is collected in the inner disc which generates the positive torque to drive the planets outward (Masset & Snellgrove 2001). Our models serve to quantify this process in more detail.

A particularly clear example of this mechanism is model L for which we reported the dependency of mass accretion through the gap on the direction of migration in Sect. 3.5. There, mass flow through the gap is present during both in- and outward migration but is strongly enhanced for the outward case. This means that the common gap formed by the planets is not an impermeable barrier for mass accretion. Model L illustrates that mass flow through the gap is possible for both directions of migration and that it can be enhanced by over one order of magnitude in the case of outward migration.

The large gap in dust emission reported in Sects. 4 and 5 (see also Marzari et al. 2019; Bae et al. 2019) together with an enhanced stellar mass accretion make outwardly migrating pairs of planets prime candidates for a consistent explanation of Type II transition discs (Owen & Clarke 2012) which feature large gaps or holes and high accretion rates at the same time.

6.8. Directly imaged planets at large distances

There are several examples of giant planets observed at large distances from their host star. At such large distances, in situ formation by gravitational instability is challenging (Zhu et al. 2012). Assuming they formed further in, it is still challenging to explain how they moved outwards over long distances, even though models based on the smooth outward resonant migration have been invoked to explain such systems (Pepliński et al. 2008; Crida et al. 2009; Kimmig et al. 2020). The advantage of our migration jumps is the very short timescale on which they occur and the large radial range covered.

PDS 70 is one example, with the outer planet located at 35.5 ± 2 au (Haffert et al. 2019), for which outward migration seems a promising scenario, as a comparison with our simulations shows. In our simulations, the outer planet reaches distances from its host star of up to 133 au after 226 kyr, providing an explanation of how planets can reach such large distances from their host after being formed further inside. The actual process is likely a balance between speed of migration and dispersal of the disc, allowing for a range of final locations.

HR 8799 is another famous example of a directly observed planetary system that features a chain of four planets which might be in 8:4:2:1 resonance (Marois et al. 2010; Goździewski & Migaszewski 2014). There, the outer planet HR 8799 b is located around 70 au (Wang et al. 2018). It is unclear whether or not outward migration in resonance can also produce such an intricate system, yet formation of the planets closer to the star followed by outward migration should be considered as a formation scenario. More extended simulations with more planets are needed to elucidate this problem.

7. Summary

We studied the dynamical evolution of a system of two massive planets (in a mass range of 3–9 M_{Jup}) embedded in a protoplanetary disc using two-dimensional, viscous hydrodynamical simulations carried out with the FARGO code. The planets were treated as smoothed point masses that in some simulations were allowed to accrete mass which was added to their dynamical mass. For the disc, we assumed either a locally isothermal equation or a more realistic situation where we solved for an energy equation that included viscous heating, radiative cooling, and stellar irradiation.

Concerning the migration of the planets, we found two different basic behaviours depending on the mass order of the two planets. In the case of a more massive outer planet, the planets migrate inward engaged in 2:1 MMR. For a more massive inner planet with mass ratios of 2:1 or 3:1, we find outward migration of both planets, again engaged in a 2:1 MMR. As found before, this resonant migration process, originally described by Masset & Snellgrove (2001) for the Jupiter–Saturn system, can lead to a resonant outward migration in 2:1 MMR in the case of massive planets (Pepliński et al. 2008; Crida et al. 2009).

The new feature that we discovered is an occurrence of what we call a "migration jump". A migration jump is a composite phenomenon in which outward migration in resonance and interaction with a vortex cause conditions such that type III rapid outward migration is triggered. The outer (lighter) planet covers a large radial distance on a very short timescale, for example from 40 to 72 au in only 5000 yr; see Fig. 4. The phase of outward migration is usually followed by a phase of inward migration back into the initial resonant configuration. Migration jumps are a generic, robust feature of our models. They occur for different equations of state and accretion rates onto the planet, with or without self-gravity, and for different resolutions, as long as the surface density of the disc is sufficiently high.

In addition to the dynamical behaviour of the embedded planets, we monitored the mass accretion onto the central star, as this is a standard observable feature in transition discs (Owen 2016). For our models we find that during the smooth outward

migration phase of the resonantly locked planet pair the accretion rate is significantly higher than in the situation when the outer planet has a higher mass and the planets migrate inward. During the outward migration phases the planetary system gains angular momentum which is lost by the disc. As a consequence, the disc material moves inwards and is "shovelled" towards the star by the pair of planets. This increases the mass flow rate onto the star by more than one order of magnitude, much higher than in the regular phases of smooth inward migration. This effect can be even more enhanced during the short phase of a migration jump; see Figs. 7 and 9. A combination of outward migration and high stellar mass accretion, as found in our models, could serve as a consistent explanation for the phenomenon of Type II transition discs with large inner holes and nevertheless high stellar accretion rates (Owen & Clarke 2012).

Using the outcome of our hydrodynamical models, we calculated synthetic images that show a surprising variety of non-axisymmetric features appearing over time in a single system; see Fig. 10. Depending on their dynamical state, a bright ring just beyond the planets was seen, followed by vortex structures, and then additional structures in the main gap created by the planets. These initial images were based on a constant dust-to-gas ratio and for more realistic cases the dust dynamics will have to be followed simultaneously to the gas dynamics. Nevertheless, the initial models provide insight into the possible observational effects generated by the planets. In our study, we also included models with parameters reminiscent of the system PDS 70, which contains two massive embedded planets. From our synthetic images for this system we may conclude that it does not currently undergo a migration jump but might very well be in a phase of outward migration, compatible with Bae et al. (2019). The non-occurrence of the signposts of a migration jump indicates a disc mass lower than $M_{\rm disc} < 0.048\,M_{\odot}$ for a disc extending out to 200 au which serves an independent upper bound compatible with radiative transfer models reproducing the observations of the system (Keppler et al. 2018, 2019). A more detailed comparison between simulations and observations will have to consider dust embedded in the disc. From our models we can finally conclude that Type II transition discs with large inner holes but significant stellar accretion are indeed signposts for highly dynamic embedded planetary systems.

Acknowledgements. All authors acknowledge funding from the DFG research group FOR 2634 "'Planet Formation Witnesses and Probes: Transition Disks" under grant DU 414/22-1 and KL 650/29-1, 650/30-1. The authors acknowledge support by the High Performance and Cloud Computing Group at the Zentrum für Datenverarbeitung of the University of Tübingen, the state of Baden-Württemberg through bwHPC and the German Research Foundation (DFG) through grant INST 37/935-1 FUGG. Plots in this paper were made with the Python library `matplotlib` (Hunter 2007).

References

Alexander, R. D., Clarke, C. J., & Pringle, J. E. 2006, MNRAS, 369, 216
Andrews, S. M., Huang, J., Pérez, L. M., et al. 2018, ApJ, 869, L41
Ataiee, S., & Kley, W. 2020, A&A, 635, A204
Ataiee, S., Pinilla, P., Zsom, A., et al. 2013, A&A, 553, L3
Bae, J., Zhu, Z., Baruteau, C., et al. 2019, ApJ, 884, L41
Baruteau, C. 2008, Theses, Observatoire de Paris
Birnstiel, T., Dullemond, C. P., Zhu, Z., et al. 2018, ApJ, 869, L45
Calvet, N., D'Alessio, P., Hartmann, L., et al. 2002, ApJ, 568, 1008
Chametla, R. O., D'Angelo, G., Reyes-Ruiz, M., & Sánchez-Salcedo, F. J. 2020, MNRAS, 492, 6007
Cimerman, N. P., Kley, W., & Kuiper, R. 2018, A&A, 618, A169
Crida, A., Morbidelli, A., & Masset, F. 2007, A&A, 461, 1173
Crida, A., Sándor, Z., & Kley, W. 2008, A&A, 483, 325
Crida, A., Masset, F., & Morbidelli, A. 2009, ApJ, 705, L148
Cumming, A., Butler, R. P., Marcy, G. W., et al. 2008, PASP, 120, 531
D'Alessio, P., Hartmann, L., Calvet, N., et al. 2005, ApJ, 621, 461
de Juan Ovelar, M., Min, M., Dominik, C., et al. 2013, A&A, 560, A111
de Val-Borro, M., Edgar, R. G., Artymowicz, P., et al. 2006, MNRAS, 370, 529
Dodson-Robinson, S. E., & Salyk, C. 2011, ApJ, 738, 131
Dong, R., & Dawson, R. 2016, ApJ, 825, 77
Dubrulle, B., Morfill, G., & Sterzik, M. 1995, Icarus, 114, 237
Dullemond, C. P., Juhasz, A., Pohl, A., et al. 2012, Astrophysics Source Code Library [record ascl:1202.015]
Dürmann, C., & Kley, W. 2017, A&A, 598, A80
Espaillat, C., Muzerolle, J., Najita, J., et al. 2014, Protostars and Planets VI, eds. H. Beuther, R. S. Klessen, C. P. Dullemond, & T. Henning (Tucson, AZ: University of Arizona Press), 497
Forgács-Dajka, E., Sándor, Z., & Érdi, B. 2018, MNRAS, 477, 3383
Gaia Collaboration (Brown, A. G. A., et al.) 2018, A&A, 616, A1
Goździewski, K., & Migaszewski, C. 2014, MNRAS, 440, 3140
Haffert, S. Y., Bohn, A. J., de Boer, J., et al. 2019, Nat. Astron., 3, 749
Hayashi, C. 1981, Prog. Theor. Phys. Suppl., 70, 35
Hendler, N. P., Pinilla, P., Pascucci, I., et al. 2018, MNRAS, 475, L62
Ho, P. 2016, Nature, 530, 169
Huélamo, N., Lacour, S., Tuthill, P., et al. 2011, A&A, 528, L7
Hunter, J. D. 2007, Comput. Sci. Eng., 9, 90
Isella, A., Huang, J., Andrews, S. M., et al. 2018, ApJ, 869, L49
Keppler, M., Benisty, M., Müller, A., et al. 2018, A&A, 617, A44
Keppler, M., Teague, R., Bae, J., et al. 2019, A&A, 625, A118
Kimmig, C. N., Dullemond, C. P., & Kley, W. 2020, A&A, 633, A4
Koller, J., Li, H., & Lin, D. N. C. 2003, ApJ, 596, L91
Lovelace, R. V. E., & Hohlfeld, R. G. 2013, MNRAS, 429, 529
Manara, C. F., Testi, L., Natta, A., et al. 2014, A&A, 568, A18
Marois, C., Zuckerman, B., Konopacky, Q. M., Macintosh, B., & Barman, T. 2010, Nature, 468, 1080
Marzari, F., Baruteau, C., & Scholl, H. 2010, A&A, 514, L4
Marzari, F., D'Angelo, G., & Picogna, G. 2019, AJ, 157, 45
Masset, F. 2000, A&AS, 141, 165
Masset, F., & Snellgrove, M. 2001, MNRAS, 320, L55
McMullin, J. P., Waters, B., Schiebel, D., Young, W., & Golap, K. 2007, ASP Conf. Ser., 376, 127
Muley, D., Fung, J., & van der Marel, N. 2019, ApJ, 879, L2
Müller, T. W. A., & Kley, W. 2012, A&A, 539, A18
Müller, T. W. A., & Kley, W. 2013, A&A, 560, A40
Müller, T. W. A., Kley, W., & Meru, F. 2012, A&A, 541, A123
Müller, A., Keppler, M., Henning, T., et al. 2018, A&A, 617, L2
Owen, J. E. 2016, PASA, 33, e005
Owen, J. E., & Clarke, C. J. 2012, MNRAS, 426, L96
Paardekooper, S. J., & Mellema, G. 2004, A&A, 425, L9
Pepliński, A., Artymowicz, P., & Mellema, G. 2008, MNRAS, 387, 1063
Pinilla, P., de Juan Ovelar, M., Ataiee, S., et al. 2015, A&A, 573, A9
Regály, Z., & Vorobyov, E. 2017, MNRAS, 471, 2204
Reggiani, M., Christiaens, V., Absil, O., et al. 2018, A&A, 611, A74
Rein, H., & Liu, S. F. 2012, A&A, 537, A128
Rice, W. K. M., Armitage, P. J., Wood, K., & Lodato, G. 2006, MNRAS, 373, 1619
Rodenkirch, P. J., Klahr, H., Fendt, C., & Dullemond, C. P. 2020, A&A, 633, A21
Sándor, Z., Kley, W., & Klagyivik, P. 2007, A&A, 472, 981
Shakura, N. I., & Sunyaev, R. A. 1973, A&A, 500, 33
Shu, F. H., Johnstone, D., & Hollenbach, D. 1993, Icarus, 106, 92
Thun, D., & Kley, W. 2018, A&A, 616, A47
van der Marel, N., van Dishoeck, E. F., Bruderer, S., Pérez, L., & Isella, A. 2015, A&A, 579, A106
van der Marel, N., van Dishoeck, E. F., Bruderer, S., et al. 2016, A&A, 585, A58
Varnière, P., Blackman, E. G., Frank, A., & Quillen, A. C. 2006, ApJ, 640, 1110
Wang, J. J., Graham, J. R., Dawson, R., et al. 2018, AJ, 156, 192
Ward, W. R. 1997, Icarus, 126, 261
Weber, P., Benítez-Llambay, P., Gressel, O., Krapp, L., & Pessah, M. E. 2018, ApJ, 854, 153
Zhu, Z., & Baruteau, C. 2016, MNRAS, 458, 3918
Zhu, Z., Nelson, R. P., Hartmann, L., Espaillat, C., & Calvet, N. 2011, ApJ, 729, 47
Zhu, Z., Hartmann, L., Nelson, R. P., & Gammie, C. F. 2012, ApJ, 746, 110
Ziampras, A., Ataiee, S., Kley, W., Dullemond, C. P., & Baruteau, C. 2020, A&A, 633, A29

Appendix A: Convergence with resolution

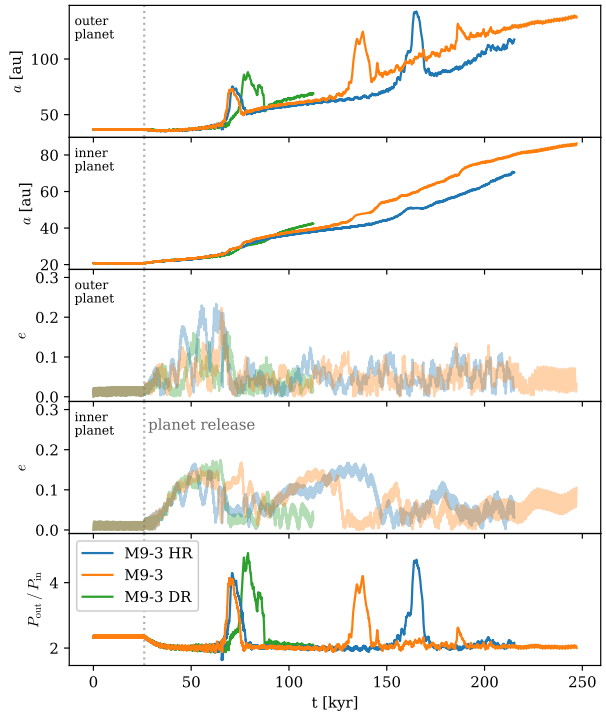

Fig. A.1. Migration history of models with standard, double (DR), and half (HR) 2D resolution to test convergence with spacial resolution. The panels show, *from top to bottom*, evolution of the semi-major axis of the outer planet, same for the inner planet, their eccentricities (middle and following panel), and their period ratio.

To test convergence of the simulations with respect to spatial resolution, we ran a model with the 2D resolution lowered and increased by a factor of two, i.e. in each direction the resolution is changed by a factor of $\sqrt{2}$. Model M9-3 HR has $N_r \times N_\phi = (426, 580)$ and model M9-3 DR has $N_r \times N_\phi = 851 \times 1161$ cells. They are otherwise identical to the M9-3 model which has $N_r \times N_\phi = 602 \times 821$ cells.

A comparison of the planet migration for the three cases is shown in Fig. A.1. The overall qualitative behaviour is the same; the most noticeable difference is the time at which the migration jump occurs. For the first jump, this is only slightly different. Since the changes are small, we conclude that the simulations are converged with respect to resolution. In fact, the lower resolution is already sufficient to resolve the dynamics.

Appendix B: Dependence on equation of state

Using the locally isothermal equation of state is a valid approximation in the case of low optical thickness and negligible viscous heating compared to stellar irradiation. For the outer disc region, in which the planets in our simulations are located, this should be well justified. To test the assumption, we ran additional simulations where the energy equation is solved and viscous heating and cooling from the disc surfaces are included as in Müller & Kley (2012), and irradiation from the star is treated analogously

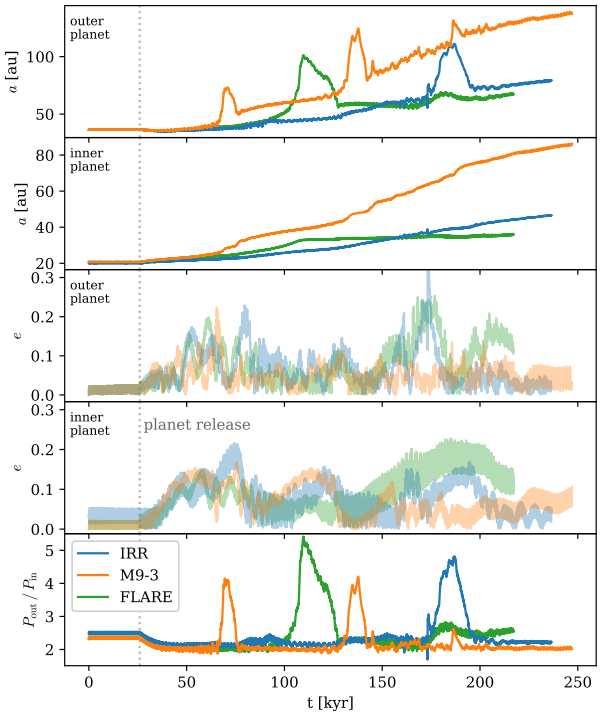

Fig. B.1. Comparison of the migration history of the standard M9-3 model and the more realistic and radiative model IRR and the model FLARE. Panels as in Fig. A.1.

to Ziampras et al. (2020) with their choices of parameters. Additionally, we repeated the standard M9-3 with a radial temperature profile that is set by stellar irradiation, which resembles the temperature profile in model IRR very well resulting in a flared disc (see Fig. B.2 below).

Figure B.1 shows a comparison of the migration history between the reference model M9-3 and the irradiation model IRR. Although the outward migration happens with a slower speed, a migration jump still occurs. Model IRR shows a first event at around 80 kyr where the eccentricity of the outer planet suddenly drops from 0.2 down to small values, but only jumps about 5 au. A second event occurs around 170 kyr where the outer planet jumps 45 au, comparable to the migration jumps observed in the M9-3 run. Model FLARE, which employs a locally isothermal equation of state, first follows the IRR model but instead of the failed small jump at 80 kyr it undergoes a full large jump. The comparison shows that, although details such as the migration rate depend on the aspect ratio profile, migration jumps appear also for flared discs.

Figure B.2 shows the temperature and aspect ratio profiles for the three models. Around the region where the planets are located, the aspect ratios are comparable with values around 0.05. However, at the location where the planet jumps happens, h has increased to ~0.07 for the IRR and FLARE models. This might explain the difference in amplitude and period ratios during the migration jump. Finally, as there are only small qualitative differences, we conclude that the locally isothermal assumption is justified in this case to capture the most important dynamics.

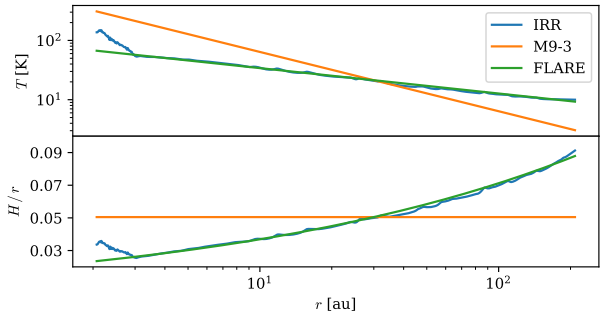

Fig. B.2. Temperature (*top*) and aspect ratio H/r (*bottom*) for the standard model M9-3, model IRR and model FLARE at 200 kyr.

Appendix C: Identification of the vortex

During the periods of resonant outward migration, a banana-shaped overdensity appears just outside the common gap. In this section, we analyse the snapshot in panel b of Fig. 5 of model M9-3 in more detail.

Figure C.1 shows the vortensity ω/Σ normalised by its value from the initial profile. The numerator is the vorticity, which is defined as the z-component of the curl of the velocity, $\omega = (\nabla \times \boldsymbol{v})_z$. The orbits of both planets are shown as a dotted green line and the locations of the planets are indicated by the green crosses. By dividing the current value of the vortensity by the initial one at each location, the dependence on the steepness of the initial density profile and the background vorticity of the

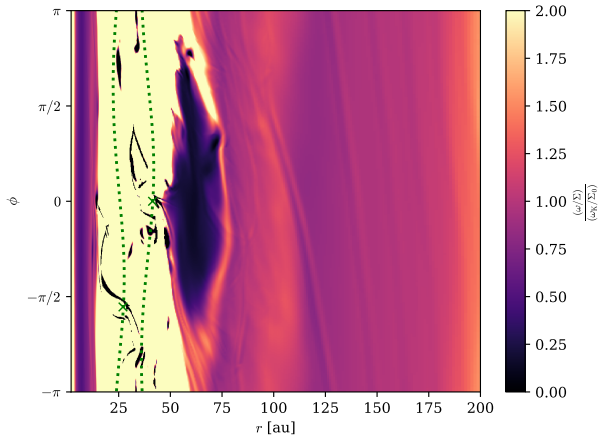

Fig. C.1. Vortensity normalized by the initial vortensity in $r-\phi$ coordinates for a ±100 au zoom-in to panel b of Fig. 5. The overdensity appears as a region of lower vortensity compared to its surroundings indicating that it is indeed a vortex. The orbits of the planets are shown as dotted green lines and the location of each planet is indicated by a small green cross symbol.

Keplerian disc are factored out. This results in a clear picture of what happens locally with the velocity field. A vortex in a disc appears as a region of lower vortensity as compared to its surroundings, due to its anticyclonic nature as seen in Fig. 6. This clearly identifies the overdensity at 59 au as a vortex.

A&A 656, A130 (2021)
https://doi.org/10.1051/0004-6361/202142105
© ESO 2021

Astronomy & Astrophysics

Survival of planet-induced vortices in 2D disks

Thomas Rometsch, Alexandros Ziampras, Wilhelm Kley, and William Béthune

Institut für Astronomie und Astrophysik, Universität Tübingen, Auf der Morgenstelle 10, 72076 Tübingen, Germany
e-mail: thomas.rometsch@uni-tuebingen.de, alexandros.ziampras@uni-tuebingen.de

Received 29 August 2021 / Accepted 29 September 2021

ABSTRACT

Context. Several observations of protoplanetary disks reveal non-axisymmetric features, which are often interpreted as vortices. Numerical modeling has repeatedly shown that gap-opening planets are capable of producing large and long-lasting vortices at their outer gap edge, making massive planets popular candidates as the source of such features.
Aims. We explore the lifetime of vortices generated by Jupiter-sized planets as a function of the thermal relaxation timescale, the level of turbulence, and the effect of disk self-gravity.
Methods. We conduct 2D numerical simulations using the hydrodynamics codes PLUTO and FARGO, scanning through several physical and numerical parameters. Vortex properties are automatically extracted from thousands of simulation snapshots.
Results. We find that vortices that spawn at the outer gap edge can survive for about 100–3000 planetary orbits, with the shortest lifetimes occurring for moderately efficient dissipation and cooling. However, we also observe a different regime of long-lasting vortices with lifetimes of at least 15 000 orbits for very low viscosity and very short thermal relaxation timescales. Disk self-gravity significantly shortens the lifetime of regular vortices but still allows long-lived ones to survive.
Conclusions. Our results suggest that the cooling timescale plays an important role in vortex formation and lifetime and that planet-generated vortices should be observable at large distances from the star for typical thermal relaxation timescales and low turbulence levels.

Key words. protoplanetary disks – planet-disk interactions – hydrodynamics – methods: numerical

1. Introduction

Planets are born and grow in accretion disks around young stars. This is supported by observations of protoplanets embedded in a disk of gas and dust captured during their growth phase (e.g., Keppler et al. 2018). A protoplanet interacts with the disk around it in every stage of its growth (Kley & Nelson 2012), for example via exchange of angular momentum. This results in the launching of spiral arms (Ogilvie & Lubow 2002); if the planet is massive enough, the opening of a gap; and, in some cases, the formation of multiple rings around the planet's orbit (Rafikov 2002). The number of spirals, gaps, and rings as well as their contrast scales with the planet mass, such that Jupiter-sized planets can have a strong impact on their environment in the right conditions, possibly resulting in multiple ring-like and nonaxisymmetric observable features (Zhang & Zhu 2020; Miranda & Rafikov 2020a). This makes the planet–disk interaction scenario a popular interpretation of such features in the numerous high-fidelity ALMA observations.

One promising scenario to explain observational asymmetries is the existence of vortices because they naturally accumulate dust at the pressure maxima in their center (see e.g., Marel et al. 2013; Bae et al. 2016; Pérez et al. 2018; Hammer et al. 2019; Barge & Sommeria 1996). Among the various ways to form vortices, the Rossby-wave instability (RWI, Lovelace et al. 1999) is particularly relevant in the vicinity of gaps. The RWI readily happens in 2D disks at the outer and inner edge of planet-opened gaps (Li et al. 2005; De Val-Borro et al. 2007). Additional mechanisms that could be relevant in this context are the subcritical baroclinic instability (SBI, Klahr & Bodenheimer 2003; Lesur & Papaloizou 2010) and the zombie-vortex instability (ZVI, Marcus et al. 2015, 2016). Vortices are then susceptible to viscous spreading as well as secondary instabilities such as the elliptical instability (Lesur & Papaloizou 2009), which cause vortex decay. The lifetime of vortices is therefore determined by a competition between vortex-forming and -decaying mechanisms.

Aside from possibly causing observable features in the disks, vortices can also affect planet migration in a stochastic fashion (Regály et al. 2013; Ataiee et al. 2014; McNally et al. 2019) and even cause temporary outward migration (Lega et al. 2021) for otherwise inwardly migrating planets. Understanding their formation pathways and lifetimes is therefore critical to the modeling of planet migration using global, low-viscosity simulations.

In previous numerical studies, vortex properties have been found to depend on various physical processes such as turbulent viscosity and disk self-gravity. Lower viscosity allows vortices to live longer (Godon & Livio 1999; De Val-Borro et al. 2007; Ataiee et al. 2013; Fu et al. 2014; Regály et al. 2017) whereas the inclusion of self-gravity tends to weaken vortices, shortening their lifespan (Lin & Papaloizou 2011; Zhu & Baruteau 2016; Regály & Vorobyov 2017; Pierens & Lin 2018).

In recent numerical studies, radiative effects have been discovered to have a significant impact on the gap-opening capabilities of planets and therefore the structure of the gaps themselves (Ziampras et al. 2020b; Miranda & Rafikov 2020b), affecting the development of the RWI and by extension vortices around their edge (Tarczay-Nehéz et al. 2020). The aim of the present study is to investigate the role of radiative effects for properties of vortices created by planets. More precisely, we explore how the thermal relaxation timescale of the gas affects the

lifetime of vortices created during the growth of Jupiter-sized planets.

The impact of thermal relaxation on vortex formation and lifetime was studied for nearly inviscid disks by Les & Lin (2015), and recently Fung & Ono (2021) ran 2D shearing box simulations of RWI-induced vortices. As their simulations did not include a planet, the RWI was triggered by an artificial density bump. These authors described a baroclinic effect that spins down vortices where the decay is fastest for thermal relaxation times of the order of a tenth of the vortex turnover time.

We ran a suite of global two-dimensional hydrodynamics simulations with an embedded Jupiter-sized planet – which naturally creates vortices in the disk – for different choices of turbulent viscosity and thermal relaxation timescales, among other physical parameters. The results of these simulations are then post-processed with our newly developed pipeline for the detection and characterization of vortices.

In Sect. 2 we describe our physical model and numerical setup. We present a typical life track of a vortex in our models in Sect. 3, report the dependence of vortex properties on physical parameters in Sect. 4, and present the case of long-lived vortices in Sect. 5. We discuss and comment on our findings in Sect. 6. Finally, Sect. 7 contains a summary of our main results and our conclusions.

2. Physics and numerics

In this section, we describe the physical and numerical framework that we used in our simulations. We justify the approximations in our model, explain in detail the initialization process, and list technical parameters such as our grid setup and parameter space.

2.1. Hydrodynamics

We consider a thin disk of neutral, ideal gas with adiabatic index $\gamma = 7/5$ and mean molecular weight $\mu = 2.353$ that is orbiting around a star with one solar mass $M_\star = M_\odot$. The two-dimensional, vertically integrated Navier-Stokes equations in a polar coordinate system $\{r, \phi\}$ read

$$\frac{\partial \Sigma}{\partial t} + \boldsymbol{u}\cdot\nabla\Sigma = -\Sigma\nabla\cdot\boldsymbol{u}, \tag{1a}$$

$$\Sigma\frac{\partial \boldsymbol{u}}{\partial t} + \Sigma(\boldsymbol{u}\cdot\nabla)\boldsymbol{u} = -\nabla p + \Sigma\boldsymbol{g} + \nabla\cdot\boldsymbol{\sigma}, \tag{1b}$$

$$\frac{\partial(\Sigma\varepsilon)}{\partial t} + \boldsymbol{u}\cdot\nabla(\Sigma\varepsilon) = -\gamma\Sigma\varepsilon\nabla\cdot\boldsymbol{u} + Q_{\rm visc} + Q_{\rm relax}, \tag{1c}$$

where $\boldsymbol{u} = (u_r, u_\phi)$ and ε are the velocity and specific internal energy of the gas evaluated at the midplane, and Σ is the surface density. The vertically integrated pressure p is defined through the ideal gas law $p = (\gamma - 1)\Sigma\varepsilon = R_{\rm g}\Sigma T/\mu$, with $R_{\rm g}$ being the gas constant and T the gas temperature. The isothermal sound speed of the gas is then given by $c_{\rm s,iso} = \sqrt{p/\Sigma} = \sqrt{R_{\rm g}T/\mu}$ and relates to the adiabatic sound speed $c_{\rm s}$ as $c_{\rm s,iso} = c_{\rm s}/\sqrt{\gamma}$. For a disk in Keplerian motion and vertical hydrostatic equilibrium, we can also write $c_{\rm s,iso} = H\Omega_{\rm K}$, where $\Omega_{\rm K} = \sqrt{GM_\star/r^3}$ is the Keplerian orbital frequency at radius r and H is the pressure scale height of the gas.

The viscous stress tensor $\boldsymbol{\sigma}$ (following Tassoul 1978) appears in both the momentum Eq. (1b) and the dissipation function:

$$Q_{\rm visc} = \frac{1}{2\nu\Sigma}{\rm Tr}(\boldsymbol{\sigma}^2) = \frac{1}{2\nu\Sigma}\left(\sigma_{rr}^2 + 2\sigma_{r\phi}^2 + \sigma_{\phi\phi}^2 + \sigma_{zz}^2\right), \tag{2}$$

where $\nu = \alpha c_{\rm s} H$ is the kinematic viscosity parametrized according to the α-viscosity model of Shakura & Sunyaev (1973). Here, α is a parameter that captures both radial angular momentum transport – that leads to accretion onto the star – and heating of the disk due to viscous friction. Numerical simulations of (magneto)hydrodynamical instabilities such as the vertical shear instability (VSI, Nelson et al. 2013) or the magneto-rotational instability (MRI, Balbus & Hawley 1991) have provided numerical estimates of α, while observations of young stellar objects surrounded by disks have constrained these estimates (Dullemond et al. 2018). To probe a wide range of diffusion regimes from practically inviscid to moderately viscous, we choose $\alpha \in \{10^{-6}, 10^{-5}, 10^{-4}, 10^{-3}\}$ for our models.

Viscous dissipation leads to the heating of the disk. An embedded planet can also deposit significant amounts of thermal energy via the dissipation of spiral shocks (Rafikov 2016; Ziampras et al. 2020a). As a cooling solution, we allow the disk to relax to a prescribed temperature profile T_0 (see, Eq. (5)) over a relaxation timescale $\tau_{\rm relax} = \beta/\Omega_{\rm K}$ (Gammie 2001).

The thermal relaxation term appears as an additional source term to the energy equation

$$Q_{\rm relax} = -\Sigma c_{\rm v}\frac{T - T_0}{\beta}\Omega_{\rm K} \Rightarrow \frac{\partial T}{\partial t} = -\frac{T - T_0}{\tau_{\rm relax}}, \tag{3}$$

where $c_{\rm v} = \frac{R_{\rm g}}{\mu(\gamma-1)}$ is the heat capacity of the gas at constant volume. The parameter β controls the relaxation timescale, as well as the overall planet–disk interaction process (Miranda & Rafikov 2020b); we choose the values $\beta \in \{0.01, 1, 100\}$ which correspond to very fast, moderate, and very slow relaxation.

The gravity of the star and planet are included as a source term in $\boldsymbol{g}$. We work in a star-centered coordinate system and embed a planet with mass $M_{\rm p}$ at a position $\boldsymbol{r}_{\rm p}$. Thus, the source term reads

$$\begin{aligned}\boldsymbol{g} &= \boldsymbol{g}_\star + \boldsymbol{g}_{\rm p} + \boldsymbol{g}_{\rm ind}\\ &= -\frac{GM_\star}{r^3}\boldsymbol{r} - \frac{GM_{\rm p}}{(d^2+\epsilon^2)^{3/2}}\boldsymbol{d} - \frac{GM_{\rm p}}{r_{\rm p}^3}\boldsymbol{r}_{\rm p}, \quad \boldsymbol{d} = \boldsymbol{r} - \boldsymbol{r}_{\rm p}.\end{aligned} \tag{4}$$

The terms $\boldsymbol{g}_\star$, $\boldsymbol{g}_{\rm p}$, and $\boldsymbol{g}_{\rm ind}$ denote the acceleration due to the star, the planet, and the indirect term which is a correction needed because the star-centered frame is not an inertial frame. As we are considering fixed, nonmigrating planets, disk feedback on the star and planet is neglected. The planet's gravitational pull (second term in the RHS of Eq. (4)) is smoothed using a Plummer potential with a smoothing length $\epsilon = 0.6H(\boldsymbol{r})$ that captures the effect of the vertical structure of a more realistic 3D disk (Müller et al. 2012) and prevents singularities near the location of the planet.

For simplicity, we do not allow the planet to migrate. We chose to limit the degrees of freedom in our model to focus on the dynamics of the vortex and avoid complex and potentially chaotic interplay between the vortex and the planet (Lega et al. 2021). For the same reason of simplicity, we neglect planetary accretion in our models.

2.2. Numerics

We use two different codes for our numerical models: `PLUTO 4.2` (Mignone et al. 2007), a finite-volume, energy-conserving, shock-capturing code that treats transport by solving the Riemann problem across the interfaces of adjacent cells in both directions (r, ϕ) in an unsplit fashion; and our custom `FARGO` (Masset 2000) version, `FargoCPT` (Rometsch et al. 2020),

which uses a finite-difference, dimensionally split, second-order upwind method for gas advection. Both codes utilize the FARGO method (implemented into PLUTO by Mignone et al. 2012), in which orbital advection is essentially performed via the Keplerian rotation on top of which the code solves for the residual velocity deviations, significantly relaxing time-step limitations and reducing numerical dissipation in the process (Masset 2000).

The inherent differences between the two numerical schemes make it worthwhile to carry out our simulations using both codes, to verify the robustness of our results, and to test for numerical convergence. Namely, the strictly energy-conserving nature of PLUTO and the necessity for artificial viscosity to stabilize FargoCPT are discussed in more detail in Sect. 6.7, among others.

2.2.1. Grid setup

Our computational domain spans the full azimuthal extent and a radial range of $r \in [0.2, 5.0]\, r_\mathrm{p} = [1.04, 26.0]$ au, with square cells logarithmically spaced so that the cell aspect ratio is preserved. After carrying out a thorough investigation of the effects of our numerical resolution of the recovery of both radial and azimuthal features caused by the planet, we decided to execute our simulations using a resolution of 8 and 16 cells per scale height (hereafter "cps") in both directions (r, ϕ). Because we use a constant aspect ratio together with a logarithmically spaced radial grid, the resolution in cps is constant throughout the domain.

At this resolution, the two codes reach good convergence in terms of the presence and contrast of features shaped by the planet and results agree between the codes. This translates to a fiducial resolution of $(N_r, N_\phi) = (528, 1024)$ cells for 8 cps, or $(1056, 2048)$ cells for 16 cps. In addition, using the same resolution in both directions in terms of cps ensures that the effects of numerical viscosity are isotropic (see Appendix A).

2.2.2. Initial and boundary conditions

Our disk is initially axisymmetric and in equilibrium in the radial direction, such that the initial radial velocity profile results in a constant accretion rate through the disk. The azimuthal velocity is close to the Keplerian profile, with the correction due to the radial pressure gradient. The initial surface density and temperature profiles are simple power laws such that

$$\Sigma_0(r) = 222\,\mathrm{g\,cm^{-2}} \left(\frac{r}{r_\mathrm{p}}\right)^{-1/2}, \quad T_0(r) = 120.7\,\mathrm{K} \left(\frac{r}{r_\mathrm{p}}\right)^{-1}, \tag{5}$$

with $r_\mathrm{p} = 5.2$ au. This temperature profile translates to a disk with a constant aspect ratio $h(r) = H/r = 0.05$. While the general consensus is that protoplanetary disks are flared (i.e., the aspect ratio increases with distance, see e.g., Dullemond 2000), we choose to use a constant aspect ratio because the behavior and lifetime of vortices depends on this quantity (Hammer et al. 2021). Thus, we can isolate the dependence of vortices on the physical and numerical parameters in our suite of simulations.

The radial and azimuthal velocity components at $t = 0$ are then

$$u_r(r) = -\frac{3}{2}\frac{\nu}{r}, \quad u_\phi(r) = r\Omega_\mathrm{K}\sqrt{1 - 1.5\,h^2}. \tag{6}$$

Near the boundaries, within the radial extent $r \in [0.2, 0.25] \cup [4.2, 5.0]\, r_\mathrm{p}$, the surface density and velocity are both damped to their initial profiles (see Eqs. (5) and (6)) using the method of De Val-Borro et al. (2006) over a damping timescale of 0.3 periods at the respective boundary. While the radial boundary edges are closed, this minimizes the reflection of spiral waves back into the computational domain. The boundaries are periodic in the azimuthal direction.

We then embed a Jupiter-sized planet ($M_\mathrm{p} = 1\,M_\mathrm{J} = 10^{-3} M_\star$) in most models, with some simulations instead containing a less massive planet of $M_\mathrm{p} = 0.5\,M_\mathrm{J}$. To smoothly introduce the planet into the disk, we typically allow the planet to grow over 100 orbits at r_p using the formula by De Val-Borro et al. (2006). The importance of the growth timescale and planet mass are discussed in Sect. 4.

2.3. Vortex detection

We use the gas vortensity

$$\varpi = \frac{(\nabla \times \boldsymbol{u}) \cdot \hat{z}}{\Sigma}, \tag{7}$$

– where $\hat{z}$ is the unit vector in the vertical direction – as a proxy to detect and track the evolution of vortices over hundreds of snapshots for every model. As these vortices consist of anticyclonic motion, the center of a vortex corresponds to a local minimum in vorticity, $\omega = (\nabla \times \boldsymbol{u}) \cdot \hat{z}$. Because vortices tend to accumulate mass towards their center and Σ is enhanced inside the vortex, the transition from the background flow to the vortex region is stronger and the vortex is more easily identified in a map of ϖ than in the case of ω alone.

More precisely, we use the gas vortensity normalized by the background vortensity from the initial conditions, $\varpi_0 = (\nabla \times \boldsymbol{u}_\mathrm{K}) \cdot \hat{z} \,/\, \Sigma_0$. This eliminates the radial dependence of the Keplerian velocity and the disk's surface density and ensures that our vortex proxy quantity, ϖ/ϖ_0, is of order unity everywhere in the disk except for the gap region due to its very low surface density. The quantity ϖ/ϖ_0 usually varies between -1, for strongly counter-rotating vortices, and 1 for the background flow.

We use our new Python module, `Vortector`, which extracts iso-vortensity contours using the computer vision library `OpenCV` (Bradski 2000) to detect vortex candidates and then fits a 2D Gaussian to the vortensity and surface density data. The FWHM (or 2.355σ) of this Gaussian is used to define the radial and azimuthal extent of a vortex. Using this method, we also extract information about the shape of the vortex, including its radial and azimuthal extent and the mass it encloses. A more detailed description can be found in Appendix B.

One drawback is that this automated process sometimes produces detection artifacts, as can be seen for example in Fig. 6 below (top panel, dashed orange line), such that the vortex size (and therefore its mass) is overestimated near the end of its lifetime as it blends into the disk background. While this effect is partly counteracted by using a median filter in time, we do not manually edit the output of the `Vortector` on a model-by-model basis.

In the following three sections, we present the results of our simulations. First, we present a typical example of vortex formation and evolution (Sect. 3). We then go on to describe the dependence of vortices on physical parameters for the group of vortices with short and intermediate lifetimes (Sect. 4). Finally, long-lived and migrating vortices are presented (Sect. 5).

3. Typical life track of a vortex

The Jupiter-sized embedded planet opens a deep gap in all of our simulations. Figure 1 shows maps of Σ (left) and ϖ (right) normalized by their initial values at five time-stamps during the

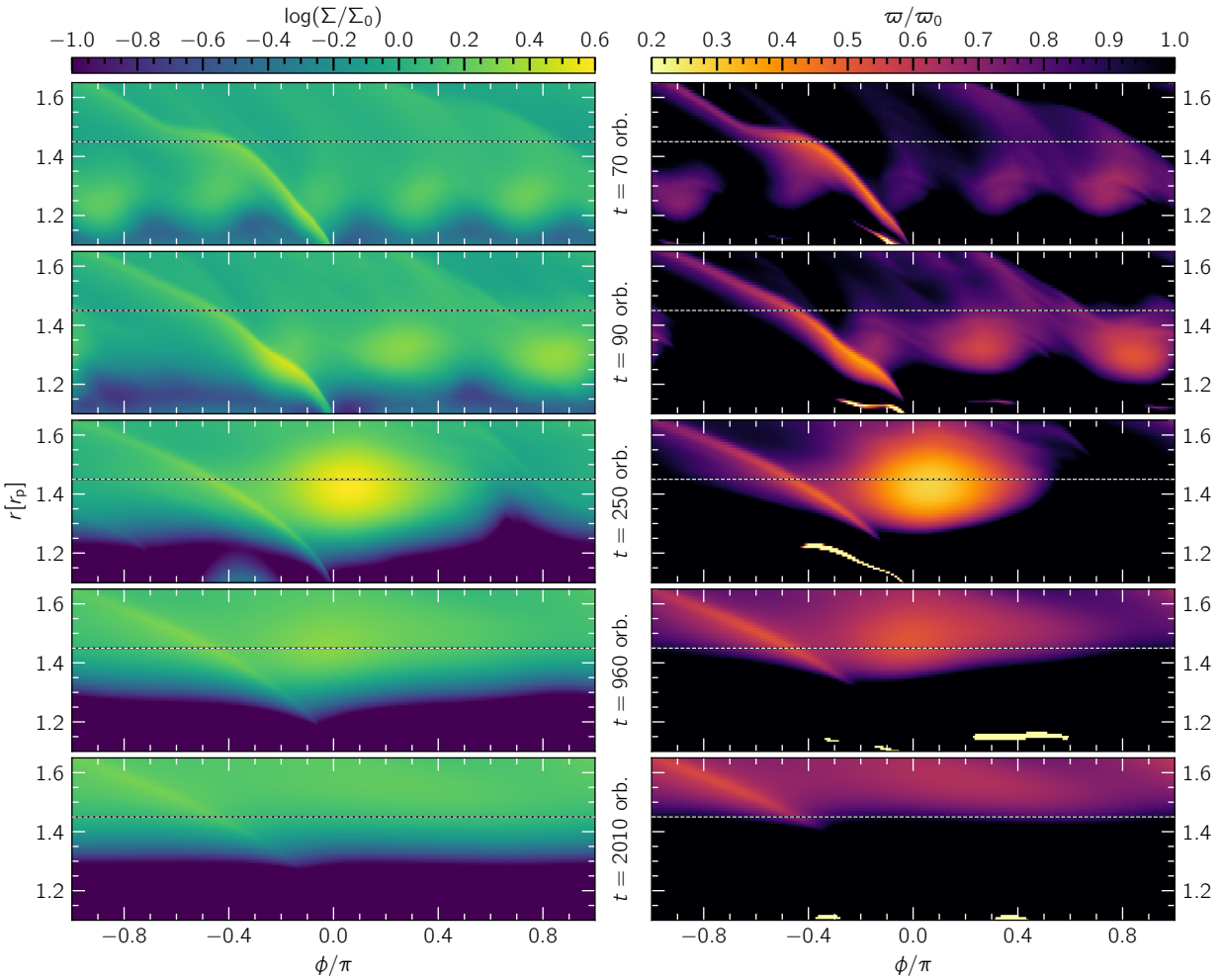

Fig. 1. Multiple snapshots of the $\alpha = 10^{-5}$, $\beta = 1$, 8 cps model showcasing the vortex merging process during the early stage of gap opening, the fully grown size of the resulting vortex, and its subsequent decay. The surface density and vortensity contrast compared to their initial profiles is shown in the *left* and *right panels*, respectively. Time is quoted in units of planetary orbits. The horizontal line at $r = 1.45\, r_p$ serves to highlight the outward radial movement of those structures as the gap around the planet grows wider. The planet is located at $r = 1\, r_p$ and $\phi = 0$.

vortex lifetime for a model with $\alpha = 10^{-5}$, $\beta = 1$, and a resolution of 8 cps performed with the `FargoCPT` code. Horizontal dotted lines at $r = 1.45\, r_p$ are superimposed as a reference marking the final location of the vortex center. Here, four small-scale vortices (top row) first merge into two slightly larger vortices (second row) and then finally into one massive vortex (middle) that will last for a little over 1100 orbits. The vortex slowly decays over time, maintaining a large size (fourth row). In the later stages, the vortex is no longer present (bottom row). The nonaxisymmetric structure still visible exists due to the planet's spiral arm and is corotating with the planet.

Early in the gap-opening process, the outer gap edge grows Rossby-wave unstable (Lovelace et al. 1999) and several small-scale vortices form around it (top two rows). Figure 2 shows radial profiles of the Lovelace parameter, $\mathcal{L}$, (top) and Σ (bottom) at different time-stamps during the vortex formation up until $t = 180$ orbits. The Lovelace parameter is defined as

$$\mathcal{L} = \frac{S^{2/\gamma}}{\varpi}, \tag{8}$$

with the entropy $S = P/\Sigma^{\gamma}$. The development of a maximum in $\mathcal{L}$ is visible, which is one condition for the onset of the RWI. Vertical lines at the center of the $\mathcal{L}$ maxima (as determined by eye) are added to both panels to guide the eye for a comparison of the location of the maxima in $\mathcal{L}$ and Σ at each time-stamp. The $\mathcal{L}$ maxima are located on the slope of the gap edge slightly inward from the Σ maxima and coincide with the location of the small vortex centers. The maximum in $\mathcal{L}$ moves outward following the maximum in Σ as the gap opens. This illustrates that the vortices form due to the RWI at the slope of the outer gap edge.

In the absence of self-gravity, these small vortices then quickly merge together (within ∼100 planet orbits) into a single large vortex that slowly moves outwards following the gap edge as the gap deepens and widens (third and fourth rows in Fig. 1). The surviving vortex then typically decays over ∼200–2000 orbits. The evolution of three vortex properties is illustrated in Fig. 3, where we show, from top to bottom, the mass $M_{\rm vort}$ enclosed within the FWHM ellipse of the 2D Gaussian fit to Σ, the location of the center of the vortex $r_{\rm vort}$ and the radial FWHM width Δr as the shaded area, and the vortensity at the

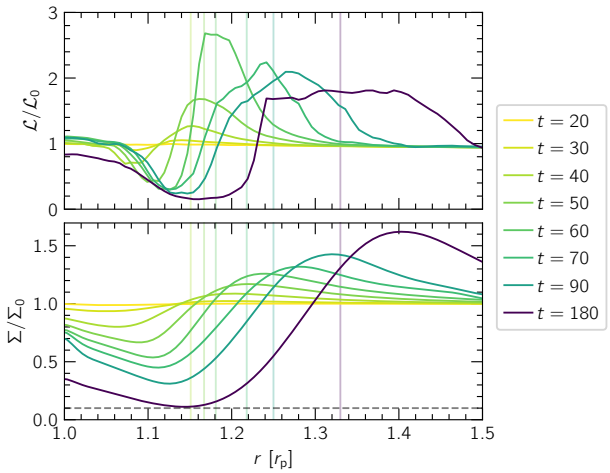

Fig. 2. Evolution of radial Lovelace parameter (see Eq. (8)) and Σ profiles during vortex formation over the first 200 orbits of the sample case from Sect. 3. The vertical lines indicate the center of the plateau in $\mathcal{L}$ (estimated by eye) to guide the eye to the corresponding location of the Σ profile. $\mathcal{L}$ is calculated as the azimuthal average at each radius. The dotted horizontal line in the *bottom panel* marks 10% of Σ_0, which we define as the location of the gap edge.

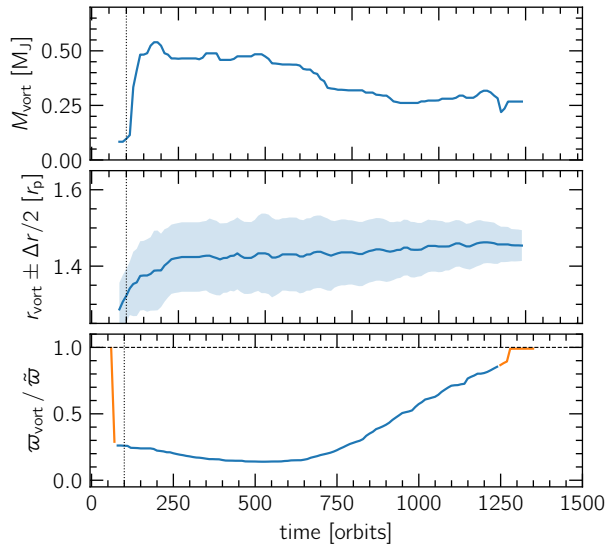

Fig. 3. Evolution of vortex properties for the showcase simulations presented in Sect. 3. The panels show, *from top to bottom*, the mass enclosed in the FWHM ellipse of the vortex fit M_{vort} in Jupiter masses, the radial location of the vortex r_{vort}, and its FWHM Δr, indicated by the shaded area, and the ratio between minimum vortensity inside the vortex and the azimuthal median of vortensity at the radial location of the vortensity minimum. A dotted vertical line indicates the time when the planet has reached its final mass. The curves are smoothed with a median filter that spans over the preceding and following five datapoints (±50 orbits at r_p). The orange parts of the line in the bottom panel show the evolution of the vortensity prior to the "birth" and after the "death" of the vortex.

vortex center normalized by the azimuthal median. The vertical dotted lines indicate the time when the planet reached its full mass (typically 100 orbits). A short phase of vortex formation is followed by a slow and steady decay process, as can be seen in the decrease of mass and radial size. Because the vortensity contribution of the anticyclonic vortex is negative, an increase in vortensity indicates a decay as well. The line in the bottom panel of Fig. 3 is continued (in orange) for another 100 orbits after the vortex has decayed – according to our criterion presented below in Sect. 4.1 – in order to illustrate the return of the curve to 1, which corresponds to an azimuthally symmetric state.

During its lifetime, the vortex can become as large as $\Delta r = 0.4\, r_p$ (2 au for $r_p = 5.2$ au) with a typical vortex aspect ratio ($r\Delta\phi/\Delta r$) of 6-10. Its mass, M_{vort}, is typically some tenths of M_J but can be as large as one M_J, with a surface density enhanced by a factor of up to seven compared to the initial value.

The vortices form around the location where the radial Σ profile reaches 10% of its initial value (see bottom panel of Fig. 2), which we define as the gap edge in a similar way to Crida et al. (2006). During their lifetime, most vortices tend to stick to this gap edge in the sense that their inner boundary, $r_{vort} - \Delta r/2$, roughly coincides with the location of the gap edge. For some models, we observe that the vortex detaches from the outer gap edge after several hundred orbits and starts migrating outward. These models are discussed in Sect. 5.

4. Dependence of vortex properties on physical parameters

Having described a typical lifetrack of a vortex in our simulations, we now present the effects of different physics and numerics on vortex lifetime, location, and impact on the overall disk structure. The model parameters are listed with the main results in Table C.1.

4.1. Vortex lifetime

We define the vortex lifetime as the time difference between its "birth" and "death" by analyzing the ratio of ϖ to the azimuthal median value $\tilde{\varpi}$ as a function of time. The normalization with $\tilde{\varpi}$ instead of ϖ_0 is done to eliminate the ϖ evolution of the background disk due to changes in Σ and radial pressure gradients, which affect $(\nabla \times \boldsymbol{u}) \cdot \hat{z}$ by changing the azimuthal velocity.

The "birth" is identified as the time when $\varpi/\tilde{\varpi}$ drops from its initial value of 1 (for an axisymmetric disk) down to lower values (see bottom panel of Fig. 3). Because $\varpi/\tilde{\varpi}$ drops already for small vortices, the lifetime also includes the stage where there are multiple small vortices (see Sect. 3).

The "death" of the vortex on the other hand is less obvious to identify. At this stage, $\varpi/\tilde{\varpi}$ usually slowly rises back to the value of the background disk. Usually, there is a "knee" visible in $\varpi/\tilde{\varpi}$ at or slightly after the point in time where the vortex dies and where ϖ approaches the background flow (see the orange part of the line in the bottom panel of Fig. 3 where $\varpi/\tilde{\varpi}$ is continued for another 100 orbits after the vortex disappeared at $t = 1250$ orbits). For some models, this knee is not visible, and we manually inspect the 2D contour plots of $\varpi/\tilde{\varpi}$ and identify the point after which no further closed iso-value lines (with spacing in $\varpi/\tilde{\varpi}$ of 0.05) are present. As an additional measure for less obvious cases, we analyze the gas streamlines at different time-stamps.

In our models, the drop in $\varpi/\tilde{\varpi}$ happens in a matter of tens of orbits. A conservative estimate for the uncertainty of this birth time measurement is 50 planetary orbits. From applying the manual method to models where the knee exists in the $\varpi/\tilde{\varpi}$ curve (implying the death of the vortex), we estimate a conservative uncertainty to be 100 planetary orbits. This leaves a

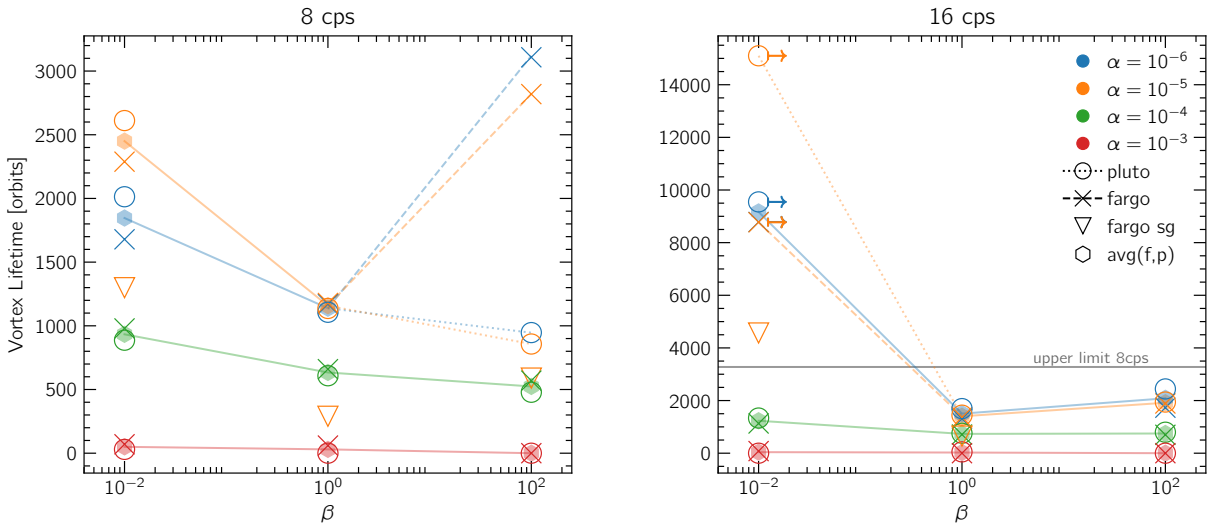

Fig. 4. Lifetime of vortices as a function of β for 8 cps (*left*) and 16 cps resolution (*right*). Colors encode α, and the different symbols denote the code and the inclusion of self-gravity. The solid lines help guide the eye and connect the lifetime averages between the two codes (without self-gravity) for each value of α, where the two codes agree sufficiently. For parameters where there is a difference between the codes, dashed and dotted lines connect to the datapoints of the `FargoCPT` and `PLUTO` runs, respectively. A "↦" next to a symbol marks models that were terminated due to runtime constraints but still contain an active vortex. The horizontal gray line in the *right panel* indicates the top of the y-axis of the *left panel*. A list of all vortex lifetimes shown here is provided in Table C.1.

total uncertainty of 150 planetary orbits for the lifetime of our vortices.

The lifetime of vortices in our grid of simulations is shown as an overview in Fig. 4. The left and right panels show vortex lifetimes as a function of β for 8 and 16 cps, respectively. The viscous α is encoded in color, and the symbol indicates the simulation code and the inclusion of self-gravity. For each value of α and β, we calculated the average ("avg(f,p)") between the two codes (not including the self-gravity models) when the results are close together. The solid-colored lines connect the averages to help visualize the trends. For parameters for which the two codes showed different vortex lifetimes, we added separate lines connecting the average to the `FargoCPT` and `PLUTO` results to highlight the differences.

Lifetimes range from approximately 200–2000 orbits for the shorter-lived vortex group up to at least 15 000 orbits for the long-lived vortices discussed later in Sect. 5. The most prominent features of the distribution are the trend of decreasing lifetime with increasing α and the minimum vortex lifetime at $\beta = 1$ for low α and high resolution. In the following sections, we address the influence of our model parameters on vortex lifetime.

4.2. Influence of the thermal relaxation timescale

The dimensionless thermal relaxation timescale β has a strong effect on vortex lifetime. For $\alpha = 10^{-4}$, lifetimes are of the order of several hundred to 1000 orbits with a downward trend as β increases. Vortex lifetimes are shortest for $\beta = 1$ (around 1250 orbits) and increase towards both sides to around 2000 orbits for $\beta = 100$ and to values of the order of 10 000 orbits for $\beta = 0.01$, high-resolution runs. This decrease in lifetime for nonisothermal disks is consistent with the results of Tarczay-Nehéz et al. (2020). Exceptions to this trend are the 8-cps `PLUTO` models for $\alpha = 10^{-5}$–10^{-6} and $\beta = 100$. We were not able to identify the reason why the two codes did not agree for these parameters, but we note that the two codes match well once again for 16 cps in the same configurations. Models with very long vortex lifetimes are analyzed in Sect. 5.

Fung & Ono (2021) reported a similar trend in vortex lifetime in 2D shearing-box simulations without planets, in which the vortex was introduced by initializing the simulation with a radial density bump. These authors found that vortex decay is fastest for intermediate β in the range 1–10, but their disk model assumes a constant background disk without gradients in T and Σ, which change baroclinic effects. Our results indicate that a similar mechanism might be at play in the presence of an embedded planet with strong spiral-arm shocks. However, the strong enhancement of vortex lifetime for $\beta = 0.01$ hints at the presence of an additional mechanism which keeps the vortices alive. We discuss these hypotheses further in Sect. 6.1.

For a comparison of vortex evolution at different β, see Fig. 5, where the evolution of vortex properties (analogous to Fig. 3) of three `FargoCPT` simulations at 8 cps resolution with $\beta = 0.01, 1$, and 100 is shown. The absolute radial location of vortices varies with β as well. This is due to the tendency of the vortices to form and subsequently stick to the outer planet gap edge and the gap-opening process being strongly influenced by β. Miranda & Rafikov (2020b) showed that "extreme" values of β (i.e., $\beta \to 0$ or $\beta \to \infty$) result in narrower planet-opened gaps but additional gaps in the inner disk, whereas intermediate values of $\beta \sim 0.1$–10 lead to a single, wide gap around the orbit of the planet. In our simulations, models with $\beta = 0.01$ show the widest gaps, narrower gaps are present for $\beta = 1$, and $\beta = 100$ models showed an even slightly narrower gap. This is reflected in the vortex locations which are further in for higher β (see the center panel of Fig. 5). The difference between our results and those of Miranda & Rafikov (2020b) might be due to the presence of the vortex.

4.3. Planet growth timescale

Hammer et al. (2017) observed that the lifetime of planet-induced vortices can depend on the timescale over which the planet mass

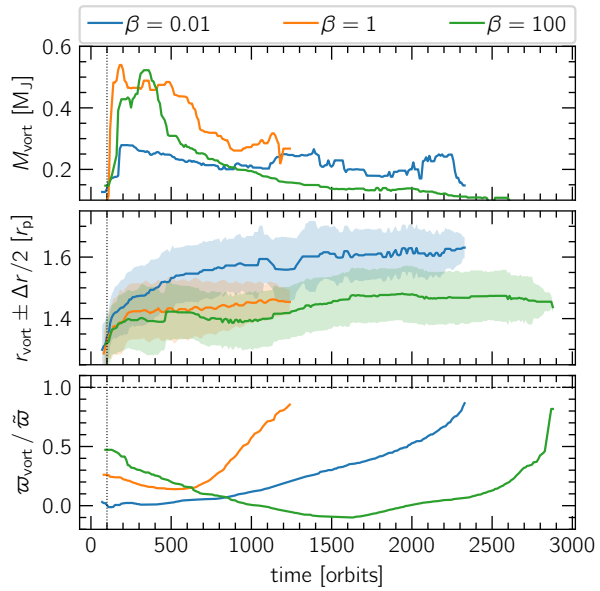

Fig. 5. Evolution of vortex properties for varying values of the thermal relaxation β parameter. The panels are as in Fig. 3. Shown are models run with the FargoCPT code with $\alpha = 10^{-5}$ and at 8 cps resolution (orange "f8" dots in Fig. 4).

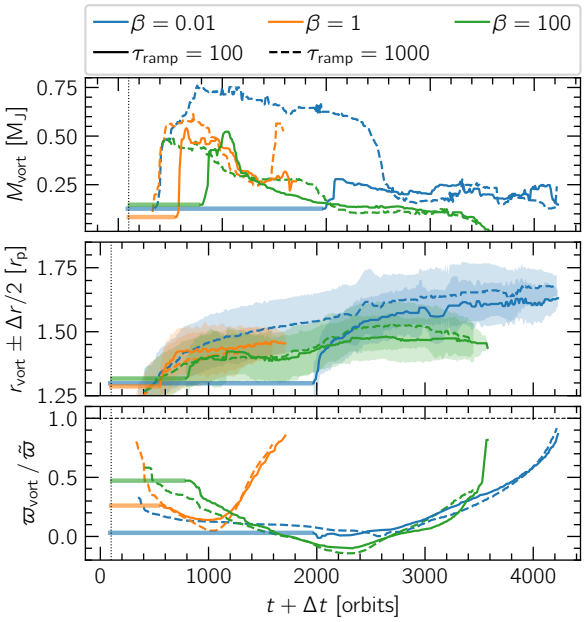

Fig. 6. Influence of the planet introduction time on the evolution of vortex properties. The panels are as in Fig. 3. Solid and dashed lines show models with $\tau_{ramp} = 100$ orbits and 1000 orbits, respectively. The $\tau_{ramp} = 100$ orbits curves are shifted to the right (see the horizontal lines) to illustrate that the curves have the same shape in the decay phase, independent of τ_{ramp}. We note that the final evolution of the vortex, after it has reached its minimum in vortensity, is the same independent of planet introduction time.

is increased in order to introduce the planet into the simulation. These authors found that vortex lifetime decreased with a longer planet growth time. In our models, increasing the planet growth timescale from 100 to 1000 orbits caused vortices to live longer by 470 orbits for $\beta = 1$, and by up to 1900 orbits for $\beta = 0.01$. Figure 6 shows the evolution of vortex quantities comparing the FargoCPT runs with a $\tau_{ramp} = 100$ orbits, already presented in Fig. 5, with their respective counterparts with $\tau_{ramp} = 1000$ orbits. The curves of runs with $\tau_{ramp} = 100$ orbits are shifted to the right by the difference in lifetime Δt compared to the respective $\tau_{ramp} = 1000$ orbits model. This shift clearly illustrates that the decay of these vortices is almost the same for both values of τ_{ramp} in terms of their mass, location, and vortensity curves. The only difference caused by the planet injection timescale appears in the time it takes for the vortex to reach the turnover point, after which it starts to decay.

4.4. Planet mass

From our $M_p = 0.5\,M_J$ models we cannot draw any conclusions regarding the dependence of vortex lifetime on planet mass, because for the set of parameters $\beta = 0.01$ and $\alpha = 10^{-5}$ the vortices are long-lived outliers like the ones discussed in Sect. 5. However, the location of the vortex is also influenced by the planet mass. Lower-mass planets open narrower gaps and cause the location of the vortex to be further in compared to more massive planets because this location is linked to the location of the gap edge. In our models, the vortices in the $M_p = 0.5\,M_J$ were located ~0.15 r_p closer to the star.

4.5. Viscosity

The observed vortex lifetime typically increases with lower values of α. Simulations with $\alpha = 10^{-3}$ show only small vortices forming. These disappear within 100 orbits, and are therefore already gone by the time the planet has grown to its full mass. For models with $\alpha = 10^{-4}$, we observe vortex lifetimes of up to around 1000 orbits.

Simulations with a lower viscosity ($\alpha = 10^{-6}$–10^{-5}) show even longer lifetimes, usually in the range between 1000 and 2000 orbits, excluding the outliers that we discuss later in Sect. 5. For this range of α, vortices usually have similar lifetimes for simulations sharing the same β value. An example of this is shown in See Fig. 7, which shows, from top to bottom, the evolution of the mass enclosed in the region of the vortex (FWHM), the location and radial extent (in FWHM) of the vortex as determined by the surface density fit, and the ratio of normalized vortensity to the azimuthal median of the latter at the location of the vortex.

The vortex location is not influenced by viscosity. Although the gap-opening time is $t_{gap} \approx 2700 \left(\frac{\alpha}{10^{-3}}\right)^{-3/2} T_{orb}$ according to the estimate in Kanagawa et al. (2017), the bulk of the gas in the vicinity of the planet is cleared within the first few hundred orbits. During this time, Σ is lowered by two orders of magnitude within the gap region, and the radial gradient of Σ becomes steep enough to facilitate vortex formation.

4.6. Self-gravity

Several studies showed that vortices in weakly or strongly self-gravitating disks might not grow as large because small vortices do not merge into one large vortex (Lin & Papaloizou 2011) and dissipate more rapidly because of stretching in the azimuthal direction (Lovelace & Hohlfeld 2013; Regály & Vorobyov 2017; Zhu & Baruteau 2016). This can be the case even for low-mass disks as long as the Toomre stability parameter Q is lower than

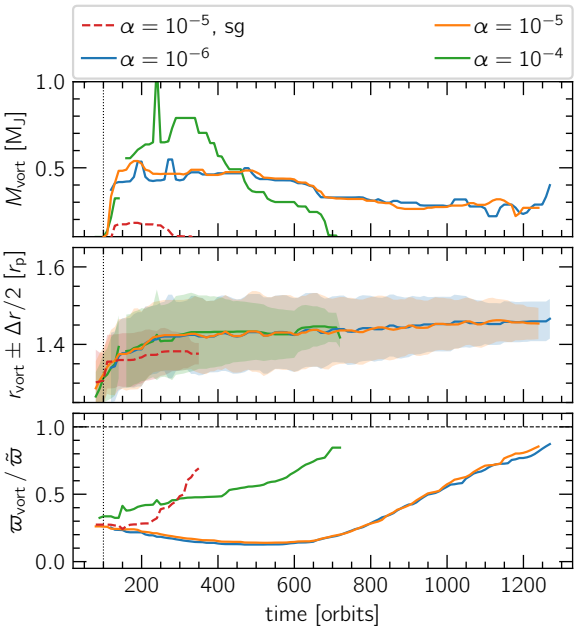

Fig. 7. Evolution of vortex properties for varying values of α. Panels are shown as in Fig. 3. Shown are models run with the FargoCPT code with $\beta = 1$ and at 8 cps resolution. The $\alpha = 10^{-3}$ run is excluded because no vortex forms. In addition, a run with disk self-gravity enabled is added for the $\alpha = 10^{-5}$ case. The similarity between simulations with $\alpha = 10^{-5}$ and 10^{-6} is apparent.

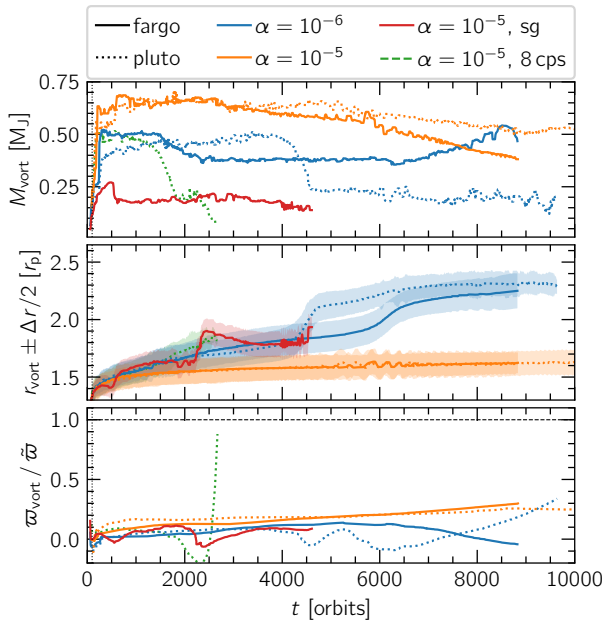

Fig. 8. Selection of models with long-living and migrating vortices at 16 cps resolution for the two different codes. Both codes agree remarkably well for the blue and orange cases. The panels are as in Fig. 3. In models shown here, $\beta = 0.01$. The values of α, the resolution, and the code used are indicated in the legend.

50 or $hQ \leqslant \frac{\pi}{2}$. For the choice of parameters in our models, the Toomre parameter is $Q \approx 25\,(r/r_\mathrm{p})^{-3/2}$ ($hQ \approx 1.25\,(r/r_\mathrm{p})^{-3/2}$), dropping under 5 at roughly $r/r_\mathrm{p} = 2.8$. To check the effect that disk self-gravity has in our models, we ran additional simulations with FargoCPT with self-gravity activated for all three values of β (0.01, 1, and 100) and $\alpha = 10^{-5}$.

The lifetimes of vortices in these simulations are shown in Fig. 4 as the rightmost datapoint in each column (models "f8sg"). An example evolution of their properties is shown in Fig. 7.

Self-gravity inhibits the merging of the small initially formed vortices into one large vortex. Instead, two smaller vortices usually remain until they decay. This leads to a significantly shorter lifetime compared to the analogous simulations without self-gravity, which is consistent with the findings of the studies mentioned above. However, this does not apply to the long-lived migrating vortices discussed in Sect. 5.

Figure 7 shows that the center of the vortex in a model with self-gravity and $\beta = 1$ is further in compared to its nonself-gravitating counterpart. This is due to the smaller radial extent of the vortex in the run with self-gravity and the tendency of the inner edge of each vortex to coincide with the gap edge. Because self-gravity does not noticeably change the radial disk profile for the mass regime of our models, the inner edge of the vortices is at the same location, independent of whether self-gravity is included or not. The same effect is also observed for $\beta = 0.01$ and $\beta = 100$.

5. Long-lived and migrating vortices

In some of the cases, a much longer lived vortex is observed. In these models, vortices stay close to their peak mass for several thousand orbits, and in some cases migrate outwards after having stayed at the planet gap edge. This happens only for very low viscosities ($\alpha \leq 10^{-5}$) and $\beta = 0.01$ or locally isothermal simulations ($\beta \to 0$). For our standard $M_\mathrm{p} = 1\,M_\mathrm{J}$ planets, the long-lived outliers appear only at the highest resolution of 16 cps but not at 8 cps. For the corresponding $M_\mathrm{p} = 0.5\,M_\mathrm{J}$ model, the long-lived vortex also appeared at 8 cps. Spiral arms launched by the vortex are clearly visible for these long-lived large vortices (see Fig. B.2). They are more pronounced for lower values of α.

Figure 8 shows the evolution of vortex properties for a selection of models to highlight the observed behavior. The most prominent example is the model with $\alpha = 10^{-5}$, $\beta = 0.01$, and a 16 cps resolution. The vortex in those runs lived for 15 100 orbits before we terminated the two simulations because of their long runtime. Both codes, PLUTO and FargoCPT, agree well for the long-lived cases. Specifically, they are in exceptionally close agreement for $\alpha = 10^{-5}$ and only differ at later stages for $\alpha = 10^{-6}$ (see orange and blue lines in Fig. 5). We do not currently fully understand the mechanism that allows these long-lived vortices to sustain themselves for such long timescales. We attempt to provide a speculative explanation in Sect. 6.1.

For $\beta \neq 1$, a secondary radial density and pressure bump is observed in the outer disk. This is the result of the vortex generating spiral arms which transport angular momentum. Radially outwards, this results in the accumulation of mass in a second bump (see panels for $\beta \neq 1$ in Fig. 9). This does not happen for $\beta = 1$ because of the less efficient angular momentum transport by spiral arms for this intermediate value of β (Miranda & Rafikov 2020b). For $\beta = 0.01$, some models show vortices migrating radially outwards (e.g., the $\alpha = 10^{-6}$ models in Fig. 8). This is likely related to the formation of the secondary bump outside of the vortex location (see Fig. 9) and the fact that vortices typically migrate towards pressure bumps (Paardekooper et al. 2010). For vortices that migrate far enough outside, which

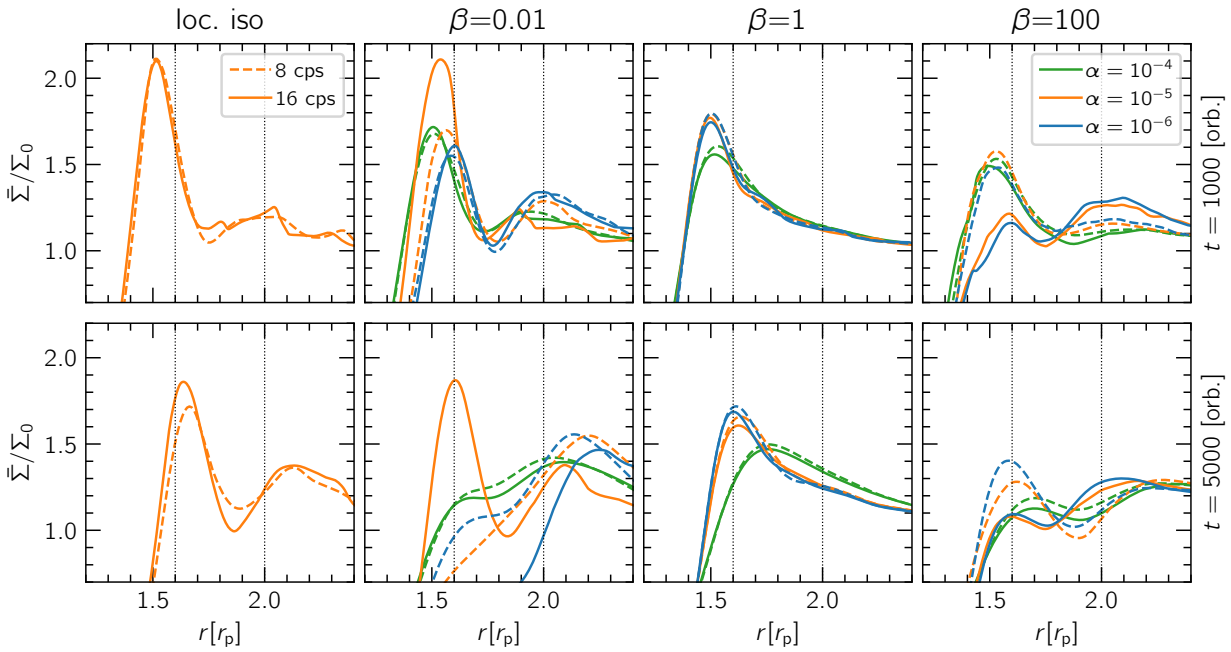

Fig. 9. Azimuthally averaged surface density profiles as a function of different physical (α, β) and numerical (cps) parameters at two different time-stamps. The peak around $r/r_p = 1.5$–1.6 corresponds to the pressure bump formed by the planet as the latter pushes material away, forming a gap around its orbit. The smaller, secondary peak at around $r/r_p = 2.1$ is caused by the vortex that forms near the primary, planet-generated bump. *Top*: radial profiles at $t = 1000$ orbits. At this stage, all models pictured feature a vortex near the primary bump. We note the absence of a secondary bump for the models with $\beta = 1$. *Bottom*: same profiles at $t = 5000$ orbits. Here, the primary bump has moved radially outwards as the planet's gap gets deeper and wider. We highlight the depletion of gas near the primary pressure bump for the *second panel from the left* ($\beta = 0.01$). This is caused by the combination of a vortex migrating outwards to the secondary bump, and the inability of the planet to resupply that zone with material from its now-depleted gap region. We also note the difference between resolutions of 8 and 16 cps (dashed and solid lines), especially for the $\beta = 100$ models and the $\beta = 0.01$, $\alpha = 10^{-5}$ model (the evolution of this model is shown as the orange line in Fig. 8).

only happens for $\beta = 0.01$, a weaker secondary vortex appears between them and the edge of the planet-generated gap (see Fig. B.2). These secondary vortices then decay over a few hundred orbits, already having decayed by the time the primary vortex disappears. While they are treated as independent entities, these secondary vortices are not included in Fig. 4 or the discussion above; their occurrence is likely the result of a multistage process which begins with the secondary bump forming and the primary vortex migrating radially outwards towards it and meanwhile supplying mass towards the edge of the planet-generated gap. This then feeds the emerging "secondary" vortex.

6. Discussion

In this section, we address some ways in which our results could be interpreted and their relevance in explaining observations. We also underline some caveats of our models.

6.1. The conditions needed to form and sustain a vortex

To form a vortex, one needs to create a local vortensity extremum. In the absence of nonconservative forces, the evolution equation for the vortensity in a 2D flow reads

$$\frac{\partial \varpi}{\partial t} + \boldsymbol{u} \cdot \nabla \varpi = \frac{\nabla \Sigma \times \nabla P}{\Sigma^3} \cdot \hat{z} + \mathcal{V} = \mathcal{B} + \mathcal{V}, \tag{9}$$

where $\mathcal{B} = \frac{\nabla \Sigma \times \nabla P}{\Sigma^3} \cdot \hat{z}$ is the baroclinic term and $\mathcal{V}$ describes viscous diffusion of vortensity which can lead to vortex decay.

As outlined in the introduction, several instabilities have been discovered that provide a mechanism to form or destroy large-scale vortices, but they all fundamentally rely on Eq. (9) to change the vortensity of the flow. The mechanism responsible for the formation of the vortex in our simulations is most likely the RWI which is triggered during the gap-opening process, as we demonstrated in Sect. 3 and Fig. 2.

To check whether vortices can only form during the gap-opening process and not in the quasi-steady state after the bulk of the gas has been pushed out of the gap region, we removed the long-lived vortex from the $\alpha = 10^{-5}$, $\beta = 0.01$, 16 cps model by replacing the velocities and Σ with their azimuthal median values for $r > r_p$ during the peak of its activity ($t = 1880$ orbits). The fact that there is no vortex forming again is an indication that the formation of vortices in our simulations depends on the gap-opening process to produce conditions that can trigger the RWI. This is also supported by the observation that the peak in $\mathcal{L}$ is strongest for an intermediate time, $t = 70$ orbits, during the gap opening process, after which the maximum disappears and a plateau in $\mathcal{L}$ forms.

Vortex decay happens due to at least two mechanisms. Viscous spreading attacks the vortices for high $\alpha = 10^{-4}$–10^{-3}, as illustrated by the trend of lower vortex lifetime for higher α, and vortex stretching due to self-gravity effects additionally limits the vortex lifetime, if it is considered (Lin & Papaloizou 2011; Zhu & Baruteau 2016; Regály & Vorobyov 2017). For sufficiently low α, another process that depends on β starts to be dominant. We do not fully understand the mechanism but we

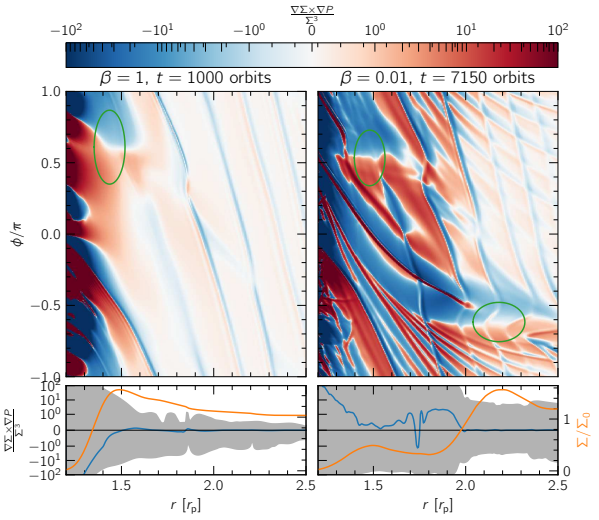

Fig. 10. Baroclinic term (RHS of Eq. (10)) in the outer disk for a short-lived model ($\beta = 1$ at $t = 1000$ orbits) and a long-lived vortex ($\beta = 0.01$ at $t = 7150$ orbits, see also Fig. B.2) with $\alpha = 10^{-5}$ and 16 cps resolution on the *left and right side*, respectively. The *top row* shows maps of the baroclinic term with the detected vortices indicated with green ellipses as obtained from the Σ fit. The *bottom row* shows the radial Σ profile in orange, the azimuthally averaged baroclinic term in blue and the region between its minimum and maximum shaded in gray.

observed some similarities to the recent work by Fung & Ono (2021). These latter authors find that, in their simulations, vortices decay the fastest for $\beta = 1$–10 and decay slower for both smaller and larger β. Vortex lifetime in their simulations changes by up to an order of magnitude depending on β. We also find a minimum in vortex lifetime for $\beta = 1$ with lifetimes increasing as $\beta \neq 1$.

Fung & Ono (2021) explained the decay mechanism by asymmetries in the structure of $\mathcal{B}$ around the vortex center, which they found to be quadrupolar (see their Fig. 6) and to change with β. We also find asymmetries in the structure of $\mathcal{B}$, but our simulations differ from theirs in some fundamental aspects. Our simulations are global with radially varying Σ and T profiles and include a planet that continually perturbs the disk, whereas the simulations of Fung & Ono (2021) consider a local shearing sheet with a constant background Σ and T, with only an initial perturbation in the form of a density bump. As a consequence of the radially varying T in our simulations, the structure of $\mathcal{B}$ around the vortex center is dipolar in the azimuthal direction, as can be expected for a Gaussian-like density maximum. Additionally, the planetary spiral arms strongly influence $\mathcal{B}$. Figure 10 shows a 2D map of $\mathcal{B}$ for two simulations with $\alpha = 10^{-5}$ and 16 cps resolution. The left panels show a short-lived vortex with $\beta = 1$ at $t = 1000$ orbits and the right panels show the long-lived vortex model which exhibits the secondary vortex (see Sect. 5 for a description and Fig. B.2 for ϖ and Σ maps at the same time). The actual shape of the perturbation of $\mathcal{B}$ inside and around the vortex varies in time because it depends on the phase with respect to the spiral arm. It is currently not clear to us how the changes in structure of $\mathcal{B}$ lead to the change in vortex decay and how this proposed mechanism depends on the various parameters in our system.

The long-lived group of vortices for low β (see Sect. 5) indicates that there might be another vortex formation mechanism at play. Given that the RWI already caused finite perturbations in the disk and our disks exhibit a radial entropy gradient, the SBI (Klahr & Bodenheimer 2003; Lesur & Papaloizou 2010) seems to be a natural candidate. However, we verified that the SBI is not active in our disks by analyzing the Richardson number, the ratio of the buoyancy (also called Brunt-Väisälä) frequency to the shear rate, which needs to be negative in a radially extended region over the full azimuth of the disk for the SBI to operate. The Richardson number in our simulation is positive, except for narrow stripes following the spiral arms, which rules out that the SBI is active.

To rule out that the difference in lifetime is a result of the initial vortex formation during gap opening, we took the long-lived vortex out of the $\alpha = 10^{-5}$, $\beta = 0.01$, 16 cps model and inserted it into the $\alpha = 10^{-5}$, $\beta = 1$, 16 cps model. Although this artificial vortex has the same structure as in its original $\beta = 0.01$ model, it decays over nearly the same time as the standard $\beta = 1$ vortex. This is an additional indication that the difference in lifetime is caused by the dependence of the decay process on β or a possible additional vortex formation channel that sustains the vortex at low β.

This leaves us with the hypothesis that the interaction of the spiral arms with the vortices might play a major role in either slowing down vortex decay or providing an additional vortex formation channel. This hypothesis is motivated by the strong impact of the spiral arms on $\mathcal{B}$ and the dependence of spiral-arm properties on β (Ziampras et al. 2020b; Miranda & Rafikov 2020b). Another contribution might be the vortensity jump across the spiral-arm shock, which was recently illustrated to be important for the evolution of vortensity in the case of subthermal-mass planets (Cimerman & Rafikov 2021). Providing an analysis of both mechanisms in our context is unfortunately out of the scope of the present explorative study.

6.2. Effect of in-plane radiation transport

It has been shown that parametrizing radiative effects with β while omitting the effects of in-plane radiation transport can result in a potentially inaccurate radial surface density structure, mainly in the inner disk and around the gap, due to the impact of β on the capability of a planet to open multiple secondary gaps at $r < r_p$ (Miranda & Rafikov 2020b). Here, we are not interested in the annular structures of the inner disk, and so we chose to ignore in-plane radiation transport. Nevertheless, to check for possible effects of in-plane radiation transport on the vortex dynamics, we repeated the $\alpha = 10^{-5}$, $\beta = 1$ model at 8 cps. This time we included a flux-limited diffusion (FLD) approach (Levermore & Pomraning 1981) similar to Ziampras et al. (2020a), but by parametrizing the diffusion coefficient $D_{\rm rad}$ following Eqs. (12)–(14) of Flock et al. (2017):

$$t_{\rm cool} \approx \frac{l_{\rm thin}^2}{3D_{\rm rad}} + \frac{H^2}{D_{\rm rad}} = \beta\Omega_{\rm K}^{-1} \Rightarrow D_{\rm rad} = \frac{\Omega_{\rm K}}{\beta}\left(\frac{l_{\rm thin}^2}{3} + H^2\right), \quad (10)$$

where $l_{\rm thin}$ is the photon mean free path. We found that including FLD slightly changes the radial surface density structure in the inner disk as predicted by Miranda & Rafikov (2020b) and reduces the vortex lifetime from 1200 to 900 orbits. Studying the effect of in-plane radiation transport in more detail requires further investigation.

6.3. The assumption of a 2D disk

One of the main limitations of our models is the 2D assumption, which was chosen because of runtime constraints in our rather

wide exploration of the parameter space. It is entirely possible that various 3D effects can result in quantitative differences in vortex properties. Three-dimensional vortices can be susceptible to the elliptical instability (Lesur & Papaloizou 2009) which would lower their lifetime. On the other hand, the vertical modes of the SBI could provide an additional channel to sustain the vortices, and vertical gas circulation due to the VSI might interfere with vortex growth and decay (Flock et al. 2020).

To estimate the impact of including full-3D effects, we ran one 3D simulation with FARGO3D (Benítez-Llambay & Masset 2016) using a setup analogous to our 2D setup. We chose $\beta = 2\pi$, $\alpha = 0$ and a resolution of 8 cps in all three directions. The simulation assumed symmetry about the midplane and covered four scale heights in the vertical direction. Similar to our 2D models, a large vortex formed at the outer gap edge and lived for 7000 orbits. This illustrates that while there are differences, large vortices can survive in 3D disk simulations for a long time, even longer than in 2D for our example. We limited the 3D runs to this one test because its runtime at 8 cps resolution was close to 4 months with the simulation performed on four NVIDIA K80 GPUs.

6.4. Observability of vortices at large radii

Section 4.2 illustrates that vortex lifetime is affected by the thermal cooling timescale β. The latter is expected to vary with radius in a disk, with values of 1–10 at 5 au, 0.1 at ∼10 au, and below 0.1–0.01 at ∼50 au (Ziampras et al. 2020b). Thus, we expect vortices to be in the short-lived regime close to the star and in the long-lived regime far from the star. From Fig. 4 we can estimate the lifetime of vortices in disks with $\alpha \leq 10^{-4}$ to be between 500 and 3000 orbits for $\beta \geqslant 1$ and between 1000 and 15 000 orbits for $\beta < 1$ for $\alpha \leq 10^{-4}$. Assuming a solar-mass star, this yields estimated lifetimes for a planet-induced vortex in the range of 6–30 kyr at 5 au, 175–700 kyr at 50 au, and 1–15 Myr at 100 au. On the basis of a simple lifetime-centered argument, our results therefore suggest that planet-induced vortices are more likely to be observed at larger radii.

It should be noted that planet growth timescales of 100 and 1000 planetary orbits are at the very low end of the spectrum of physically expected planet growth times. Hammer et al. (2017) provided estimates for more realistic planet growth times of several thousand to tens of thousands of orbits. It remains to be seen whether the effects observed in this study still appear for longer, more realistic planet-growth timescales. However, simulating the disks at the required resolution of at least 16 cps for longer planet-growth times along with the additional vortex evolution time is still computationally expensive.

6.5. Using the lifetime of vortices in simulations to explain observations

In the suite of simulations we carried out, the lifetime of vortices in models with identical physical parameters varies significantly with resolution. This was the case for low values of the viscous α parameter ($\alpha = 10^{-5}, 10^{-6}$). We argue that the numerical viscosity of our simulation codes is comparable to $\alpha_{\rm num} \lesssim 10^{-5}$. This suggests that simulations with a prescribed viscosity of the order of the numerical viscosity cannot be used as a controlled numerical experiment, at least as far as the occurrence and persistence of vortices is concerned. For prescribed viscosities well above the estimated numerical viscosity ($\alpha = 10^{-4}, 10^{-3}$ in our case), the consistency of vortex lifetimes between the two codes and numerical choices supports the idea that the numerical experiment is indeed a controlled one.

Recent observations of molecular line broadening (e.g., Flaherty et al. 2018) and numerical studies of VSI turbulence (e.g., Flock et al. 2017) and planet–disk interaction (e.g., Zhang et al. 2018) point to low α values. The requirement of a numerical viscosity lower than the physical viscosity necessitates high resolution, which poses a challenge for simulations of vortices in protoplanetary disks.

6.6. Resolution and numerical viscosity

Vortex evolution in "inviscid" disks is often studied using very high-resolution grids to minimize the effects of numerical viscosity (Li et al. 2005; Paardekooper et al. 2010; Lin & Papaloizou 2011; Zhu & Baruteau 2016; Hammer et al. 2017, 2021; McNally et al. 2019; Fung & Ono 2021). While the resolution of 8 and 16 cells per scale height is likely enough to resolve planet-generated features such as the gap shape and spiral arms (see Appendix A), the numerical viscosity also needs to be low enough not to interfere with vortex decay.

An estimation of the numerical viscosity, valid for first-order schemes, is $\nu_{\rm num} \sim \frac{\Delta x^2}{\Delta t}$, with a representative cell size Δx and the time-step Δt. For our choices of parameters and assuming $\Delta t \approx \frac{\Delta x}{c_s}$ this corresponds to $\alpha_{\rm num} \sim 10^{-2}$–$10^{-1}$. Clearly, we see substantial changes in dynamics down to much lower values of the prescribed α. Because we employ a higher-order scheme, this simple estimate is not applicable. To our knowledge, there exists no formula to estimate the numerical viscosity for the higher-order schemes employed in this study, and so we attempt to estimate it by comparing the results of our simulations at different values of α.

In general, we observe similar behavior between models with $\alpha = 10^{-5}$ and 10^{-6}, in terms of both the behavior of vortices during their lifetime (size, mass, migration patterns) and the overall lifetime itself (see Fig. 4). This is also true across both codes that we used in this study, with the exception of the 8 cps models for $\beta = 100$. We attribute the similarity to the numerical diffusion inherent in the different advection schemes of the two codes and expect that this translates to an effective $\alpha_{\rm num}$ between 10^{-6} and 10^{-5} for our given choices of grid resolution. This implies that our experiments with $\alpha = 10^{-6}$ are most likely not controlled ones, and for this reason, we typically group models with $\alpha \leq 10^{-5}$ together.

Nevertheless, we still observe a different behavior for some models with $\alpha = 10^{-6}$ when comparing them to those with $\alpha = 10^{-5}$, such as the migration of the long-lived models presented in Sect. 5 (see the different tracks of $r_{\rm vort}(t)$ in Fig. 8), most of which have a 16 cps resolution. This hints at a lower numerical diffusion for 16 cps of $\alpha_{\rm num} \sim 10^{-6}$. Because the numerical viscosity in the 8 cps models might interfere with the prescribed $\alpha \leq 10^{-5}$, our 8 cps simulations might not be as trustworthy as our higher resolution 16 cps, $\alpha \leq 10^{-5}$ runs.

6.7. Effects of the different numerics of the two codes

We used two codes (PLUTO and FargoCPT) with fundamentally different numerical properties. The fact that the two codes agree in terms of results (see the orange lines in Fig. 8 for one striking example) is reassuring, but it is worth discussing their differences nonetheless.

FargoCPT requires an artificial viscosity prescription to stabilize the upwind method near regions of strong compression

such as shocks. This provides additional dissipation which could affect the evolution of vortices whenever they interact with the spiral shocks induced by the planet. With the exception of the 8 cps models for $\beta = 100$, we found no significant differences in vortex lifetimes between the two codes. The one case for which the codes disagreed might be a result of insufficient resolution because the differences disappear for 16 cps.

On the other hand, PLUTO's strictly energy-conserving nature means that the evolved quantity in the energy equation is the sum of kinetic and thermal energy. As kinetic energy dominates over thermal in typical Keplerian flows (for our setup, $E_{\rm kin}/E_{\rm th} \approx \frac{\gamma-1}{2h^2} = 80$), numerical errors in the calculation of total energy could affect the thermal energy budget of the disk due to subtractive cancellation error. In order to check this effect, we reran our fiducial model using the ENTROPY_SWITCH option of PLUTO, which ensures entropy conservation outside of the vicinity of shocks (which by definition do not conserve entropy, but are captured accurately by the Riemann solver). We find that this does not affect the life track of the generated vortex.

Finally, we also reran the fiducial model with PLUTO using a third-order solver and parabolic reconstruction instead of the standard second-order solver and linear reconstruction setup. We find no differences in vortex evolution or lifetime. On the basis of our tests and the agreement of the codes for high resolution, we conclude that the vortex dynamics and effects we observed in our simulations are not numerical artifacts but are indeed physical.

7. Summary

We studied vortices created by planets in protoplanetary disks using 2D viscous hydrodynamics simulations. The equation of state was assumed to follow an ideal gas, turbulence was included following the α parametrization, and thermal processes were considered by prescribing a thermal relaxation timescale using the β formalism. Our focus was on vortices exterior to the gap opened by the planet. In order to verify our results, we carried out the simulations with both the FARGO and PLUTO codes which use different numerical schemes. The planet was treated as a nonaccreting point mass with a smoothed gravitational potential and kept on a fixed circular orbit. Properties of vortices were automatically extracted using our newly developed Vortector Python tool, which identifies and characterizes vortices. Vortex identification was performed by looking for elliptical shapes in iso-vortensity lines in the r-ϕ plane, and characterization was performed by fitting a 2D Gaussian to the vortensity and surface density.

Vortices form during the gap-opening process as the embedded Jupiter-mass planet is introduced into the simulation. At the outer gap edge, multiple small vortices form that usually merge into a single large vortex that lives, depending on parameters, between 200 and several thousand orbits. These vortices have a FWHM (as determined by the fitted 2D Gaussian) of up to $0.4\,r_{\rm p}$ (several au for a planet at $r_{\rm p} = 5.2$ au). The mass enclosed in this vortex area is up to one planetary mass (one Jupiter-mass in our models) for our choice of disk mass.

Vortex lifetime depends on the thermal relaxation timescale such that vortices live shortest for intermediate cooling times ($\beta = 1$), a result also found by Fung & Ono (2021). We find two regimes for the lifetimes of vortices. A short-lived regime with vortex lifetimes of up to 3000 orbits is observed for slowly cooling disks ($\beta \geq 1$), in which the vortices decay faster than expected from viscous dissipation alone. In the long-lived regime, which is observed for fast cooling ($\beta \ll 1$) with the isothermal assumption as an extreme, vortices live for a much longer time and do not decay rapidly. Vortex lifetimes are considerably longer in this regime, with a lower bound on the maximum lifetime being 15 000 orbits (the model was terminated while the vortex was still alive due to runtime constraints). From our analysis, we suspect that the long lifetime for small β is connected to the interaction of the vortex with the spiral arms, which are a source of vorticity. Details are left to future studies.

Additionally, including the disk's self-gravity in our models with a Toomre parameter $Q \approx 25$ usually shortens the lifetime of vortices and stops the small initial vortices from merging into one large vortex. Typically, in our models, two smaller vortices remain after the initial gap opening process, which then decay faster compared to those in models where disk self-gravity is not accounted for. This finding that self-gravity is detrimental to vortex survival is in line with previous studies (Lovelace & Hohlfeld 2013; Zhu & Baruteau 2016; Regály & Vorobyov 2017; Pierens & Lin 2018).

Outward migration of the vortex is observed in some of the models with $\beta \ll 1$ and $\beta \gg 1$. In those cases, a second density (and thus pressure) bump forms outside of the vortex location, towards which the vortex then migrates (Paardekooper et al. 2010). In some $\beta = 0.01$ models, a small, short-lived, secondary vortex forms between the planet gap and the primary vortex.

Concerning the dependence of vortex lifetime on viscosity, we find the expected behavior that this lifetime is shorter for higher viscosity (Godon & Livio 1999; De Val-Borro et al. 2007; Ataiee et al. 2013; Fu et al. 2014; Regály et al. 2017). For the highest viscosity of $\alpha = 10^{-3}$, practically no vortices are observed. For $\alpha = 10^{-5}$ and 10^{-6} we find nearly identical results, suggesting that the numerical viscosity in our models with a resolution of 8 and 16 cells per scale height is of the order of $\alpha_{\rm 8cps} \lesssim 10^{-5}$ and $\alpha_{\rm 16cps} \approx 10^{-6}$.

Allowing the planet to grow over a longer time, 1000 instead of 100 orbits, leads to longer vortex lifetimes in all the cases we tested. This disagrees with the findings of Hammer et al. (2017), who found reduced vortex lifetimes for longer planet-growth times. In our models, vortices take longer to form in the case of the more slowly growing planet. During their decay, however, their evolution is very similar, independent of planet introduction time (see Fig. 6), which in total increases their lifetime. The fact that vortex lifetime increases for longer planet-growth timescales could be an indication that the effects presented in this study, including the long-lived vortex regime, are also applicable to longer, and arguably more realistic planet-growth timescales of around 10 000 orbits.

Estimating vortex lifetime from our results, vortices are expected to live much longer at larger distances away from their host star. The increase in expected lifetime is firstly due to the longer orbital period at large radii, but also because the expected β values – the thermal relaxation timescale compared to the orbital timescale – are much lower and vortices then likely belong to the long-lived regime (see Sect. 5). From order-of-magnitude calculations, we find that large planet-induced vortices exterior to the planet at 50–100 au might live for up to several million years for low-viscosity disks ($\alpha \lesssim 10^{-4}$). Considering the sensitivity of instruments like ALMA at these distances from the star, this suggests that these vortices should be observable more easily than planet-induced vortices at smaller radii.

Acknowledgements. T.R. and W.K. acknowledge funding from the Deutsche Forschungsgemeinschaft (DFG) research group FOR 2634 "Planet Formation Witnesses and Probes: Transition Disks" under grant DU 414/22-1 and KL

650/29-1, 650/30-1. W.B., W.K., and A.Z. acknowledge support by the DFG-ANR supported GEPARD project (ANR-18-CE92-0044 DFG: KL 650/31-1). The authors acknowledge support by the High Performance and Cloud Computing Group at the Zentrum für Datenverarbeitung of the University of Tübingen, the state of Baden-Württemberg through bwHPC and the German Research Foundation (DFG) through grant INST 37/935-1 FUGG. Plots in this paper were made with the Python library `matplotlib` (Hunter 2007).

References

Ataiee, S., Pinilla, P., Zsom, A., et al. 2013, A&A, 553, L3
Ataiee, S., Dullemond, C. P., Kley, W., Regály, Z., & Meheut, H. 2014, A&A, 572, A61
Bae, J., Zhu, Z., & Hartmann, L. 2016, ApJ, 819, 134
Balbus, S. A., & Hawley, J. F. 1991, ApJ, 376, 214
Barge, P., & Sommeria, J. 1996, NASA Conf. Pub., 3343, 179
Benítez-Llambay, P., & Masset, F. S. 2016, ApJS, 223, 11
Bradski, G. 2000, Dr. Dobb's Journal of Software Tools
Cimerman, N. P., & Rafikov, R. R. 2021, MNRAS, 508, 2329
Crida, A., Morbidelli, A., & Masset, F. 2006, Icarus, 181, 587
De Val-Borro, M., Edgar, R. G., Artymowicz, P., et al. 2006, MNRAS, 370, 529
De Val-Borro, M., Artymowicz, P., D'Angelo, G., & Peplinski, A. 2007, A&A, 471, 1043
Dullemond, C. P. 2000, A&A, 361, L17
Dullemond, C. P., Birnstiel, T., Huang, J., et al. 2018, ApJ, 869, L46
Flaherty, K. M., Hughes, A. M., Teague, R., et al. 2018, ApJ, 856, 117
Flock, M., Nelson, R. P., Turner, N. J., et al. 2017, ApJ, 850, 131
Flock, M., Turner, N. J., Nelson, R. P., et al. 2020, ApJ, 897, 155
Fu, W., Li, H., Lubow, S., & Li, S. 2014, ApJ, 788, L41
Fung, J., & Ono, T. 2021, ApJ, 922, 13
Gammie, C. F. 2001, ApJ, 553, 174
Godon, P., & Livio, M. 1999, ApJ, 523, 350
Hammer, M., Kratter, K. M., & Lin, M.-K. 2017, MNRAS, 466, 3533
Hammer, M., Pinilla, P., Kratter, K. M., & Lin, M.-K. 2019, MNRAS, 482, 3609
Hammer, M., Lin, M.-K., Kratter, K. M., & Pinilla, P. 2021, MNRAS, 504, 3963
Hunter, J. D. 2007, Comput. Sci. Eng., 9, 90
Kanagawa, K. D., Tanaka, H., Muto, T., & Tanigawa, T. 2017, PASJ, 69, 97
Keppler, M., Benisty, M., Müller, A., et al. 2018, A&A, 617, A44
Klahr, H. H., & Bodenheimer, P. 2003, ApJ, 582, 869
Kley, W., & Nelson, R. P. 2012, ARA&A, 50, 211
Lega, E., Nelson, R. P., Morbidelli, A., et al. 2021, A&A, 646, A166
Les, R., & Lin, M.-K. 2015, MNRAS, 450, 1503
Lesur, G., & Papaloizou, J. C. B. 2009, A&A, 498, 1
Lesur, G., & Papaloizou, J. C. B. 2010, A&A, 513, A60
Levermore, C. D., & Pomraning, G. C. 1981, ApJ, 248, 321
Li, H., Li, S., Koller, J., et al. 2005, ApJ, 624, 1003
Lin, M.-K., & Papaloizou, J. C. B. 2011, MNRAS, 415, 1426
Lovelace, R. V. E., & Hohlfeld, R. G. 2013, MNRAS, 429, 529
Lovelace, R. V. E., Li, H., Colgate, S. A., & Nelson, A. F. 1999, ApJ, 513, 805
Marcus, P. S., Pei, S., Jiang, C.-H., et al. 2015, ApJ, 808, 87
Marcus, P. S., Pei, S., Jiang, C.-H., & Barranco, J. A. 2016, ApJ, 833, 148
Marel, N. v. d., Dishoeck, E. F. v., Bruderer, S., et al. 2013, Science, 340, 1199
Masset, F. 2000, A&AS, 141, 165
McNally, C. P., Nelson, R. P., Paardekooper, S.-J., & Benítez-Llambay, P. 2019, MNRAS, 484, 728
Mignone, A., Bodo, G., Massaglia, S., et al. 2007, ApJS, 170, 228
Mignone, A., Flock, M., Stute, M., Kolb, S. M., & Muscianisi, G. 2012, A&A, 545, A152
Miranda, R., & Rafikov, R. R. 2020a, ApJ, 892, 65
Miranda, R., & Rafikov, R. R. 2020b, ApJ, 904, 121
Müller, T. W. A., Kley, W., & Meru, F. 2012, A&A, 541, A123
Nelson, R. P., Gressel, O., & Umurhan, O. M. 2013, MNRAS, 435, 2610
Ogilvie, G. I., & Lubow, S. H. 2002, MNRAS, 330, 950
Paardekooper, S.-J., Lesur, G., & Papaloizou, J. C. B. 2010, ApJ, 725, 146
Pierens, A., & Lin, M.-K. 2018, MNRAS, 479, 4878
Pérez, L. M., Benisty, M., Andrews, S. M., et al. 2018, ApJ, 869, L50
Rafikov, R. R. 2002, ApJ, 569, 997
Rafikov, R. R. 2016, ApJ, 831, 122
Regály, Z., & Vorobyov, E. 2017, MNRAS, 471, 2204
Regály, Z., Sándor, Z., Csomós, P., & Ataiee, S. 2013, MNRAS, 433, 2626
Regály, Z., Juhász, A., & Nehéz, D. 2017, ApJ, 851, 89
Rometsch, T., Rodenkirch, P. J., Kley, W., & Dullemond, C. P. 2020, A&A, 643, A87
Shakura, N. I., & Sunyaev, R. A. 1973, A&A, 500, 33
Tarczay-Nehéz, D., Regály, Z., & Vorobyov, E. 2020, MNRAS, 493, 3014
Tassoul, J.-L. 1978, Theory of Rotating Stars (Princeton: Princeton Legacy Library)
Zhang, S., & Zhu, Z. 2020, MNRAS, 493, 2287
Zhang, S., Zhu, Z., Huang, J., et al. 2018, ApJ, 869, L47
Zhu, Z., & Baruteau, C. 2016, MNRAS, 458, 3918
Ziampras, A., Ataiee, S., Kley, W., Dullemond, C. P., & Baruteau, C. 2020a, A&A, 633, A29
Ziampras, A., Kley, W., & Dullemond, C. P. 2020b, A&A, 637, A50

Appendix A: Grid resolution and numerical convergence

A grid resolution of 8 cells per scale height (cps) is often adopted in models of planet–disk interaction in the literature. While it is widely agreed upon as sufficient, we test this statement by performing a series of test simulations with both `PLUTO` and `FargoCPT` using the same physical parameters as our locally isothermal models ($\alpha = 10^{-5}$), but using varying grid resolutions with 1, 2, 4, 8, and 16 cps in both directions (always maintaining square cells).

We find that we achieve numerical convergence on large-scale features such as the gap width and pressure bumps for a resolution of 4 cps. Convergence on more numerically sensitive features such as gap depth and vortex formation is reached for a resolution of 8 cps, with 16 cps affecting the picture relatively weakly. This was observed across both codes, with the two showing very good agreement with each other both in terms of the resolution at which different features converge and the physical properties of said features across codes.

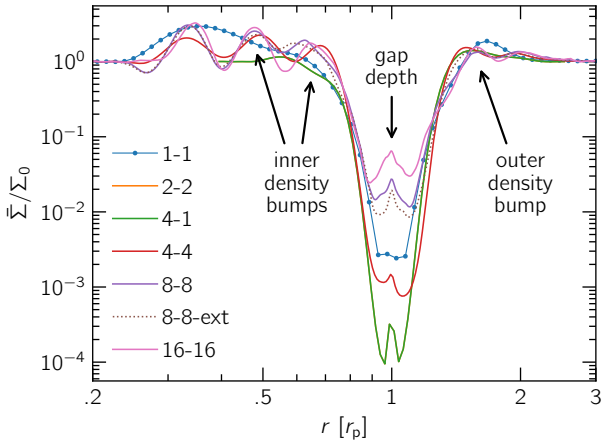

Fig. A.1. Results for our resolution study using `FargoCPT`. The overall shape of the gap is resolved with around 4 cps, while it takes 8 cps to properly resolve the gap depth and the contrast of most pressure bumps far from the gap. We are interested in the region between 0.5–2.0 r_p. Extending the outer boundary to $r = 10\,r_p$ in the "8-8-ext" model practically made no difference. It should be noted that the 16×16 cps model develops some small-scale vortices in the inner disk, which causes these differences around $0.7\,r_p$. Interestingly, a model that resolves the radial and azimuthal directions with 4 and 1 cps, respectively, captures these radial features almost as well as one with 4 cps in both directions.

Appendix B: The Vortector

A major task in this study was the identification and characterization of vortices in simulation data. For this purpose, we developed a Python package, the `Vortector`, which automates the process for relatively generic 2D hydrodynamics planet–disk simulations.

The `Vortector` package allows one to visualize the vortex detection results (an example is shown in Fig. B.2), and includes information about the location, extent, and mass of a vortex along with various statistics related to the contour.

The package is publicly available on GitHub[1]. We hope to make the detection and characterization of vortices in simulation data easier for other members of the community and facilitate quantitative comparison of vortices between studies by providing a common detection pipeline.

To search for possible vortex candidates, a simple search for the location of minimum vortensity is sometimes enough to find the location of a vortex. Then, the value of the vorticity $\omega = (\nabla \times \boldsymbol{u}) \cdot \hat{z}$ can be used to learn how strongly the vortex rotates and the local surface density can be used as an indication for the mass enclosed in the vortex. However, this method fails for many simulations, e.g., when the vortensity in a very small region close to a spiral arm of the planet is lower than inside a vortex candidate, or when the gap region intrudes into the outer disk, which can induce strong anticyclonic motion at the outer gap edge.

To get around these issues, the `Vortector` uses the geometrical shape of vortices as they appear in a face-on image of the disk. Looking down on the surface of a disk, vortices appear as crescent-shaped objects. In the r-ϕ plane, which is more suitable for this task, large vortices appear as elliptical objects (see also Fig. 1 of Lesur & Papaloizou 2009). In fact, contour lines of the vortensity closely resemble ellipses in the r-ϕ plane. We can therefore identify vortices in a disk by finding closed contour lines that closely resemble ellipses. To solve this task programmatically, we can make use of the computer vision library `OpenCV` (Bradski 2000).

Our strategy to extract vortex candidates from a simulation snapshot can be then subdivided into three tasks:

1. Extract contour lines in the r-ϕ map of the vortensity,
2. identify nearly elliptical contours as vortex candidates, and
3. fit 2D Gaussians to ϖ and Σ for characterization.

The algorithm step by step

This section describes the vortex detection process using the model presented in Sect. 5 (`FargoCPT`, $\alpha = 10^{-5}$, $\beta = 0.01$, 16 cps) which shows the emergence of a secondary vortex. The data used for this analysis corresponds to a time $t = 7150$ orbits.

Before the analysis is performed on ϖ, the map is periodically extended in the ϕ direction in order to be able to identify vortices that intersect the periodic azimuthal boundary. The resulting image is shown in the left panel of Fig. B.1. There, the original domain is indicated by the thick solid rectangle, which spans the azimuthal range from 0 to N, where N is the image size in pixels in the azimuthal direction. The top and bottom areas of the domain (orange and green) are repeated at the lower and upper boundaries, respectively.

Task 1: Contour lines

Contour lines are extracted for a range of ϖ values ranging from 0 to 1 in increments of 0.05. For each value $\varpi_{\rm crit}$, a binary image is produced by setting each cell with $\varpi \geq \varpi_{\rm crit}$ to 1 and 0 otherwise. The binary image is then analyzed using `findContours` from `OpenCV`. Only closed contours are retained. This step usually results in up to a few thousand contours, depending on the dynamical state of the disk and the choice of increments in ϖ.

[1] https://github.com/rometsch/vortector

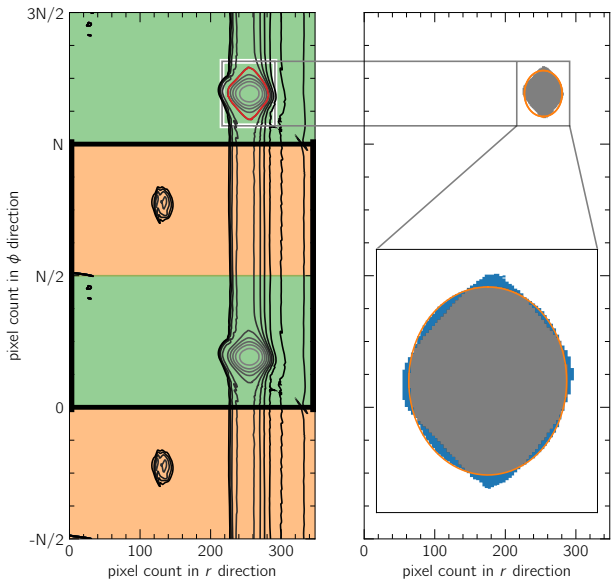

Fig. B.1. Periodically continued iso-vortensity line image (left) used for extracting contours for vortex candidates and an example contour illustrating the ellipse fit (right). The snapshot shown is at time $t = 7150$ orbits of the model with the secondary vortex that was discussed in Sect. 5. The left panel shows how the data array is mirrored in order to allow the detection of vortices that overlap with the periodic boundary. Areas with the same color are copies of one another. The red line indicates the outline of the grey area in the right panel. The original size is marked by the black rectangle ranging from 0 to N on the vertical axis. The area shaded in blue in the right panel illustrates the definition of the deviation from the ellipse that is used to select the vortex candidates from the closed contours. For the example shown, the ratio of difference area (blue) to the total contour area is 0.122, which is below the 0.15 threshold.

Task 2: Find closed contours resembling ellipses

Next, the `fitEllipse` function from `OpenCV` is used to fit an ellipse to each closed contour. One example of this is shown in the right panel of Fig. B.1, where the ellipse is visible as an orange line in the zoom-in.

The difference in area between the contour and fit is used as a measure of deviation. The deviation from an ellipse is then defined as the ratio of this difference and the area enclosed by the contour. We only keep contours for which the deviation is smaller than 0.15. The example contour in Fig. B.1 has a deviation of 0.122.

Finally, all the contours that are contained within the largest contour that satisfies this criterion are discarded, which leaves the example red contour in Fig. B.1 as the selected vortex candidate (see also the white contour line in Fig. B.2).

We only retain contours that enclose at least two other contours. With this restriction, we make sure that ϖ/ϖ_0 changes by a value of 0.1 from the outside to the inside of the vortex candidate. This has proven to be useful to filter out small fluctuations in the disk that otherwise appear as small transient vortices.

At this point, it becomes clear that the extent of the vortex and derived quantities such as the mass contained within are influenced by the choice of the levels used to produce the contour lines and the choice of the maximum relative ellipse deviation. The properties of the contour give an order-of-magnitude estimate nonetheless.

Task 3: Fit a 2D Gaussian

To remove the influence of the threshold parameters in the detection of the contour, a process that does not depend on our parameter choices but on the underlying data is needed.

Upon inspection of the curves of vortensity and surface density along a cut through the vortex, either radial or azimuthal, it becomes clear that these lines resemble Gaussian functions (see curves in Fig. B.2 around the 2D maps)

$$f(r,\phi) = c + a \exp\left(-\frac{(r-r_0)^2}{2\sigma_r^2}\right) \exp\left(-\frac{(\phi-\phi_0)^2}{2\sigma_\phi^2}\right). \tag{B.1}$$

Here, σ_r and σ_ϕ provide a measure for the vortex size and can even be used to give a definition of the vortex region that does not depend on additional parameters. In combination with the center coordinates r_0 and ϕ_0, σ_r and σ_ϕ can be used to define the vortex as the disk material contained within the ellipse given by

$$\left(\frac{r-r_0}{h_r}\right)^2 + \left(\frac{\phi-\phi_0}{h_\phi}\right)^2 = 1\,, \tag{B.2}$$

where $h_r = \sqrt{2\ln(2)}\,\sigma_r$ and $h_\phi = \sqrt{2\ln(2)}\,\sigma_\phi$ denote the half width at half maximum of the 2D Gaussian function defined in Eq. (B.1). We usually use the values obtained from the surface density fit because these are less time-sensitive compared to the vortensity fit and because the shape of Σ curves more closely resemble Gaussians (see Fig. B.2).

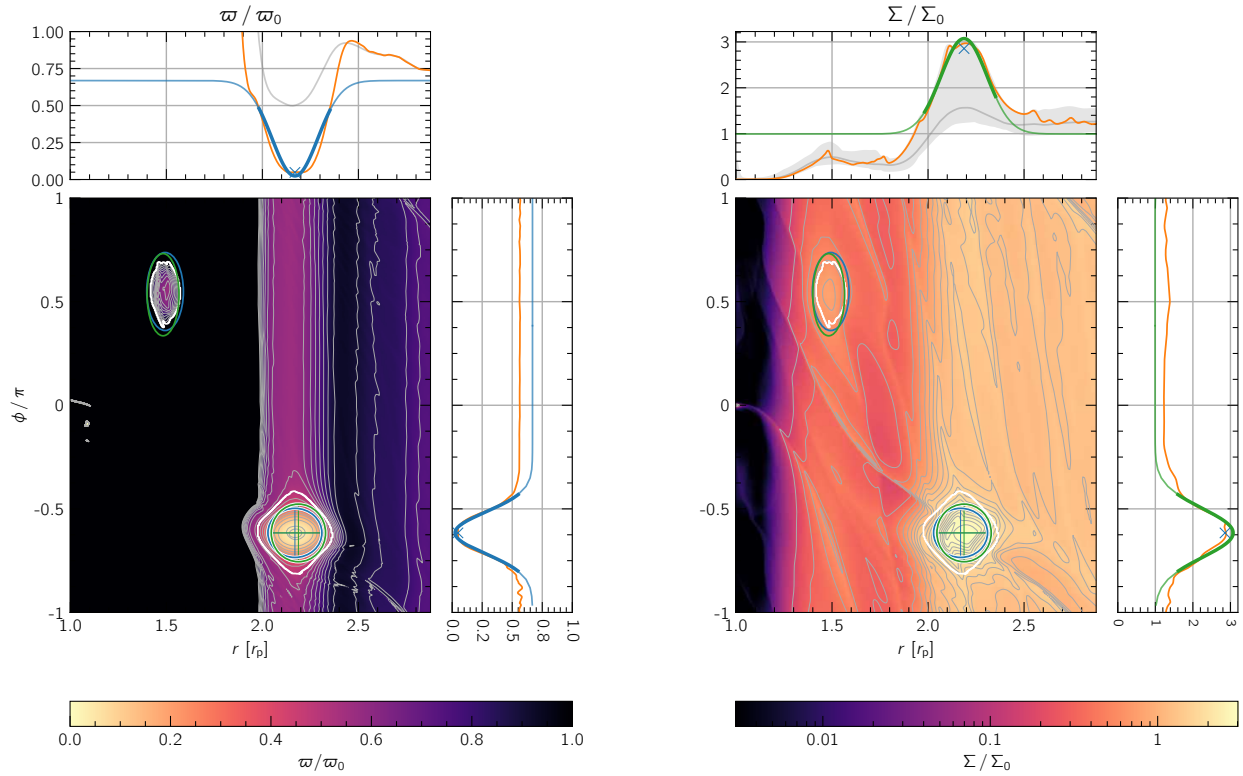

Fig. B.2. Overview of the results produced by the `Vortector` package for a model showing a secondary vortex discussed in Sect. 5 at t = 7150 orbits, with a 2D map of the vortensity on the left and surface density on the right. All detected vortex candidates are indicated in the 2D plots. The extracted contour (shown in Fig. B.1) is marked with a white line, the ellipse of the vortensity fit is shown in blue and the ellipse of the surface density fit is shown in green. Note that these ellipses are defined by σ_r and σ_ϕ from the fit of Eq. (B.2) and are different from the ellipse used to fit the contour. The ellipses of the most massive vortex include a crosshair indicating the center of the fit. Each 2D plot is accompanied by 1D plots of slices through the main vortex. The plots also show the values of the respective Gaussian fit in blue for vortensity and green for surface density. In this figure, the planet is located at $r = 1$ and $\phi = 0$.

Appendix C: Data table

The lifetimes and parameters of all models mentioned in Sects. 4 and 5 are listed in Table C.1.

Table C.1. Lifetimes of vortices in the simulations.

code	β	α	cps	$\tau_{\rm intro}$ [a]	special [b]	in Fig. 4	$T_{\rm vort}$ [c]	code	β	α	cps	$\tau_{\rm intro}$ [a]	special [b]	in Fig. 4	$T_{\rm vort}$ [c]
fargo	0.01	10^{-6}	16	100		x	>8784	fargo	1	10^{-5}	8	1000			1279
pluto	0.01	10^{-6}	16	...		x	9548	fargo	1	10^{-5}	8			x	1179
fargo	0.01	10^{-6}	8			x	1679	fargo	1	10^{-5}	8		sg	x	289
pluto	0.01	10^{-6}	8			x	2013	fargo	1	10^{-5}	8	1000	sg		509
fargo	0.01	10^{-5}	32				>739	pluto	1	10^{-5}	8			x	1136
fargo	0.01	10^{-5}	16			x	8774	pluto	1	10^{-5}	8	1000			956
fargo	0.01	10^{-5}	16		sg		>4567	fargo	1	10^{-4}	16			x	709
pluto	0.01	10^{-5}	16			x	>15100	pluto	1	10^{-4}	16			x	757
pluto	0.01	10^{-5}	16				5762	fargo	1	10^{-4}	8			x	659
pluto	0.01	10^{-5}	16		vort rem		1843	pluto	1	10^{-4}	8			x	607
fargo	0.01	10^{-5}	8	1000			3897	fargo	1	10^{-3}	16			x	0
fargo	0.01	10^{-5}	8			x	2288	pluto	1	10^{-3}	16			x	49
fargo	0.01	10^{-5}	8				7845	fargo	1	10^{-3}	8			x	59
fargo	0.01	10^{-5}	8		sg	x	1299	pluto	1	10^{-3}	8			x	0
fargo	0.01	10^{-5}	8	1000	sg		1269	fargo	100	10^{-6}	16			x	1729
pluto	0.01	10^{-5}	8			x	2611	pluto	100	10^{-6}	16			x	2441
pluto	0.01	10^{-5}	8	1000			2691	fargo	100	10^{-6}	8			x	3108
pluto	0.01	10^{-5}	8				10638	pluto	100	10^{-6}	8			x	946
fargo	0.01	10^{-4}	16			x	1129	fargo	100	10^{-5}	16			x	1888
pluto	0.01	10^{-4}	16			x	1335	pluto	100	10^{-5}	16			x	1943
fargo	0.01	10^{-4}	8			x	979	fargo	100	10^{-5}	8	1000			3048
pluto	0.01	10^{-4}	8			x	887	fargo	100	10^{-5}	8			x	2708
fargo	0.01	10^{-3}	16			x	79	fargo	100	10^{-5}	8		sg	x	589
pluto	0.01	10^{-3}	16			x	0	fargo	100	10^{-5}	8	1000	sg		499
fargo	0.01	10^{-3}	8			x	69	pluto	100	10^{-5}	8			x	857
pluto	0.01	10^{-3}	8			x	29	pluto	100	10^{-5}	8	1000			0
fargo	1	10^{-6}	16			x	1309	fargo	100	10^{-4}	16			x	699
pluto	1	10^{-6}	16			x	1694	pluto	100	10^{-4}	16			x	797
fargo	1	10^{-6}	8			x	1189	fargo	100	10^{-4}	8			x	569
pluto	1	10^{-6}	8			x	1106	pluto	100	10^{-4}	8			x	478
fargo	1	10^{-5}	16			x	1359	fargo	100	10^{-3}	16			x	0
fargo	1	10^{-5}	16		sg		649	pluto	100	10^{-3}	16			x	0
pluto	1	10^{-5}	16			x	1445	fargo	100	10^{-3}	8			x	0
pluto	1	10^{-5}	16		art vort		916	pluto	100	10^{-3}	8			x	0

Notes. Models with a resolution of 8, 16, and 32 cps have 528×1024, 1056×2048, and 2112×4096 cells, respectively. [(a)]Planet introduction time. 100 orbits if empty. [(b)]Special propertiy of the model. "sg" if self-gravity is included. "vort rem" and "art vort" refer to the models discussed in Sect. 6.1 with the removed vortex and the artificial vortex, respectively. [(c)]Lifetime of the vortex in planetary orbits. ">" indicates that the vortex still exists at the end of the simulation.